UNIVERSIDAD DE CANTABRIA

Facultad de Ciencias

Dpto. de Ciencias de la Tierra y Física de la Materia Condensada

TESIS DOCTORAL

PROPIEDADES MAGNÉTICAS Y ESTRUCTURALES DE NUEVOS LÍQUIDOS IÓNICOS MAGNÉTICOS (MILs) BASADOS EN IMIDAZOLIO Y HALUROS DE HIERRO

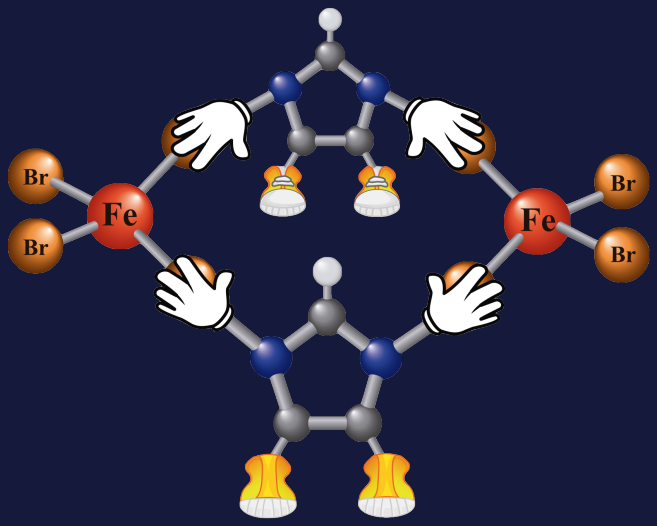

Abel García Saiz

Santander, Marzo de 2016

FACULTAD DE CIENCIAS

DPTO. DE CIENCIAS DE LA TIERRA Y FISICA DE LA MATERIA CONDENSADA

TESIS DOCTORAL:

PROPIEDADES MAGNÉTICAS Y ESTRUCTURALES DE NUEVOS LÍQUIDOS IÓNICOS MAGNÉTICOS (MILs) BASADOS EN IMIDAZOLIO Y HALUROS DE HIERRO

Tesis presentada por Abel García Saiz para la obtención del grado de Doctor por la Universidad de Cantabria

---

Supervisado por:

Prof. Jesús Rodríguez Fernández

Dr. Imanol de Pedro del Valle

Santander, Febrero 2016

“La verdadera ciencia enseña, sobre todo, a dudar y a ser ignorante”

Miguel de Unamuno

Dedicado a
mi familia y amigos

UNIVERSIDAD DE CANTABRIA

Resumen

Facultad de Ciencias
Dpto. de Ciencias de la Tierra y Física de la Materia Condensada

PROPIEDADES MAGNÉTICAS Y ESTRUCTURALES DE NUEVOS LÍQUIDOS IÓNICOS MAGNÉTICOS (MILs) BASADOS EN IMIDAZOLIO Y HALUROS DE HIERRO

por Abel García Saiz

Los Líquidos Iónicos Magnéticos (MILs) son una nueva clase de materiales inteligentes que permiten combinar las propiedades típicas de los líquidos iónicos tales como baja presión de vapor o la excelente estabilidad térmica, con nuevos atributos debidos al ion metálico incorporado, los cuales podrían ser controlados por campos magnéticos externos. Es por ello que desde su reciente descubrimiento, su desarrollo combinando diferentes cationes y aniones ha permitido mejorar sus cualidades para futuras aplicaciones en numerosos campos entre los que destacan la catálisis y los procesos de separación selectiva de gases o materiales.

En esta tesis se ha abordado el desarrollo de nuevos líquidos iónicos magnéticos (MILs) basados en cationes de imidazolio y haluros de hierro, que presentan ordenamiento magnético en estado sólido a bajas temperaturas. Inicialmente se ha estudiado los efectos de la presión y de la deuteración en un MIL ya conocido, el Emim[$FeCl_4$] y posteriormente se ha sintetizado y estudiado 4 nuevos MILs. Para ello se han utilizado diversas técnicas de caracterización físico química, estructural y de análisis de las propiedades térmicas y magnéticas. Finalmente, se ha afrontado el estudio de sus correlaciones magneto-estructurales combinando los resultados experimentales de difracción de rayos X, de radiación sincrotrón y de neutrones con los resultados de cálculos teóricos basados en el funcional de la densidad (DFT).

Como resultados principales se destacan: (i) que se ha logrado mejorar las interacciones magnéticas de los MILs predecesores, (ii) se ha podido inducir transiciones magnéticas a través de la aplicación de presiones hidrostáticas, (iii) que se ha determinado por primera vez la estructura magnética de un MIL, donde las interacciones magnéticas

principales vienen dadas por interacciones de supercanje Fe-X–X-Fe (X = halógeno) no covalentes entre los complejos metálicos vecinos y (iv) se ha comprobado que la influencia del tamaño del catión y la electronegatividad del halógeno en los complejos metálicos no son los responsables principales del aumento de las interacciones magnéticas, sino que viene dado principalmente por una transferencia de momento magnético de los hierros a los halógenos vecinos.

Agradecimientos

Cuatro años han pasado ya desde que empecé en el CITIMAC, en mitad del máster de materiales buscando un tema para realizar la tesis. No me imaginaba como iban a ser los años siguientes y aunque no me dedique actualmente al mundo de la investigación, no me arrepiento de esta experiencia y es por ello que quiero expresar mi agradecimiento a todas las personas que directa o indirectamente han contribuido en la realización de este trabajo.

En primer lugar a mis directores de tesis, el Prof. Jesús Rodríguez Fernández y al Dr. Imanol de Pedro del Valle. Gracias por todo el apoyo que han hecho de estos años una buena experiencia. Con todos los viajes a realizar experimentos, congresos, cursos... Por no daros por vencido y apoyarme cuando decidí cambiar de aires y dejé la beca para dedicarme a la programación. No estaría aquí con la tesis terminada y a punto de presentarse. Por ser como unos padres dentro del trabajo. Este trabajo es de todos nosotros. Muchas gracias.

A los demás miembros del grupo de Magnetismo de la Universidad de Cantabria, Luis Fernández y José I. Espeso, que aunque la temática no fuera la misma, siempre estaban ahí cuando les necesitaba. Gracias.

A los todos los compañeros de despacho, Marta, Pablo, Susana, Cristina, María (y Carlos, como uno más). Gracias por los ratos en el despacho que hacían más ameno el trabajo.

A Luis Echeandía, que siempre estaba disponible para echar una mano cuando lo necesitaba en el laboratorio. Gracias.

A Rosa y Nieves, que siempre me ayudaban con una sonrisa con los temas administrativos (que no eran pocos). Gracias.

Y al resto de miembros del departamento CITIMAC (y Rafa) que a pesar de ser tantos, siempre ha habido buena relación, principalmente por los momentos en la cafetería. Gracias a todos.

A Jesús Blanco, por mostrar siempre interés en el tema de esta tesis y aportar sus conocimientos para el estudio de mis muestras. Muchas gracias.

A Jordi Rius y Oriol Vallcorba, que hicieron de mi estancia de 3 meses en el ICMAB y los experimentos en ALBA una buena experiencia y que me sintiera a gusto. Gracias.

A los miembros del grupo de difracción del ILL, en especial a M. Teresa Fernández Díaz y a Óscar Fabelo, que hicieron agradables y divertidos todos los viajes a Grenoble. Muchas gracias por la acogida y toda vuestra ayuda.

A mis amigos, que en un momento u otro han estado ahí y estarán en el futuro. Muchas gracias.

Y para terminar, mi familia, con la que siempre puedo contar para todo y siempre están ahí apoyándome en todas las decisiones. Os quiero. Muchas gracias por todo.

Índice de publicaciones

La Tesis Doctoral se presenta por compendio de artículos publicados o aceptados para su publicación en revistas científicas incluidas en la relación de revistas del Journal of Citation Reports-Science Edition (JCR-SCE), cumpliendo con la normativa existente en la Universidad de Cantabria y en el Departamento de Ciencias de la Tierra y Física de la Materia Condensada (CITIMAC) en relación a la elaboración de Tesis Doctorales en este formato.

- ***Título:*** Pressure effects on emim[$FeCl_4$], a magnetic ionic liquid with three-dimensional magnetic ordering.
  - *Autores:* Abel García-Saiz, Imanol de Pedro, Jesús A Blanco, Jesús Antonio González, Jesús Rodríguez Fernández
  - *Referencia:* J. Phys. Chem. B 2013, 117, 3198 – 3206
  - *DOI:* dx.doi.org/10.1021/jp3114623
  - *Índice de impacto:* 3.377

- ***Título:*** A Magnetic Ionic Liquid Based on Tetrachloroferrate Exhibits Three-Dimensional Magnetic Ordering: A Combined Experimental and Theoretical Study of the Magnetic Interaction Mechanism.
  - *Autores:* Abel García-Saiz, Pedro Migowski, Oriol Vallcorba, Javier Junquera, Jesús Angel Blanco, Jesús Antonio González, María Teresa Fernández-Díaz, Jordi Rius, Jairton Dupont, Jesús Rodríguez Fernández, Imanol de Pedro
  - *Referencia:* Chem. Eur. J. 2014, 20, 72 – 76
  - *DOI:* dx.doi.org/10.1002/chem.201303602
  - *Índice de impacto:* 5.731

- ***Título:*** Anion-π and Halide-Halide Nonbonding Interactions in a New Ionic Liquid Based on Imidazolium Cation with Three-Dimensional Magnetic Ordering in the Solid State.
  - *Autores:* Abel García-Saiz, Imanol de Pedro, Pedro Migowski, Oriol Vallcorba, Javier Junquera, Jesús Angel Blanco, Oscar Fabelo, Denis Sheptyakov, Joao Carlos Waerenborgh, Maria Teresa Fernández-Díaz, Jordi Rius, Jairton Dupont, Jesús Antonio González, Jesús Rodríguez Fernández
  - *Referencia:* Inorg. Chem. 2014, 53, 8384 – 8396
  - *DOI:* dx.doi.org/10.1021/ic500882z
  - *Índice de impacto:* 4.762

- ***Título:*** 1-Ethyl-2,3-dimethylimidazolium paramagnetic ionic liquids with 3D magnetic ordering in its solid state: synthesis, structure and magneto-structural correlations.
  - *Autores:* Abel García-Saiz, Imanol de Pedro, Oriol Vallcorba, Pedro Migowski, Ignacio Hernández, Luis Fernández Barquin, Isaac Abrahams, Majid Motevalli, Jairton Dupont, Jesús Antonio González, Jesús Rodríguez Fernández
  - *Referencia:* RSC Adv., 2015, 5, 60835 – 60848
  - *DOI:* 10.1039/c5ra05723j
  - *Índice de impacto:* 3.840

- ***Título:*** Neutron Powder Diffraction study of the Magnetic Ionic Liquid Emim[$FeCl_4$] and its deuterated phase.
  - *Autores:* Abel García-Saiz, Imanol de Pedro, Luis Fernández Barquín, Maria Teresa Fernández-Díaz, Jesús Angel Blanco, Jesús Rodríguez Fernández
  - *Referencia:* Journal of Physics: Conference Series 663 (2015) 012008
  - *DOI:* 10.1088/1742-6596/663/1/012008
  - *Índice de impacto:* -

- ***Título:*** Slow Dynamically Solid-to-Solid Phase Transition Induced by Thermal Treatment on DimimFeCl4 Magnetic Ionic Liquid.
    - *Autores:* Abel García-Saiz, Imanol de Pedro, Oriol Vallcorba, Oscar Fabelo, Javier Junquera, Jesús Ángel Blanco, João Carlos Waerenborgh, D. Andreica, Andrew Wildes, María Teresa Fernández-Díaz, and Jesús Rodríguez Fernández
    - *Referencia:* En preparación
    - *DOI:* -
    - *Índice de impacto:* -

Índice general

Resumen VII

Agradecimientos X

Índice de publicaciones XIII

Contenidos XVII

1. Los Líquidos Iónicos Magnéticos **1**
1.1. Introducción . . . 1
1.2. Síntesis y Técnicas experimentales . . . 3
1.2.1. Síntesis de MILs . . . 3
1.2.2. Caracterización físico-química . . . 4
1.2.3. Caracterización estructural . . . 5
1.2.3.1. Difracción de Rayos X . . . 6
1.2.3.2. Difracción de Neutrones . . . 6
1.2.3.3. Análisis de los diagramas de difracción . . . 7
1.2.4. Propiedades magnéticas . . . 7
1.2.4.1. Magnetometría . . . 7
1.2.4.2. Calor específico . . . 8
1.2.4.3. Mössbauer . . . 9
1.3. Cálculos *ab initio* del funcional de la densidad . . . 9
1.4. Correlaciones magnetoestructurales . . . 10

2. Emim[$FeCl_4$] **13**
2.1. Introducción . . . 13
2.2. Artículo I . . . 15
2.3. Artículo II . . . 27

3. Dimim[$FeCl_4$] **33**
3.1. Introducción . . . 33
3.2. Artículo III . . . 35
3.3. Artículo IV . . . 60

4. Dimim[$FeBr_4$] **109**
4.1. Introducción . . . 109
4.2. Artículo V . . . 111

5. Edimim[$FeCl_4$] y Edimim[$FeBr_4$] **137**
5.1. Introducción . . . 137
5.2. Artículo VI . . . 138

6. Discusión final **157**

7. Conclusiones **159**

A. Artículos **161**

B. Comunicaciones a congresos **165**

C. Experimentos en grandes instalaciones **169**

Bibliografía **171**

Capítulo 1

Los Líquidos Iónicos Magnéticos

1.1. Introducción

Uno de los principales desafíos de la Ciencia de Materiales es el diseño de nuevos compuestos así como entender y conocer sus propiedades físico-químicas debidas a su composición y estructura. Los sistemas híbridos orgánicos-inorgánicos no sólo representan una alternativa creativa para diseñar nuevos materiales con interés básico, sino que sus propiedades físico-químicas avanzadas permiten el desarrollo de numerosas aplicaciones industriales. Esto ha llevado en la actualidad a que estos sistemas jueguen un papel importante en el desarrollo de nuevos materiales funcionales, pudiendo combinar las propiedades intrínsecas de ambos componentes (orgánicos e inorgánicos), los cuales se pueden modificar con pequeñas transformaciones en la interfase. Los líquidos iónicos (ILs) son una clase de este tipo de materiales, definidos como sales fundidas con un punto de fusión por debajo de los 100 ^{o}C. Están compuestos por cationes orgánicos, generalmente iones de imidazolio, pirrolidinio, piridinio, tetraalquilamonio o tetraalquilfosfonio y aniones, como por ejemplo, Cl^{-}, Br^{-}, I^{-}, $FeCl_4^{-}$, PF_6^{-}, $AlCl_4^{-}$, BF_4^{-}, ..., donde los constituyentes orgánicos e inorgánicos están enlazados mediante fuerzas de Van der Waals (vdW). Estos compuestos han sido el centro de estudio en las últimas décadas dado que poseen interesantes propiedades físico-químicas, tales como presión de vapor despreciable, un gran rango de temperaturas en que los compuestos son líquidos, una buena estabilidad térmica, una conductividad eléctrica considerable, estabilidad química, etc.[1]

Dentro de los ILs, un nuevo tipo de materiales son los MILs (Magnetic Ionic Liquids). La investigación en estos materiales inteligentes ha evolucionado exponencialmente

en la última década debido a que estos compuestos pueden modificar sus propiedades físico-químicas con campos magnéticos externos y/o pueden ser utilizados en estado líquido como ferrofluidos libres de nanoparticulas.[2] Además, pueden combinar las propiedades de los líquidos iónicos (tales como la estabilidad térmica, alta conductividad eléctrica, presión de vapor insignificante...) con otras intrínsecas adicionales formando materiales termo-crómicos, magneto-crómicos o luminiscentes en función del ion magnético utilizado.[3] [4] [5] [6] De esta forma, esta área activa de investigación necesita un estudio multidisciplinar, que contemple la síntesis, resolución estructural y propiedades físico-químicas y magnéticas que presentan.

En el año 2004, se observó por primera vez que un IL basado en un anión de hierro, $[FeCl_4]^-$, y catión imidazolio, 1-butil-3-metilimidazolio, $[Bmim]^+$, podía presentar una respuesta magnética frente a un imán de neodimio de 0.55 T a temperatura ambiente[7]. A partir de este descubrimiento se realizaron diversos estudios técnico-aplicados de notable relevancia científica. Los primeros MILs desarrollados estaban principalmente basados en cationes de hierro (III) d^5 de alto espín, en la forma de tetracloro o tetrabromoferrato(III), combinados con diferentes cationes orgánicos como el alquilimidazolio, tetraalquilamonio o tetraalquilfosfonio. En la actualidad, el desarrollo de estos MIL ha llevado a combinar diferentes iones de metales de transición (manganeso, cobalto...), tierras raras (neodimio, gadolinio, disprosio...) o cationes quirales como son los aminoácidos; por lo que la síntesis, estudio y aplicación de estos nuevos materiales está creciendo de manera exponencial. En lo que se refiere a las aplicaciones tecnológicas de los MILs, se ha demostrado que estos materiales, al presentar una notable respuesta a campos magnéticos externos, pueden ser utilizados para el transporte y separación de materiales, como absorbente de emisiones del benceno, para procesos de catálisis[8], como extractantes de sulfuros (SO_x) en gasolinas, para reacciones de polimerización, para absorción de gases con efecto invernadero (CO_2 y SO_2)[5], o como nuevos materiales magnéticos aplicados. Sin embargo, a pesar de los progresos realizados en los últimos años en las propiedades que presentan desde un punto de vista aplicado, el estudio básico de su comportamiento magnético (tipo de interacciones magnéticas, estructuras magnéticas, correlaciones magnético-estructurales...), es aún una incógnita por resolver. Inicialmente, se asumió que en los MILs, los complejos metálicos estaban aislados unos de otros, generando una falta de interacción o acoplamiento magnético de largo alcance dentro de sus estructuras cristalinas. Sin embargo, los estudios de Yoshida y col. demostraron que disminuyendo el tamaño del radical del catión imidazolio, el compuesto 1-etil-3-metilimidazolio tetracloroferrato (Emim$[FeCl_4]$) y su análogo con bromo, presentaban un ordenamiento antiferromagnético de largo alcance. Este hecho

nos llevó a interesarnos por comprender su origen, ya que abría nuevas posibilidades para el diseño de nuevos MILs con temperaturas de ordenamiento magnético más altas o la posibilidad de encontrar coexistencia de ordenamientos magnéticos tridimensionales con otras propiedades interesantes como la polaridad eléctrica.

De esta forma, la presente memoria está centrada en estudio multidisciplinar que incluye la síntesis, la caracterización de las propiedades físico-químicas y el estudio de las propiedades magnéticas y de las correlaciones magnético-estructurales en nuevos MILs basados en cationes de imidazolio y aniones de tetracloro y tetrabromoferrato.

1.2. Síntesis y Técnicas experimentales

1.2.1. Síntesis de MILs

En la actualidad, el método más empleado de síntesis de MILs consiste en una reacción sólido-sólido en atmósfera inerte mediante calentamiento térmico a temperaturas moderadas[9]. De los diferentes pasos necesarios para abordar este fin, el más complejo es el de obtener las sales orgánicas de partida, ya que la mayoría no son comerciales. Además, dependiendo del grado de pureza o complejidad, su preparación puede llevar a su vez varias pasos preliminares, aumentando considerablemente su precio. En la figura 1.1 se muestran los cationes utilizados en la síntesis de los MILs de la presente memoria, los cuales han sido sintetizados en el Instituto de Química de la Universidad Federal de Rio Grande da Sul (UFRGS). Este centro se dedica desde 1994 a la investigación en el campo del diseño y síntesis de líquidos iónicos con especial énfasis en catálisis organometálica.

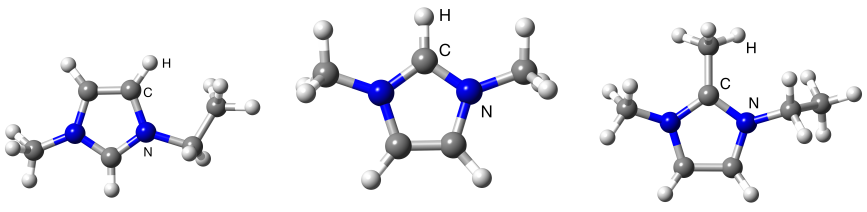

(A) (B) (C)

FIGURA 1.1: Cationes orgánicos utilizados en la presente memoria: (a) $Emim^+$, (b) $Dimim^+$, (c) $Edimim^+$

Dentro de las sales inorgánicas utilizadas en la síntesis de MILs, las de hierro[7] son los más demandadas debido a sus potenciales aplicaciones tecnológicas, abundancia y bajo coste. Entre ellas los complejos metálicos $[FeCl_4]^-$ y $[FeBr_4]^-$ son los más utilizados. Para su obtención, es necesario partir de una sal anhidra de $FeCl_3$ o $FeBr_3$, la cual se conjuga con el contraión de la sal orgánica utilizada mediante la reacción de la figura 1.2.

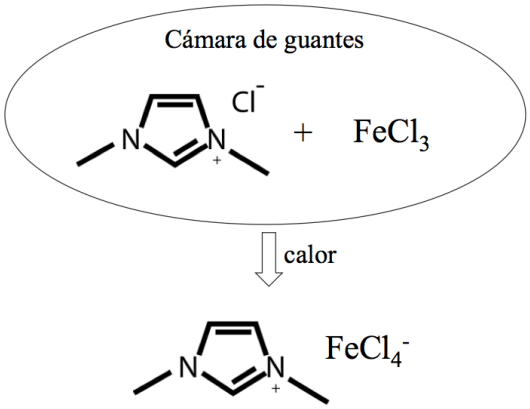

(A)

FIGURA 1.2: Síntesis del compuesto 1,3-dimetilimidazolio tetracloroferrato

Para el trabajo expuesto en la presente memoria, ha sido necesario sintetizar 4 nuevos MILs, el 1,3-dimetilimidazolio tetracloroferrato, 1,3-dimetilimidazolio tetrabromoferrato, 1-etil-2,3-dimetilimidazolio tetracloroferrato y el 1-etil-2,3-dimetilimidazolio tetrabromoferrato, denominados Dimim$[FeCl_4]$, Dimim$[FeBr_4]$, Edimim$[FeCl_4]$, Edimim$[FeBr_4]$ respectivamente.

Dado el carácter higroscópico de las sales de imidazolio, la manipulación se realiza en una cámara de guantes en atmósfera inerte mezclando cantidades equimoleculares de las sales orgánicas e inorgánicas de partida. Algunas reaccionan exotérmicamente convirtiéndose en líquido a temperatura ambiente (caso Emim$[FeCl_4]$). Otras es necesario introducirlas en recipientes herméticos y someterlas fuera de la cámara, en baño de aceite, a una temperatura menor que los 150^{o}C para evitar la descomposición del compuesto.

1.2.2. Caracterización físico-química

Una vez que se han sintetizado las muestras, se procede con una caracterización tanto química como física para comprobar si el resultado obtenido es el deseado. Las técnicas

utilizadas han sido:

- **Análisis químico elemental**. Es una técnica que permite obtener el contenido de hidrógeno, carbono, nitrógeno y azufre en las muestras.
- **Espectroscopia óptica atómica**. Mediante un proceso de atomización, las muestras se convierten en iones gaseosos de los cuales se puede obtener la proporción de un determinado átomo en el compuesto. Esta técnica se utilizó para determinar la cantidad de hierro, cloro o bromo en la muestra.
- **Técnicas vibracionales: espectroscopias Raman e infrarrojas**. Permiten identificar los modos de vibración de los aniones y cationes que componen la muestra. Con ello se consigue caracterizar los grupos funcionales específicos[10] y saber si se han formado correctamente. En el caso de los cationes de imidazolio aparece un amplio espectro de modos en la zona de altas energías (3000-3500 cm^{-1}) relacionado con las vibraciones C-H de los radicales etil y metil. Las vibraciones Metal-Cl son más fuertes, por lo que el anión puede caracterizarse someramente. En el caso de un compuesto con $[FeCl_4]^-$ con simetría tetragonal, aparecen 4 bandas bien definidas activas en Raman en un rango de energías entre 100 y 400 cm^{-1}.
- **Análisis térmico**. Por un lado se tiene la Calorimetría Diferencial de Barrido (DSC), que permite detectar las transiciones de fase en la muestra. Por otro lado se encuentra la Termogravimetría (TG), que permite obtener el rango de estabilidad de los compuestos e incluso en el caso de nuestras muestras, si han absorbido agua en el proceso de síntesis.

1.2.3. Caracterización estructural

La determinación de la estructura cristalina es fundamental para poder entender las interacciones intermoleculares y las propiedades físico-químicas de los compuestos. Por este motivo, una vez preparados los MILs, uno de los primeros pasos es el estudio estructural de su fase condensada. Para ello hemos realizado medidas de difracción en polvo utilizando tanto rayos X como neutrones.

1.2.3.1. Difracción de Rayos X

La difracción de rayos X es una técnica que permite, entre otras cosas, el estudio cristalográfico de un material. La primera ventaja de esta técnica es que se encuentra disponible en la mayoría de centros de investigación y permite obtener una primera estimación del grupo espacial de la muestra. En la presente memoria, se empleó un difractómetro D8 Advance de Bruker equipado con una cámara que permite llegar a la temperatura de nitrógeno líquido (77 K) y utilizando una longitud de onda de 1.5418 Å. En los primeros análisis se encontró que la resolución de los espectros obtenidos, dada la complejidad de la estructura cristalina, era baja para abordar el estudio cristalográfico. Por este motivo, para disponer de difractogramas de mejor calidad, se tuvieron que realizar propuestas a grandes instalaciones. En este caso, se realizaron medidas de difracción en el sincrotrón ALBA de Barcelona, obteniendo diagramas de difracción de gran calidad y en un rango amplio de temperaturas. La principal desventaja de esta técnica es que no es posible localizar los hidrógenos y puede resultar complicado diferenciar átomos próximos en la tabla periódica. Esto es debido a que los rayos X son difractados por los electrones de los átomos.

1.2.3.2. Difracción de Neutrones

La difracción de neutrones puede utilizarse como una técnica complementaria a la difracción de rayos X para determinar la estructura cristalina de un material. Aunque esta técnica necesita un tiempo de adquisición mayor que el de los rayos X de sincrotrón, los neutrones interaccionan directamente con el núcleo del átomo pudiendo diferenciar isótopos. Además, los átomos ligeros suelen contribuir de manera más fuerte a la intensidad difractada, por lo que es ideal para localizar los átomos de hidrógeno. Para realizar experimentos de difracción en polvo de neutrones hace falta solicitar tiempo en grandes instalaciones, como el Instituto Laue-Langevin (ILL). Las medidas de la presente memoria se realizaron principalmente en los equipos D1B de alto flujo y D2B de alta resolución en el centro mencionado. Otra ventaja de la difracción de neutrones es que al poseer los neutrones espín, éstos interaccionan con los momentos magnéticos del material, dando lugar a un scattering magnético. Si los materiales poseen orden magnético de largo alcance, el scattering magnético da lugar a picos de difracción que pueden superponerse a los ya existentes cristalinos o aparecer en nuevas posiciones angulares, dependiendo del tipo de ordenamiento magnético. Es decir, la difracción de neutrones permite obtener la estructura magnética del material.

1.2.3.3. Análisis de los diagramas de difracción

Los análisis de los diagramas de difracción de rayos X y de neutrones se llevaron a cabo mediante la técnica de refinamiento propuesta por H.M. Rietveld con el programa Fullprof[11]. Mediante un ajuste por mínimos cuadrados, se ajusta el difractograma completo de polvo tanto para rayos X como neutrones respecto a un perfil teórico. Sin embargo, dada la complejidad de nuestras estructuras se optó por complementar el estudio de los difractogramas mediante los programas DAjust[12], Ribols[13], TALP[14], XLENS[15] [16]. El programa DAjust se utiliza para extraer las intensidades de los picos de difracción que son introducidas en el programa TALP, que es un software que resuelve la estructura cristalina mediante una exploración en el espacio directo y que permite definir las restricciones moleculares con relativa sencillez. Si los picos de difracción no muestran solape y tienen buena resolución, se puede utilizar el software XLENS, que realiza una exploración por métodos directos. Con el resultado obtenido tanto del TALP o del XLENS, se refina el diagrama mediante el software Ribols, basado también en el método Rietveld.

1.2.4. Propiedades magnéticas

Una parte importante de esta tesis se centra en el estudio magnético de los MILs. Las principales técnicas empleadas se describen a continuación.

1.2.4.1. Magnetometría

Las medidas de susceptibilidad magnética e imanación permiten caracterizar magnéticamente el compuesto, obteniendo su comportamiento magnético en función de la temperatura o campo magnético. Un proceso típico de medida es el ciclo zero field cooling - field cooling (ZFC-FC) que consiste en ver la diferencia de la respuesta magnética al calentar un material en presencia de un campo magnético cuando previamente se ha enfriado con campo (FC) o sin campo magnético (ZFC). El resultado de este proceso nos da una idea del carácter ferromagnético de la muestra, dado que si ésta presenta ferromagnetismo o ferrimagnetismo, habrá una diferencia en las curvas de susceptibilidad asociadas a la presencia de dominios magnéticos. Otra técnica común es medir la imanación en función del campo magnético a una temperatura constante. Ésta nos permite conocer por un lado el momento de saturación, y por otro, si tenemos un compuesto

ferromagnético, aparecerá una irreversibilidad en la curva de imanación, que da lugar a la aparición de un campo coercitivo, que no ocurre cuando se trata de un compuesto antiferromagnético.

Los procesos anteriores se estudian con campos magnéticos estáticos (medidas en DC). Sin embargo, también pueden realizarse medidas con campos alternos (medidas en AC). Este modo de medida permite estudiar comportamientos dinámicos en la muestra realizando medidas para diferentes frecuencias de oscilación del campo magnético.

A partir de un ajuste a una ley de Curie-Weiss en la zona paramagnética se puede obtener el momento paramagnético efectivo (μ_{eff}) que presentan los aniones magnéticos y la temperatura de Curie paramagnética (θ_P) que nos da idea de si las interacciones son de tipo ferro o antiferromagnético.

Las medidas de susceptibilidad magnética fueron realizadas tanto en un magnétometro multipropósito PPMS de Quantum Design, que permite aplicar campos de hasta 90 kOe y temperaturas en un rango de 1.9 a 400 K, como en un magnetómetro SQUID, que es el detector de campos magnéticos más precisos (hasta 10^{-7} emu en condiciones óptimas).

1.2.4.2. Calor específico

Las medidas de calor específico se realizaron mediante un método de relajación en un equipo PPMS de Quantum Design. Se basa en un principio por el cual se aporta una determinada cantidad de calor a la muestra que se encuentra pegada con una pequeña cantidad de grasa a una plataforma. El sistema mide el incremento de la temperatura de la muestra y su posterior relajación, calculando automáticamente el calor específico del conjunto plataforma-grasa-muestra. Finalmente, substrayendo el calor específico de la plataforma-grasa, que se mide previamente, se obtiene la contribución de la muestra. El calor específico es una propiedad que da información interesante sobre los comportamientos magnéticos. Así por ejemplo, cuando tenemos una transición desde una fase con ordenamiento magnético tridimensional a la fase paramagnética, aparece un pico en el calor específico que se conoce como anomalía lambda. Si existe un ordenamiento magnético de corto alcance por encima de la temperatura de orden, éste da lugar a una contribución adicional en el calor específico, es decir, la anomalía lambda tiene una "cola" que se extiende por encima de la temperatura de orden. Para analizar la contribución magnética al calor específico, previamente hay que calcular la correspondiente

a la red, generalmente mediante un ajuste a una ley de Debye. Con la contribución restante (magnética), integrando C_m/T en función de la temperatura, se obtiene la entropía asociada al ordenamiento magnético, que da cuenta del espín del anión magnético de la muestra y por tanto, permite caracterizar el estado de oxidación del anión metálico.

1.2.4.3. Mössbauer

La espectroscía Mössbauer es una técnica que se basa en la emisión y absorción resonante de rayos gamma libres de retroceso de los átomos de un compuesto. Presenta una resolución muy fina de energía pudiendo caracterizar el entorno nuclear de los átomos. En el caso del hierro magnéticamente ordenado con un estado de oxidación (III), el espectro muestra 6 picos característicos. Cualquier variación, ya sea impurezas magnéticas, que todos los hierros no estén ordenados, etc., repercuten en el espectro final como contribuciones extra. Esto implica que ajustando el conjunto de picos se puede obtener la concentración de cada estado de oxidación de la muestra.

1.3. Cálculos *ab initio* del funcional de la densidad

Como se ha mencionado anteriormente, las propiedades de un material están determinadas por el tipo de ordenamiento cristalográfico que presentan. Este orden es debido tanto a las interacciones intramoleculares como intermoleculares, las cuales llevan a los átomos y moléculas a disponerse en un determinado orden minimizando sus energías. Entender estas interacciones o enlaces da un conocimiento de la relación estructura-propiedad representando una alternativa creativa para diseñar nuevos materiales, lo que repercute en una mejora de sus aplicaciones tecnológicas. Dentro de los líquidos iónicos, numerosos grupos de investigación se han centrado en el estudio de fuerzas del tipo Coulombianas, van der Waals (vdW) o puentes de hidrógeno[17][18]. Sin embargo, en los MILs basados en halometalatos MX_4 (M = metal y X = halógeno) y cationes imidazolio, hace falta considerar otros tipos de interacciones no enlazantes, tales como las halógeno-halógeno[19] (entre dos halógenos de dos aniones vecinos) o anión-π[20] (entre un halógeno y el anillo aromático del imidazolio), ya que también contribuyen en la estabilización de sus estructuras cristalinas[21]. Aunque se han realizado muchos experimentos para determinar las interacciones dentro de los ILs con cationes imidazolio, por ejemplo la metilación de los anillos aromáticos en distintas posiciones para detectar los cambios en los puentes de hidrógeno mediante un estudio vibracional, todavía es

un gran desafío entender estos compuestos a nivel molecular[22]. Para ello las investigaciones experimentales se apoyan en los cálculos teóricos (más económicos y sencillos), que dan abundante información sobre las relaciones entre las estructuras y propiedades. Las métodos más populares son la dinámica molecular y simulaciones de Monte Carlo, pero tienen el inconveniente de que dependen fuertemente de la calidad de las funciones potenciales empleadas y las cargas asociadas. Una mejor estrategia es la de utilizar cálculos *ab initio* del funcional de la densidad (DFT) basados en un método numérico de orbitales atómicos implementados en el código SIESTA[23]. Se ha comprobado esta aproximación en varios ILs basados en imidazolio[24] utilizando una implementación eficiente del funcional de la densidad que permite calcular las interacciones de vdW desarrollado por Dion et al.[25]. Los cálculos teóricos han mostrado interesantes resultados sobre el establecimiento de los puentes de hidrógeno, los cuales son esenciales en las características estructurales de los ILs. Dado que la difracción de rayos X no permite conocer la posición de los hidrógenos, y que las medidas de difracción de neutrones en estas muestras no dan suficiente resolución para determinarlos, los cálculos teóricos son un complemento perfecto para colocarlos y refinar sus posiciones atómicas. Desde el punto de vista magnético, viendo que las distancias entre metales son demasiado grandes para que haya una interacción directa, hace falta buscar un mecanismo indirecto de transmisión magnética en los MILs. En compuestos similares, mediante difracción de neutrones polarizados[26] y corroborado por cálculos teóricos, se observa que esta transmisión de las interacciones magnéticas está favorecida por una deslocalización de la carga del metal al halógeno, dando lugar a interacciones halógeno-halógeno. Los cálculos DFT permiten cuantificar esta deslocalización y comprender mejor los mecanismos de transmisión de estas interacciones magnéticas.

1.4. Correlaciones magnetoestructurales

En la actualidad, el estudio de las correlaciones magnetoestructurales en materiales híbridos orgánico-inorgánicos está atrayendo interés de la comunidad científica. En el caso de los MILs estudiados en la presente memoria, las distancias entre dos hierros vecinos varían entre 6 y 8 Å, lo que descarta interacciones directas entre hierros. Es por tanto necesario considerar otro tipo de mecanismos de interacción magnética, como son las interacciones de supercanje directas (Fe-X–X-Fe) y las interacciones de supercanje indirectas (Fe-X–Im–X-Fe) (X = halógeno, Im = Imidazolio)[27]. Un factor importante que determina el tipo de interacción magnética es el ángulo que forman los metales

y halógenos en los caminos de supercanje. De esta manera, ángulos próximos a 90º (condición de ortogonalidad)[28], presentan un carácter ferromagnético, mientras que los cercanos a 180º, son de tipo antiferromagnético. Cualquier situación intermedia puede dar lugar a una competencia entre ambos ordenamientos, la cual se puede analizar cualitativamente.

Finalmente, se puede determinar de manera cuantitativa la fuerza de la interacción magnética en un compuesto por medio de un ajuste a la susceptibilidad magnética a un modelo teórico asociado con su estructura cristalina y el tipo de interacción magnética que presenta.

Capítulo 2

Emim[$FeCl_4$]

2.1. Introducción

El 1-etil-3-metilimidazolio tetracloroferrato (Emim[$FeCl_4$]) es un compuesto comercial que se encuentra en estado líquido a temperatura ambiente. Está formado por un catión orgánico ($Emim^+$) y por un anión que contiene un metal de transición, en este caso hierro. Fue el primer compuesto encontrado dentro de los MILs que presentaba ordenamiento magnético de largo alcance (antiferromagnético) a una temperatura de 4 K [29].

Un estudio magnético más completo fue realizado en 2011 por nuestro grupo de investigación [30] [31]. En los datos obtenidos se corroboró que la temperatura de ordenamiento magnético estaba por debajo de 4.2 K. La ausencia de histéresis en las curvas de imanación vs. campo magnético aplicado (M(H)), unido a las medidas de la susceptibilidad AC, en las que no se observa una dependencia con la frecuencia, confirmaron que el ordenamiento es antiferromagnético, descartando un estado spin-glass. Asimismo las medidas de calor específico aportaron valiosa información sobre la transición líquido-sólido y la posterior sólido-sólido que establece una estructura cristalina que permanece estable hasta bajas temperaturas.

Entrando en el trabajo realizado en la presente memoria, inicialmente se realizó un estudio del comportamiento magnético del Emim[$FeCl_4$] al aplicarle una presión hidrostática. Este tema se trata en el artículo publicado en la revista *J. Phys. Chem. B* (Artículo I). El principal resultado obtenido de este estudio es que el ordenamiento tridimensional se

ve fuertemente alterado, induciendo una transición desde un orden 3D antiferromagnético a uno ferrimagnético por encima de 3.4 kbar, con un incremento de la temperatura de orden de aproximadamente un 40 %. Además, se realizaron en este trabajo medidas de espectometría Raman con presión revelando un interesante resultado: los aniones $FeCl_4$ se mantienen aislados tanto en los estados líquido como sólido, sugiriendo que los caminos de supercanje están mediados a través de puentes Fe-Cl–Cl-Fe. Por último se detectó que la transición sólido-líquido se desplazaba hacia temperaturas inferiores al aplicar presión, añadiendo una histéresis magnética al proceso.

Posteriormente, para intentar dilucidad la transición sólido-sólido que presenta este MIL por debajo de 220 K, se realizaron medidas de difracción de rayos X en un difractómetro D8 advance a temperatura del nitrógeno líquido (77 K) con una longitud de onda de 1.5418 Å. Los diagramas de difracción mostraban un cambio de simetría con respecto a los resultados publicados por Tobias Bäcker y colaboradores[32]. Sin embargo, dada la poca resolución del espectro obtenida fue imposible resolver su estructura cristalina. Para obtener una mejor calidad de datos de difracción, se realizaron experimentos de difracción de rayos X en el sincrotrón ALBA y de difracción de neutrones en el ILL.

Los resultados de las medidas de difracción de Rayos X en sincotrón obtenidos presentaban orientaciones preferenciales, lo que complicaba la resolución de la estructura cristalina de baja temperatura. Por otro lado, los experimentos de difracción de neutrones mostraban un scattering incoherente muy grande, debido al gran número de hidrógenos que presenta el imidazolio, que perjudicaba la calidad de los datos. Por ello se abordó un segundo estudio de difracción de neutrones con una deuteración del Emim[$FeCl_4$] en dos variantes, una completamente deuterada y otra con deuteración parcial, en la cual sólo los hidrógenos del anillo aromático quedaban sin deuterar. Las medidas magnéticas dieron como resultado órdenes magnéticos similares, con alguna variación en los valores absolutos de la susceptibilidad magnética. En las medidas de difracción de neutrones se consiguió, por un lado, una disminución del fondo que se debía a la dispersión incoherente del hidrógeno, pero por otro lado, comparando los diagramas de difracción de las muestras deuteradas y sin deuterar, se observaba que las estructuras cristalinas eran diferentes. Estos resultados preliminares han sido recientemente publicados en la revista *Journal of Physics: Conference Series* (Artículo II). La resolución estructural, aún en proceso, permitirá obtener información de los cambios estructurales en función de la deuteración del compuesto y la estructura magnética del compuesto sin deuterar.

2.2. Artículo I

Artículo publicado en la revista *The Journal of Physical Chemistry B*: “Pressure Effects on Emim[$FeCl_4$], a Magnetic Ionic Liquid with Three- Dimensional Magnetic Ordering”

Pressure Effects on Emim[FeCl4], a Magnetic Ionic Liquid with Three-Dimensional Magnetic Ordering

Abel García-Saiz, Imanol de Pedro, Jesús A. Blanco, Jesús González, Jesús Rodríguez Fernández

J. Phys. Chem. B, 2013, 117, 11, 3198-3206

https://doi.org/10.1021/jp3114623

Supplementary material

Figure S1. Crystal structure below 280 K of Emim[$FeCl_4$] in the b,c projection.
Figure S2. Low-temperature ZFC-FC magnetic susceptibility under magnetic fields of 0.01 T and 0.1 T for pressures a) 0.56 GPa and b) 0.77 GPa.
Figure S3. Raman spectrum of Emim[$FeCl_4$] without applied pressure at room temperature.

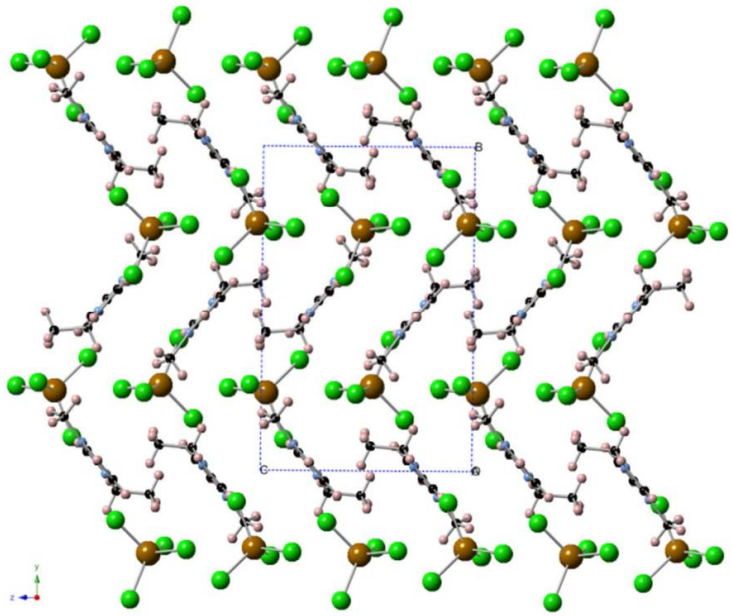

Figure S1

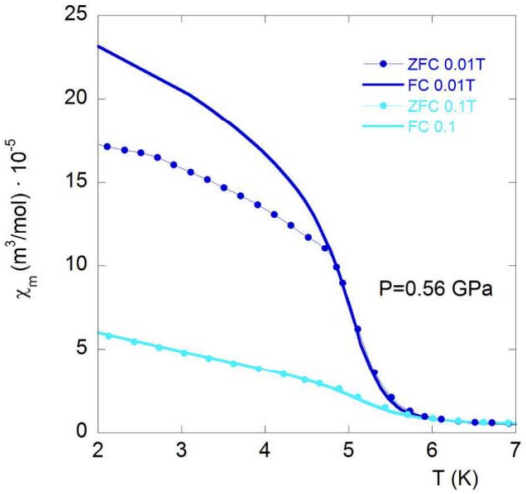

Figure S2 (a)

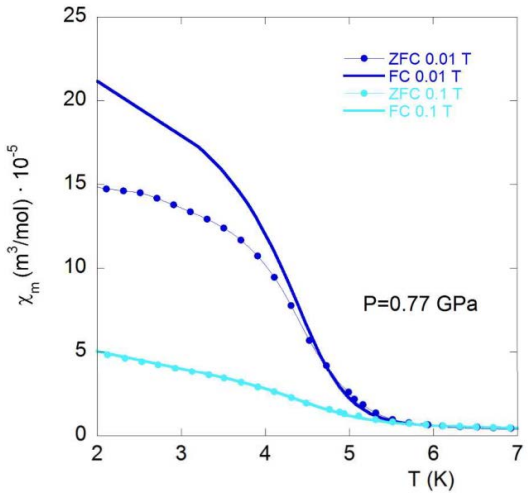

Figure S2(b)

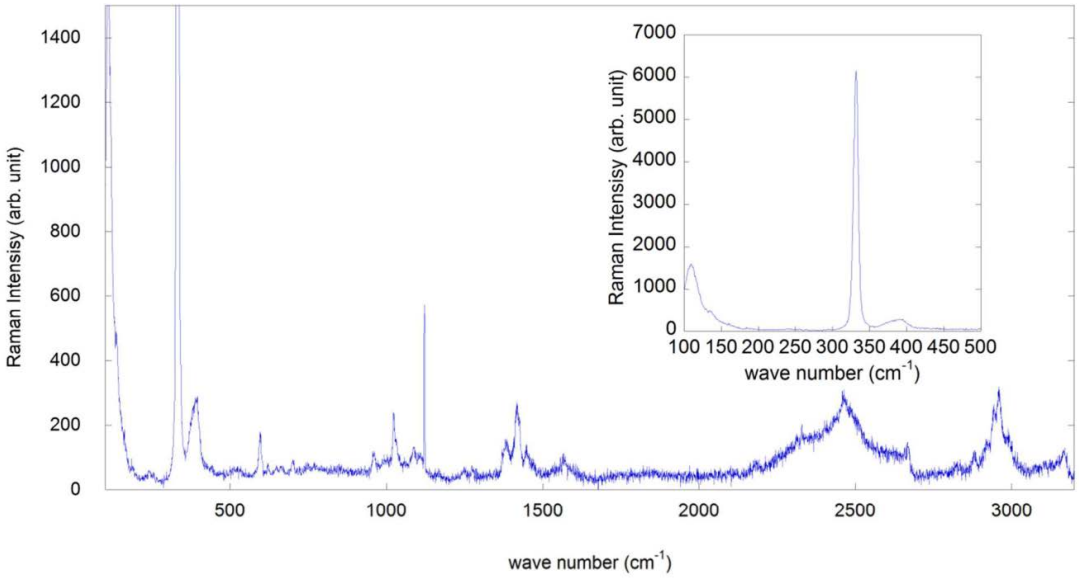

Figure S3

2.3. Artículo II

Artículo publicado en la revista *Journal of Physics: Conference Series*: "Neutron Powder Diffraction study of the Magnetic Ionic Liquid Emim[FeCl4] and its deuterated phase"

7th Meeting of the Spanish Neutron Scattering Association (SETN) IOP Publishing
Journal of Physics: Conference Series **663** (2015) 012008 doi:10.1088/1742-6596/663/1/012008

Neutron Powder Diffraction study of the Magnetic Ionic Liquid Emim[$FeCl_4$] and its deuterated phase

A. García-Saiz[1], I. de Pedro[*1], L. Fernández Barquín[1], M.T. Fernández-Díaz[2] J. A. Blanco[3] and J. Rodríguez Fernández[1]
[1] CITIMAC, Facultad de Ciencias, Universidad de Cantabria, Santander 39005, Spain.
[2] Institut Laue-Langevin, BP 156X, F-38042 Grenoble Cedex, France
[3] Departamento de Física, Universidad de Oviedo, 33007 Oviedo, Spain

E-mail: depedrovm@unican.es

Abstract. A magnetic ionic liquid comprising 1-ethyl-3 methylimidazolium (Emim) cations and tetraclhoroferrate(III) ($FeCl_4$) anions and its deuterated phase were synthetized and characterized magnetically. In both materials, the low temperature dependence of the magnetic susceptibility presents a maximum (around 4 K) related to an antiferromagnetic ordering, but the ordering temperatures are slightly shifted and the curves display different shapes. In addition, the magnetization of the deuterated phase tends to saturate at higher values than that corresponding to the non-deuterated analogue. A comparison of the neutron diffraction patterns above and below the magnetic transition clearly shows that the crystal and magnetic structures of these materials are different. Therefore, the present findings clearly prove that the magnetic exchange interactions that induce three-dimensional magnetic ordering are modified after the deuteration process.

1. Introduction

Magnetic ionic liquids (MILs) have received considerable attention among ionic liquids (ILs). The interest is fuelled by the possibility of tuning the materials properties by means of external magnetic fields or using them in the liquid state to produce nanoparticle-free magnetic emulsions and microemulsions [1]. Moreover, MILs can combine magnetic and ILs properties with additional intrinsic thermochromic, magneto-electrochromic or luminescent properties depending on the enclosed paramagnetic ion used [2]. The combinations of different rare-earth (europium, neodymium, dysprosium, etc.) chiral amionacids, bimagnetic ions or heteroanions have been studied for applications such as transport and separation of materials, separation of greenhouse gases (CO_2) through supported magnetic ionic liquids membranes, magnetic surfactants or esterification of oleic acid to biodiesel [3].

MILs have also recently received attention from the experimental and theoretical point of view concerning to non-covalent interactions and cohesion properties [4]. Many groups have focused their studies on the dipole-dipole interactions, and hydrogen bonds within the crystal and molecular structures in order to improve the understanding of these forces, with the aim of tailoring their potential technological applications [5]. Importantly, in MILs with paramagnetic ions, such as those presented here, it is also necessary to investigate other non-covalent interactions, like halogen-halogen

7th Meeting of the Spanish Neutron Scattering Association (SETN) IOP Publishing
Journal of Physics: Conference Series **663** (2015) 012008 doi:10.1088/1742-6596/663/1/012008

(between the nearest metal complex anions) or anion-π (between the anion and cation) as these forces play an important role in the organization of the structural units [6]. In addition, when these interactions are strong enough, interesting collective electrical and magnetic phenomena can arise, such as ferroelectricity in the bis(imidazolium) pentachloroantimonate (III), $(C_3N_2H_5)_2SbCl_5$ [7], or a three-dimensional (3D) magnetic ordering in MILs based on tetrahaloferrate ions [8, 9]. In this last family, recent research shows that a smaller chain length in the organic cation enhances the efficiency in the transmission of the magnetic interactions resulting in an increase in the Néel temperature, T_N (from $[Bmim]^+$ that shows no 3D magnetic ordering through $[Emim]^+$, with T_N = 3.8 K [10], to $[Dimim]^+$, with T_N = 5.6 K [11]) [Bmim: 1-butyl-3-methylimidazolium and Dimim: 1,3-dimethylimidazolium]. Moreover, the change of external conditions, like pressure, has a strong influence in the magnetic coupling of Emim[$FeCl_4$], varying from antiferromagnetic (AF) to ferrimagnetic ordering [12]. In this contribution we focus on ascertaining the nature of the magnetic structure of this last MIL, using neutron diffraction experiments. The presence of H atoms in the cation part (H= 11) of Emim[$FeCl_4$] predicted low statistics in the neutron diffraction pattern. Therefore, in order to avoid the large incoherent component of the hydrogen, which creates a large continuous background and complicates the structural resolution, we have also prepared the fully deuterated sample, Emim[$FeCl_4$] d11. Herein, we present the comparative study considering magnetic susceptibility and neutron powder diffraction data.

2. Results and discussion

The zero-field-cooled (ZFC) molar susceptibility (χ_m) at magnetic field of 1 kOe of Emim[$FeCl_4$] d11 displays a paramagnetic behaviour over most of the temperature range studied, with an effective paramagnetic moment, μ_{eff} = 5.70(1) μ_B/Fe ion, and a paramagnetic Curie temperature, θ_p = -3.0(1) K. These data anticipate an overall antiferromagnetic behaviour in good agreement with their non-deuterated phase (μ_{eff} = 5.66(1) μ_B/Fe ion and and θ_p = -2.5(1) K) [8, 9]. At low temperatures (see Figure 1), χ_m of Emim[$FeCl_4$] d11 increases and reaches a maximum at approximately 4.0 K, which suggests the existence of a long-range magnetic ordering. The most striking features of these curves being a small displacement of ordering temperature and the different shape with respect to the non-deuterated phase. These facts indicate that the magnetic coupling is modified with the deuteration process. Moreover, the magnetization of Emim[$FeCl_4$] d11 tends to saturate above 40 kOe, with higher values than those corresponding to the non-deuterated analogue (M ≈ 4.9 μ_B/Fe ion), and it is near the expected fully-saturated value of 5 μ_B/Fe for Fe (III) ion (see Figure 2). As occurs in the non-deuterated compound, the magnetization shows no-hysteresis, thereby discarding the existence of any ferromagnetic component.

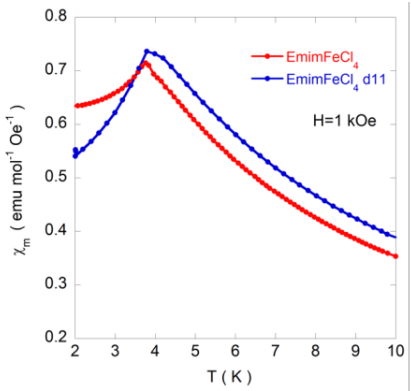

Figure 1. Low temperature ZFC magnetic susceptibility for Emin[$FeCl_4$] and its deuterated phase.

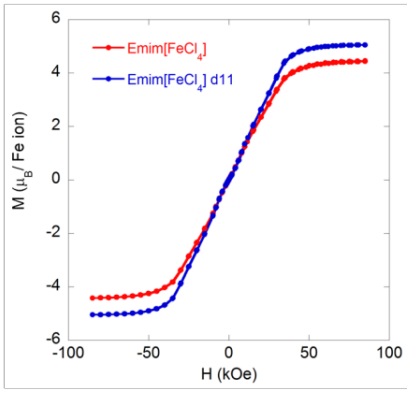

Figure 2. Magnetization of Emin[$FeCl_4$] and its deuterated phase measured at 2 K.

7th Meeting of the Spanish Neutron Scattering Association (SETN) IOP Publishing
Journal of Physics: Conference Series **663** (2015) 012008 doi:10.1088/1742-6596/663/1/012008

Neutron powder diffraction patterns of Emim[$FeCl_4$], from 270 to 2 K, and of deuterated analogue at 10 and 2 K were collected on D1B diffractometer at the ILL (λ = 2.52 Å). In these experiments, about 2 g of the sample mass was frozen and then milled before it placing in a cylindrical vanadium container pre-cooled at N_2 liquid. The samples were rapidly placed in the cryostat at temperature below the melting point (285K), checking that no preferential orientation was present. The diffraction patterns were collected in the Bragg angular range $5 \leq 2\theta \leq 70^{\circ}$. The 2D contour plots of the temperature dependence of the neutron diffraction data of the non-deuterated compound is shown in Figure 3). On one hand, a structural phase transition below 210 K is detected in the neutron diffraction patterns, which seems to be stable down to 2 K. This feature could be related to dynamical reorientations of the cations or anions during the cooling process. Therefore, the appearance of a new peak at lower angle regions at 14.5° (d = 10.06 Å) and the splitting of some crystallographic peaks (such as the one located at $2\theta \approx 45^{\circ}$) could be indicative of a loss of symmetry. This issue differs from the data reported for the Dimim[$FeCl_4$] [11], in which the structural phase transition changes the symmetry from $P2_1$ (R.T) to $P2_12_12_1$ at 285 K. Additionally, the presence of extra magnetic signals below 4 K reveals the occurrence of a long-range magnetic ordering compatible with the magnetization results.

The high temperature crystal structure was refined starting from the previously reported single-crystal structure model [13]. The best Rietveld refinement from powder diffraction data at 270 K a framework, which projected along *b* axis, can be described as a stacking of $[Edimim]^+$ and $[FeCl_4]^-$ intercalated layers, with Fe···Fe distances larger than 6.5 Å inside the layer [monoclinic space group $P2_1/c$; a = 9.424(3) Å, b = 14.662(4) Å, c = 12.449(9) Å, β = 129.89(2)° , V= 1319.2(4) $Å^3$]. The anion groups $[FeCl_4]^-$, slightly distorted, form subnets in the *a,c* plane with a change of orientation from layer to layer and a displacement of the subnet with respect to the next one. The cations, $[Emim]^+$, also form subnets in the *a,c* plane but are stacked nearly identically above one another, lying parallel to each other along *b* direction (see Figure 4) in good agreement with single-crystal structure model.

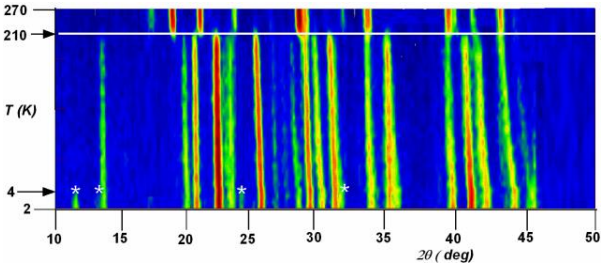

Figure 3. 2D contours of the temperature dependence of the D1B patterns between 270 and 2 K for [Emim][$FeCl_4$]. The (*) dots show the magnetic contributions. The line at 210 K shows the change of the crystalline structure.

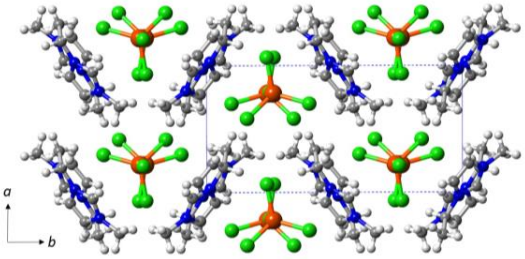

Figure 4. Crystal packing in the *a,b* plane of Emimim[$FeCl_4$] crystal structure at 270 K. Red (iron), green (chloride), black (carbon), blue (nitrogen) and white (hydrogen). The blue dashed square represent the unit cell.

A comparison of the D1B patterns for Emin[$FeCl_4$] (red) and its deuterated phase (blue) at 2 K is plotted in Figure 5. The data clearly show differences in the structural and magnetic peaks. Therefore, the intermolecular interactions between anions and cations (ionic, hydrogen bonding and van der Waals forces) are modified with the deuteration process. These forces affect the local- and long-range molecular ordering, which subsequently modify the magnetic couplings between an iron ion and its first shell of neighbouring iron ions changing the superexchange anion-anion interactions [14]. In order to try to resolve the low temperature crystal structure of both MILs, high-resolution neutron diffraction data at 10 K on D2B (λ = 1.594 Å) were collected (see Figure 6). A comparative view of

7th Meeting of the Spanish Neutron Scattering Association (SETN) IOP Publishing
Journal of Physics: Conference Series **663** (2015) 012008 doi:10.1088/1742-6596/663/1/012008

the patterns clearly shows a better signal/ratio in the deuterated phase and confirms the different low temperature crystal structures.

Only for the deuterated compound was found a satisfactory monoclinic crystal structure [M20 =16.8; F20 = 10.6] using the WINPLOTR programme [15], with unit cell parameters of a = 9.560 (1) Å, b =13.946 (1) Å, c = 14.460 (1) Å, β = 97.13(1). The analysis was consistent with the $P2_1/m$ space group. The experimental, calculated and difference diffraction profiles are displayed in Figures 5 and 6 and the resolution of the crystal structure is now in progress. Focusing on the long-range magnetic ordering of the deuterated phase, below T_N, the additional magnetic peaks can be indexed with the propagation vector k = (0.5, 0, 0.5) (Figure 5), indicating that the magnetic unit cells is twice larger than the crystallographic one in a and c directions. This approach allows us to see some important differences when compared to Dimim[$FeBr_4$] analogous [6], in which the magnetic and nuclear unit cells are the same.

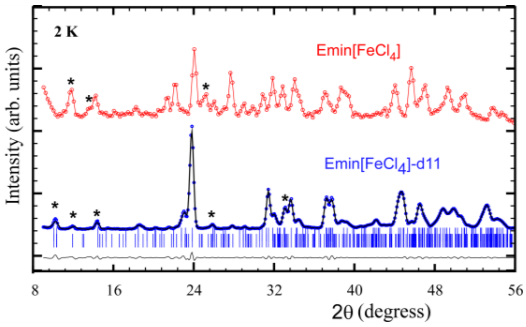

Figure 5. Neutron pattern for Emim[$FeCl_4$] and neutron diffraction profiles for the deuterated phase at 2 K obtained in D1B (λ = 2.52 Å). Positions of the magnetic (second row) profile are also presented. The (*) dots show the magnetic bragg peaks. The curves are shifted for clarity.

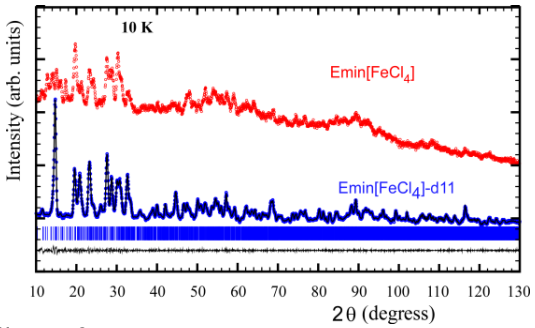

Figure 6. Neutron pattern for Emim[$FeCl_4$] and neutron diffraction profiles for the deuterated phase at 10 K obtained in D2B(λ = 1.594 Å). The curves are shifted for clarity.

3. Conclusions

Neutron data evidence a solid-solid transition in Emim[$FeCl_4$] near 210 K, this crystal structure being stable down to 2 K. The appearance of extra magnetic peaks below 4K in neutron diffraction data confirms the onset of a three-dimensional antiferromagnetic ordering. Finally, we have identified via magnetic and powder diffraction studies that these MILs change their magnetic behaviour with the deuteration process. The 3D antiferromagnetic ordering detected by magnetic measurements must take place via super-exchange coupling, the Fe–Cl···Cl–Fe interaction being the main exchange pathway. In addition, indirect exchange coupling of the type Fe-Cl···Im···Cl-Fe (Im = Imidazolium) could be present in both compounds. Taking in account that the strength of the magnetic exchange pathways via these super-exchange couplings depend on the following paramenters: (i) Cl ··· Cl distance, (ii) Fe– Cl ··· Cl –Fe angles and (iii) the Fe– Cl ··· Cl –Fe torsion angle (τ), these distances and angles should be quite similar, as inferred from the magnetic susceptibility measurements, being different their crystal structures. The present findings illustrates very well how small bonding-changes can have a profound effect on both crystal and magnetic structures of these materials whose framework is linked by non-covalent interactions.

7th Meeting of the Spanish Neutron Scattering Association (SETN) IOP Publishing
Journal of Physics: Conference Series **663** (2015) 012008 doi:10.1088/1742-6596/663/1/012008

4. Acknowledgements

Part of this work was carried out at Institute Laue-Langevin (ILL) of Grenoble and was partially financially supported by MEC research project MAT2011-27573-C04.

5. References

[1] Okuhata M, Funasako Y, Takahashi K and Mochida T 2013 *Chem. Commun.* **49** 7662.
[2] Torimoto T, Tsuda T, Okazaki K and Kuwabata S 2010 *Adv. Mater.* **22** 1196.
[3] Santos J, Albo A and Irabien R 2014 *Soc. Chem. Adv.* **4** 40008.
[4] Steed, J W and Atwood J L *Supramolecular chemistry*. John Wiley & Sons: 2009.
[5] Dupont, J 2004 *J. Braz. Chem. Soc* **15** 341.
[6] García-Saiz A, de Pedro I, Migowski P, Vallcorba O, Junquera J, Blanco J A and Rodríguez Fernández, J 2014 *Inorg. Chem.* **53** 8384.
[7] Piecha-Bisiorek A, Jakubas R, Medycki W, Florek-Wojciechowska M, Wojciechowski M and Kruk D 2014. *J. Phys. Chem. A* **118** 3564.
[8] de Pedro I, Rojas D P, Albo J, Luis P, Irabien A, Blanco J A and Rodríguez Fernández, J 2010 *J. Phys.: Condens. Matter* **22(29)** 296006.
[9] de Pedro, I, Rojas D. P, Blanco J A and Rodríguez Fernández, J 2011 *J. Magn. Magn. Mater.* **323** 1254.
[10] Yoshida Y, Otsuka A, Saito G, Natsume S, Nishibori E, Takata M, Sakata M, Takahashi M and Yoko T 2005 *Bull. Chem. Soc. Jpn.* **78**, 1921.
[11] García-Saiz A, Migowski P, Vallcorba O, Junquera J, Blanco J. A, González J. A, Fernández-Díaz M. T, Rius J, Dupont J, Rodríguez Fernández J and de Pedro I 2014 *Chem. Eur. J.* **20** 72.
[12] García-Saiz A, de Pedro I, Blanco J A González J A and Rodríguez Fernández, J 2013 *J. Phys. Chem. B* **117** 3198.
[13] Bäcker T, Breunig O, Valldor M, Merz K, Vasylyeva V and Mudring A. V 2011 *Cryst. Growth & Design* **11(6)** 2564.
[14] García Saiz A, de Pedro I, Vallcorba O, Migowski P, Campo I, Barquin, L F, Abrahams I, Motevalli M, Dupont J, Gonzalez J A, Rodríguez Fernández, J 2015 *RSC Adv.* **5** 60835
[15] Roisnel T. and Rodriguez-Carvajal J 2000 WINPLOTR: A New Tool for Powder Difracction: Laboratoire Leon Brillouin (CEA-CNRS) Centre d'Etudes de Saclay, Gif sur Yvette Cedex, France.
[16] J. Rodríguez-Carvajal, J 1993 *Physica B* **192** 55 and later un-published versions; the programme is a strongly modified version of that described by Wiles D. B. and Young, R. A. 1981, *J. Appl. Crystallogr.* **14** 149.

Capítulo 3

Dimim[$FeCl_4$]

3.1. Introducción

Uno de los objetivos de la presente memoria era la obtención de MILs con ordenes magnéticos tridimensionales a temperaturas más altas que los obtenidos en bibliografía. Para ello se optó en primer lugar por acortar el tamaño del catión imidazolio. Esto a priori, permitiría obtener estructuras más compactas, donde los complejos metálicos estarían más cerca acortando la distancia de los caminos de supercanje Fe-X–X-Fe (X = halógeno), responsables principales de las interacciones magnéticas de largo alcance en los presentes MILs.

Para ello se sintetizó un nuevo MIL, el Dimim[$FeCl_4$] en el cual el radical etilo del Emim se sustituyó por un metilo (ver figura 1.1). El tamaño del radical del catión orgánico, al ser más pequeño también influye en la temperatura de fusión del compuesto, siendo sólido a temperatura ambiente con un punto de fusión de 364 K. Las medidas de imanación muestran un máximo en la susceptibilidad a una temperatura aproximada de 5.6 K, indicando el establecimiento de un ordenamiento 3D antiferromagnético. Comparando este resultado con el obtenido para el Emim[$FeCl_4$] se puede dilucidar que el tamaño del catión influye en las propiedades magnéticas de los compuestos basados en imidazolio y el complejo tetracloroferrato de la siguiente manera: el Bmim[$FeCl_4$] no presenta ordenamiento magnético[29], mientras que el Emim[$FeCl_4$] se ordena a 4 K y el Dimim[$FeCl_4$] a 5.6 K. De esta manera, una menor cadena en el catión imidazolio aumenta el acoplamiento magnético de largo alcance.

Por otro lado los análisis de DSC realizados mostraron una transición sólido-sólido por debajo de la temperatura ambiente. A partir de los estudios de difracción de neutrones, se pudieron resolver las dos estructuras cristalinas. Se observó que el compuesto a temperatura ambiente cristalizaba en una estructura monoclínica con un grupo espacial $P2_1$, mientras que la de 9 K era ortorrómbica con un grupo espacial $P2_12_12_1$. Ambas estructuras se pueden describir por capas de aniones y cationes apiladas a lo largo del eje *b*, en la cual, las distancias más cortas entre hierros son aproximadamente 6 Å dentro de un plano. Además, el eje 2_1 hace que los complejos metálicos $[FeCl_4]^-$ cambien de orientación entre capa y capa. Debido a la complejidad de la estructura cristalina de bajas temperaturas se necesitaron cálculos teóricos del funcional de la densidad (DFT) mediante el código SIESTA[23]. Partiendo de unas coordenadas previas obtenidas a partir de un refinamiento Rietveld y realizando los cálculos DFT con esas coordenadas atómicas, se llegó a un resultado con la suficiente calidad para que un nuevo refinamiento Rietveld permitiera el ajuste de las posiciones de los hidrógenos, fijando las distancias C-H a los valores obtenidos por DFT.

Aparte de utilizarlos para refinar la estructura, estos cálculos teóricos se emplearon para obtener un mapa de la densidad de espín. Se observó que el momento magnético del Fe^{+3} (S = 5/2) está parcialmente deslocalizado en los cloros, debido al enlace covalente entre hierros y cloros. Esta deslocalización magnética se ha detectado en otros compuestos con hierros, como el $K_2FeCl_5{\cdot}H_2O$ o el $Rb_2FeBr_5{\cdot}H_2O$[26], con un porcentaje similar al Dimim[$FeCl_4$]. De esta forma, la transferencia electrónica en este tipo de compuestos fortalece la interacción entre los orbitales magnéticos a través de los caminos de supercanje Fe-Cl–Cl-Fe.

De las diferentes configuraciones magnéticas simuladas por DFT, se encontró que la estructura antiferromagnética de tipo G (antiferromagnética entre planos y dentro del plano) presentaba la configuración más estable, obteniendo una estimación de las constantes de acoplamiento de intercambio. El resultado fue que la interacción más fuerte se da entre los planos, donde el camino de intercambio Fe-Cl–Cl-Fe es prácticamente lineal, aunque la distancia total del camino sea un poco más larga. Dentro de los planos, los hierros se conectan en zig-zag. Sin embargo, este camino está compuesto por una combinación inusual de ángulos de intercambio, uno de ellos aproximándose a los 90º mientras que el otro en torno a 155º. Esto sugiere un debilitamiento del acoplamiento ferromagnético en el plano, coherente con los resultados teóricos del valor de la constante de acoplamiento de intercambio. Todos estos resultados dieron lugar a la publicación III.

Por otro lado, el efecto de la temperatura en la nanoestructura de líquidos iónicos compuestos por imidazolio ha sido examinado a través de numerosos estudios teóricos y experimentales.[33] Se especula que en estos compuestos, los grupos polares forman dominios que se vuelven más organizados a altas temperaturas mientras que los grupos no polares se vuelven menos estructurados. Esto lleva a transiciones de fase, que influyen posteriormente en sus propiedades físico-químicas.

En el caso de los MILs estudiados en la presente memoria se ha observado que la velocidad de enfriamiento influye en la dinámica de los estados sólidos teniendo repercusión en sus propiedades magnéticas a bajas temperaturas. De todos los compuestos analizados, el que presenta una variación más acentuada es el Dimim[$FeCl_4$].

La transición de fase, después de ser enfriada rápidamente en N2 líquido y mantenida estable entre 180 y 240 K, se ha caracterizado combinando rayos X de sincrotrón y difracción de polvo de neutrones. Las estructuras cristalinas obtenidas han sido corroboradas por medio de estudios de la teoría de funcionales de la densidad. Los estudios magnéticos de ambas fases, que muestran un comportamiento antiferromagnético global a baja temperatura pero con importantes cambios en sus temperaturas de orden se han analizado por combinación de magnetometría, Mössbauer y espectroscopia de muones. A través de la difracción de neutrones en polvo no polarizada y polarizada se ha podido dilucidar sus estructuras magnéticas y correlaciones magnetoestructurales. (Artículo anexo en preparación)

3.2. Artículo III

Artículo publicado en la revista *Chemistry—A European Journal*: “A Magnetic Ionic Liquid Based on Tetrachloroferrate Exhibits Three-Dimensional Magnetic Ordering: A Combined Experimental and Theoretical Study of the Magnetic Interaction Mechanism”

ChemPubSoc Europe

DOI: 10.1002/chem.201303602

CHEMISTRY A European Journal Communication

Magnetic Ionic Liquids

A Magnetic Ionic Liquid Based on Tetrachloroferrate Exhibits Three-Dimensional Magnetic Ordering: A Combined Experimental and Theoretical Study of the Magnetic Interaction Mechanism

Abel García-Saiz,[a] Pedro Migowski,[b] Oriol Vallcorba,[c] Javier Junquera,[a] Jesús Angel Blanco,[d] Jesús Antonio González,[a] María Teresa Fernández-Díaz,[e] Jordi Rius,[c] Jairton Dupont,[b] Jesús Rodríguez Fernández,[a] and Imanol de Pedro*[a]

Abstract: A new magnetic ionic liquid (MIL) with 3D antiferromagnetic ordering has been synthetized and characterized. The information obtained from magnetic characterization was supplemented by analysis of DFT calculations and the magneto-structural correlations. The result gives no evidence for direct iron-iron interactions, corroborating that the 3D magnetic ordering in MILs takes place via super-exchange coupling containing two diamagnetic atoms intermediaries.

Responsive materials for which chemical or physical properties can be tuned by applying an external stimulus are appealing in view of their potential applications.[1] New sources of such materials could be the magnetic ionic liquids (MILs), the physicochemical properties (viscosity, melting point, chemical stability, high ion conductivity, etc.) of which can be controlled by external magnetic fields.[2] Typically, MILs are composed of a metal-containing anion (such as iron, cobalt, manganese, copper and so forth) and an organic cation, generally imidazolium, pyrrolidium, pyridinium or tetraalkylphosphonium.[3,4] Nowadays, the development of these MILs has made possible the combination of different rare-earth ions (neodymium, gadolinium, dysprosium),[5] chiral amionacids (MCILs),[6] bimagnetic ions[7] or hetereoanions.[8] Therefore, the synthesis, study and application,[9,10] of these smart materials are increasing exponentially, and it is necessary to provide a complete picture of the crystal structure and the main magnetic interactions in play.

During the last few years, most efforts have focused upon understanding the intermolecular interactions within ILs,[11] including Coulomb, dipole–dipole, van der Waals, dispersion and hydrogen-bond interactions.[12] From a magnetic point of view, the reported crystal structures of most MILs show no magnetic coupling between the paramagnetic metal centres,[3,9,13] since the distances between metal ions are too large (more than 6 Å) to allow significant long-range magnetic interactions. Thus, it was generally assumed that magnetic interactions were negligible in MILs and so they were not expected to exhibit three-dimensional (3D) magnetic ordering. However, the situation changed drastically after the experimental confirmation of a 3D ordering below 4 K[14] in the 1-ethyl-3-methylimidazolium tetrachloroferrate, Emim[$FeCl_4$], and its pressure-induced magnetic transition from antiferromagnetic to ferrimagnetic behaviour.[15] We now address the challenge of understanding the magnetic interactions of MILs with a comprehensive combination of experimental and first-principle-based theoretical methods to unravel the connection between the crystal structure and the magnetic interaction mechanism in a new MIL: 1,3-dimethylimidazolium tetrachloroferrate, Dimim[$FeCl_4$]. We point to the electron-transfer transitions due to a partial covalent bond between the Fe and Cl atoms in $[FeCl_4]^-$ complexes as the driving force for the mechanism of the magnetic interaction in MILs based on tetrachloroferrate exhibiting three-dimensional ordering.

The thermal properties of Dimim[$FeCl_4$] were examined by differential scanning calorimetry (DSC), thermogravimetric analysis (TGA) and heat capacity measurements (Figure S1 to S3 in the Supporting Information, including extra information on the thermal investigations). Two solid–solid (s–s) phase transitions around 332 and 285 K are observed upon cooling from above the melting point (364 K) down to 2 K, in good agreement with other MILs based on imidazolium ions, which indicate several solid–solid transitions detected by thermal analysis.[16] The highest temperature solid phase was labelled phase **III** and the other two phases **II** and **I**, respectively (lowest temperature). The TGA experiment indicates that Dimim[$FeCl_4$] starts to decompose at about 624 K.

[a] *A. García-Saiz, Prof. J. Junquera, Prof. J. A. González, Prof. J. Rodríguez Fernández, Dr. I. de Pedro, Facultad de Ciencias, Universidad de Cantabria, Cantabria Campus Internacional, 39005 Santander (Spain), Fax: (+34) 942-201402, E-mail: depedrovm@unican.es*

[b] *Dr. P. Migowski, Prof. J. Dupont, Universidade Federal do Rio Grande do Sul, Porto Alegre—Rio Grande do Sul, 90040-060 (Brazil)*

[c] *Dr. O. Vallcorba, Prof. J. Rius, Institut de Ciència de Materials de Barcelona (CSIC), Campus de la UAB, 08193 Bellaterra, Catalunya (Spain)*

[d] *Prof. J. A. Blanco, Departamento de Física, Universidad de Oviedo, 33007 Oviedo (Spain)*

[e] *Dr. M. T. Fernández-Díaz, Institut Laue-Langevin, BP 156X, 38042 Grenoble Cedex (France)*

Supporting information for this article is available on the WWW under http://dx.doi.org/10.1002/chem.201303602.

ChemPubSoc Europe

CHEMISTRY A European Journal Communication

The crystal structures of phase **II** and phase **I**, listed in the Supporting Information and CIF files, were resolved from neutron diffraction patterns recorded at room temperature (RT) and 9 K, respectively. Due to the high quality of the data even the hydrogen atoms could be located during the Rietveld refinement. Phase **II** is stable at RT and crystallizes in the non-centrosymmetric monoclinic space group $P2_1$ (No. 4) [a = 6.542(3), b = 14.037(3), c = 6.536(3) Å, β = 90.01(3)°, V = 600.2(4) Å^3, Z = 2, ρ_{calcd} = 1.631 g cm^{-3}, T = 300 K]. Phase **I** crystallizes in the non-centrosymmetric orthorhombic space group $P2_12_12_1$ (No. 19) [a = 9.092(1), b = 13.731(2), c = 8.974(1) Å, V = 1120.2(3) Å^3, Z = 4, ρ_{calcd} = 1.748 g cm^{-3}, T = 9 K]. Both structures can be described as layers of cations and anions stacked along the b axis, with the closest Fe–Fe distances being more than 6 Å inside a layer. The presence of a 2_1 screw axis in both phases yields a change in the orientation of the $[FeCl_4]^-$ metal complex anions from layer to layer (see inset of Figure 1 and

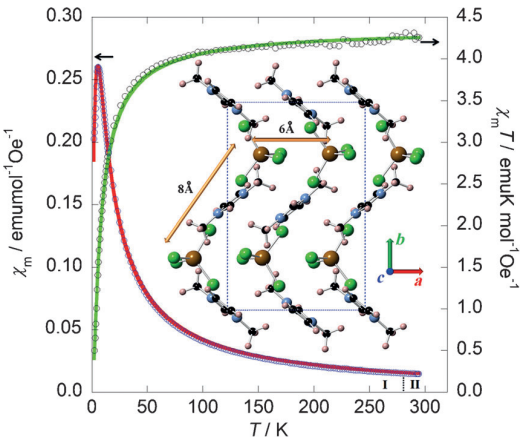

Figure 1. Temperature dependence of χ_m (blue circles) and $\chi_m T$ (black circles) for Dimim[$FeCl_4$] measured under 1 kOe. The solid red and green lines are the fit according to Equation (2) in the Supporting Information. The inset shows the crystal structure view along the [001] direction of phase **I** at 9 K. Brown (iron), green (chloride), black (carbon), blue (nitrogen) and light pink (hydrogen). The dotted square represents the unit cell.

Figure S6 in the Supporting Information). This tetrahedrally coordinated anion is fairly regular (mean values of Cl-Fe-Cl bond angles are 109(2)° for **I** and 110(3)° for **II**) with slightly different bond lengths for phase **I** and **II** (respective mean values 2.16(2) and 2.19(3) Å). The Dimim cations lie antiparallel to each other along the b direction, and are stacked nearly identically one above the other in the a and c directions, although slightly distorted in **I**. The dihedral angles of the methyl groups to the imidazolium ring [∢(C-*N*-C-N)] in both phases range from 177 to 179°. The refined values for the C–C and C–N bond lengths lie in the expected range and are comparable to those found in other imidazolium compounds, for example, in Bmim$_2$[XCl_4] (Bmim = 1-butyl-3-methylimidazoliumX = Fe, Ni and Co)[17] and Emim[$FeCl_4$].[16a]

The topologies of the unit cell in both phases are quite similar, showing virtually the same cation–anion arrangement as well as the cation and anion orientation. Each $[FeCl_4]^-$ tetrahedron is stacked with six Cl–Cl contacts (< 3.9 Å); two in a one-dimensional zigzag manner along the b axis (with slightly longer distances, 3.87(3) Å) and four in two linear chains propagated along the bisectors of the ac plane (3.63(4) (2×), 3.81(4) Å (2×)). No π–d interactions of the aromatic rings with the $[FeCl_4]^-$ metal complexes are observed in either phase, because the distances between them (near 4 Å) are considerably larger than the sum of the van der Waals (vdw) radii of C(H) and Cl atoms (3.57 Å).[18] The Dimim cation displays six and twelve weak (long) hydrogen bonds[19] for phases **II** and **I**, respectively, according to the IUPAC rule[20] (Figure S7 and Table S5 in the Supporting Information). It should be mentioned that the typical most acidic hydrogen atom of the imidazolium ring, C2–H position,[21] is not involved in the hydrogen bond network of phase **II** (nomenclature depicted in Figure S7 in the Supporting Information). Although this issue differs from the data reported for the Emim$_2$[MCl_4] (M = Co, Ni and Fe)[17] and DimimCl (Dimim = 1,3-dimethylimidazolium) ionic liquids,[22] in which the strongest hydrogen bond was located in this position; similar behaviour was observed in the Emim[BF_4][23] and Emim[$FeCl_4$][16a] MILs. In phase **I**, significantly stronger (shorter) hydrogen bonds are found, which is consistent with the Raman spectra.[24] At 4 K, the Raman bands of the C–H stretching modes of the imidazolium ring, located between 3100 and 3200 cm^{-1}, increase in intensity, which is characteristic for strong hydrogen bonds at the C2 and C4/5 positions.[19] In addition, in the low-frequency range, a splitting of the Raman modes of the $[FeCl_4]^-$ complex, associated to the crystallographic phase transition, was detected (Figure S8 of the Supporting Information).

Measurements of magnetic susceptibility as a function of temperature show a sharp maximum at approximately 5.6 K (Figure 1), indicating the existence of a 3D antiferromagnetic ordering. This result indicates that a smaller chain length in the imidazolium cation [from Bmin$^+$ that shows no 3D ordering through Emim$^+$ (4 K) to Dimim$^+$ (5.6 K)] stabilizes the magnetic ordering. Above 10 K, a paramagnetic behaviour is displayed, with a $\chi_m T$ value of 4.25 emuK mol^{-1}Oe^{-1} (5.83 μ_B) at room temperature. At temperatures higher than 10 K, the magnetic susceptibility data follow the Curie–Weiss law with Weiss temperatures, θ_p, close to −7.0 K with a Curie constant of C = 4.34 emuK mol^{-1}Oe^{-1} [see Eq. (1) in Supporting Information]. This value corresponds to an effective paramagnetic moment (μ_{eff}) of 5.88 μ_B per Fe ion; this agrees with the expected value of 4.375 emuK mol^{-1}Oe^{-1} (5.92 μ_B) for an Fe^{3+} ion with a magnetic spin S = 5/2.[25] Due to the anisotropy of the crystal, a combination of a modified expression of the one-dimensional Bonner and Fisher model,[26] for the interplane interactions, and a two-dimensional Rushbrook and Wood model,[27] for the intraplane interactions, was used to extract the magnetic exchange couplings between the Fe^{3+} ions (see magnetic fitting calculations in the Supporting Information). The best fit leads to the parameters $J_\perp$ = −0.511 K for the interplane exchange interaction and $J_{||}$ = −0.359 K value for the intraplane interactions with g = 2.03. These small values point to a very weak antiferromagnetic interactions, in accordance with the large dis-

ChemPubSoc Europe

CHEMISTRY A European Journal Communication

tances between the iron-complex anions and the literature values for this type of magnetic pathway.[28]

Neutron powder diffraction experiments at temperatures lower than 10 K show that the $P2_12_12_1$ symmetry of phase **I** is maintained below the ordering temperature, with small shifts in the Bragg reflections associated with lattice contraction. Difference patterns resulting from subtracting the nuclear contribution (pattern at 9 K) from the nuclear and magnetic ones, reveal, below 6 K, a sharp Bragg peak superimposed on a very broad diffuse background (see Figure S11 of the Supporting Information). This additional elastic intensity at low temperature confirms the onset of a magnetic ordering ($T_N = 5.5$ K). If we consider that the magnetic moment of Fe^{+3} ($S = 5/2$) is partially delocalized in the chloride ion (see below), the intensities of the magnetic peaks obtained should be very weak, but sufficient to allow 3D antiferromagnetic ordering to be observed. The presence of diffuse scattering could be the signature of additional short-range magnetic ordering superposed to the 3D ordering, which increases in a monotonous way below T_N, as observed in other geometrically frustrated antiferromagnetic materials.[29]

Below 5 K the magnetic interactions became cooperative despite the very long (6–8.5 Å) superexchange pathway. For that reason knowledge of the spin-density distribution is of crucial importance to the understanding the magnetic interaction mechanism in Dimim[$FeCl_4$]. From the atomic structure the most likely exchange pathways should be of the Fe-Cl-Cl-Fe type (Figure 2). The electron-transfer transitions due to a partial covalent bonding produce a spin delocalization[30] that would strengthen the interactions between magnetic orbitals localized in different tetrachloride ferrate units.[31] In order to substantiate this claim, density functional theory (DFT) calculations were carried out within the new formalism to deal with van der Waals interactions,[11c,32] which have been successfully applied to the study of ILs.[33] Different magnetic configurations have been tried, with the G-type antiferromagnetic phase being the most stable one (see detail of DFT analysis in the Supporting Information). Figure 2 also shows the spin density of the interplane exchange magnetic interaction for the most stable phase on the *ab* plane, which contains two Fe and two Cl atoms. The different sign in the spin density in neighbouring $[FeCl_4]^-$ tetrahedron along the *b* axis is an indication of the antiferromagnetic configuration. As can be seen, the spin density is not strictly localized on the iron ions, but is partially delocalized onto the first chloride neighbours. The sum of the Mulliken populations of the iron and the four neighbouring chloride atoms is equal to 4.98(1) μ_B. This agrees with the expected spin distribution of Fe^{3+} ion with a magnetic spin $S = 5/2$ (5 μ_B). The quantity of spin transferred from the Fe^{3+} ion toward its neighbours ranges from 0.27 to 0.25 μ_B (The sum of the spin transferred per Fe^{3+} is 1.06 μ_B; 21% of the expected saturation value of 5 μ_B.) Similar results are obtained by integrating the spin-polarized charge density in non-overlapping spheres centred on the different atoms. These reflect a stronger covalence of the Fe–Cl bond compared to other metal–Cl bonds (M = Ni, Cu and Co),[34] but they are in good agreement with those detected in other Fe^{+3} compounds (for $K_2FeCl_5{\cdot}H_2O$ and $Rb_2FeBr_5{\cdot}H_2O$, 17 and 21% spin delocalization, respectively).[28b]

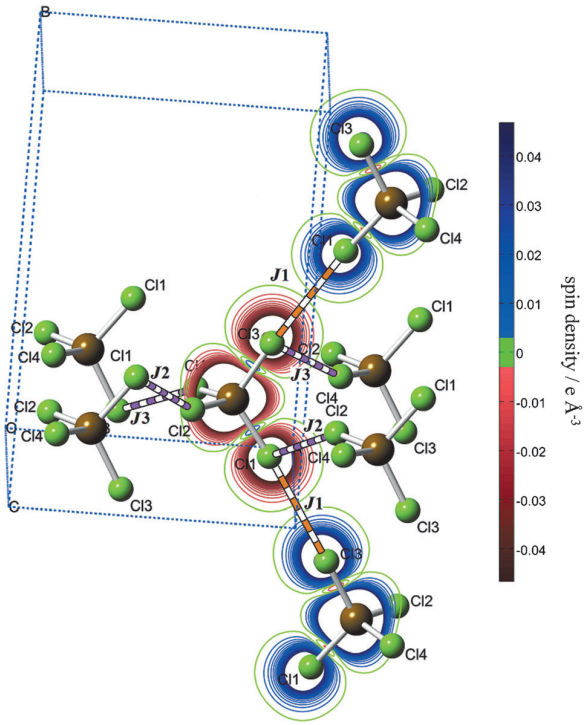

Figure 2. Schematic view of the possible exchange pathways for Dimim-[$FeCl_4$], through Fe-Cl-Cl-Fe bridges, are shown. The picture also displays the projection of the induced spin density onto the Fe_2L_2 plane ($z/c = 0.26$) for the interplane exchange magnetic interaction at 0 K. The levels are (0.05 e Å^3 with steps of 0.005 e Å^3). Only the low-density levels are drawn.

DFT calculations have also been successfully applied to the estimation of the exchange coupling constants, *J*, for a variety of transition-metal complexes.[35] From the difference in energy between the magnetic configurations, the value of the exchange magnetic couplings was inferred, arriving at the same qualitative results as before: weak antiferromagnetic coupling and stronger interaction between planes.

The analysis of the magnetostructural correlations in Dimim-[$FeCl_4$] will contribute to elucidating one important open question: the reason why interplane magnetic interactions are stronger than intraplane ones. Although the Cl–Cl distances obtained are slightly longer than the sum of the van der Waals radii of two Cl atoms (3.60 Å), the data show a remarkable agreement with the contact distances reported in other metal–organic materials[18] that show this type of magnetic coupling. In the crystal structure of **I**, all the $[FeCl_4]^-$ metal complexes are stacked upon one another in a three-dimensional manner with several Cl–Cl contacts (see Figure 2, and Figure S12 and Table S10 of Supporting Information). In this sense, it is possible to define a *J* interplane coupling ($J_\perp$ or J_1), which gives rise to zig-zag chains propagating along the *b* direction with two Fe-Cl-Cl-Fe connections, the angles of which range from 173.2 to 174.7°. This magnetic coupling leads to antiferromagnetic interactions. In addition to J_1, there are two intraplane interac-

ChemPubSoc Europe

CHEMISTRY A European Journal Communication

tions $J_{\parallel}$ (J_2 and J_3), which connect the iron atoms in zig-zag chains in the *ac* plane, with similar Fe—Fe distances. For these intraplane interactions, the antiferromagnetic couplings observed imply an unusual combination of exchange angles: 1) Fe-Cl-Cl, which varies between 87.0 and 93.3° and 2) Cl-Cl-Fe, which ranges from 154.4 to 158.2°. If one assumes that the magnetic exchange through the double halide bridges depends on both 1) the degree of delocalization of spin density from the metal ion to the halide, and 2) the orbital overlap between the two non-bonding halide ions,[36] $J_{\perp}$ should have a higher value (antiferromagnetic coupling near to 180° in both angles) than $J_{\parallel}$. These results confirm those obtained by the magnetic susceptibility fitting and DFT calculations.

In summary, a novel magnetic ionic liquid (MIL) with 3D antiferromagnetic ordering has been synthetized and characterized. The information obtained from magnetic characterization was supplemented by analysis of DFT calculations and the magnetostructural correlations. The result gives no evidence for direct iron-iron interactions, corroborating that the 3D magnetic ordering in MILs takes place through superexchange coupling via two diamagnetic intermediaries. The DFT calculations reflect the fact that the spin density of the iron ions is spread over the chloride atoms, showing a higher superexchange magnetic interaction between the planes.

Experimental Section

Details of the synthesis and characterisation of the MIL can be found in the Supporting Information. CCDC-973942 (phase **I**) and 973943 (phase **II**) contain the supplementary crystallographic data for this paper. These data can be obtained free of charge from The Cambridge Crystallographic Data Centre via www.ccdc.cam.ac.uk/data_request/cif.

Acknowledgements

Financial support from the Spanish Ministerio de Ciencia e Innovación (Project MAT2011-27573-C04) is acknowledged. This work has been carried out within the framework of the MALTA Consolider Ingenio 2010 (Ref. CSD2007-00045). The authors thankfully acknowledge the computer resources, technical expertise and assistance provided by the Red Española de Supercomputación. We also acknowledge Jorge Kohanoff and Pablo Garcia for their guidance and support with regard to the theoretical calculations and Becas Iberoaméricas Jóvenes Profesores Investigadores 2011, Santander Universidades.

Keywords: density functional calculations · ionic liquids · magnetic properties · structure elucidation

[1] E. Coronado, G. Minguez Espallargas, *Chem. Soc. Rev.* **2013**, *42*, 1525 – 1539.
[2] T. Torimoto, T. Tsuda, K.-i. Okazaki, S. Kuwabata, *Adv. Mater.* **2010**, *22*, 1196 – 1221.
[3] R. E. Del Sesto, T. M. McCleskey, A. K. Burrell, G. A. Baker, J. D. Thompson, B. L. Scott, J. S. Wilkes, P. Williams, *Chem. Commun.* **2008**, *0*, 447 – 449.
[4] T. Peppel, M. Köckerling, M. Geppert-Rybczyńska, R. V. Ralys, J. K. Lehmann, S. P. Verevkin, A. Heintz, *Angew. Chem.* **2010**, *122*, 7270 – 7274; *Angew. Chem. Int. Ed.* **2010**, *49*, 7116 – 7119.
[5] B. Mallick, B. Balke, C. Felser, A.-V. Mudring, *Angew. Chem.* **2008**, *120*, 7747 – 7750; *Angew. Chem. Int. Ed.* **2008**, *47*, 7635 – 7638.
[6] K. Tanaka, F. Ishiguro, Y. Chujo, *J. Am. Chem. Soc.* **2010**, *132*, 17649 – 17651.
[7] C.-X. Miao, J.-Q. Wang, B. Yu, W.-G. Cheng, J. Sun, S. Chanfreau, L.-N. He, S.-J. Zhang, *Chem. Commun.* **2011**, *47*, 2697 – 2699.
[8] P. Brown, C. P. Butts, J. Eastoe, E. Padron Hernandez, F. L. d. A. Machado, R. J. de Oliveira, *Chem. Commun.* **2013**, *49*, 2765 – 2767.
[9] Y. Funasako, T. Mochida, T. Inagaki, T. Sakurai, H. Ohta, K. Furukawa, T. Nakamura, *Chem. Commun.* **2011**, *47*, 4475 – 4477.
[10] P. Brown, A. Bushmelev, C. P. Butts, J. Cheng, J. Eastoe, I. Grillo, R. K. Heenan, A. M. Schmidt, *Angew. Chem.* **2012**, *124*, 2464 – 2466; *Angew. Chem. Int. Ed.* **2012**, *51*, 2414 – 2416.
[11] a) K. Binnemans, *Chem. Rev.* **2007**, *107*, 2592 – 2614; b) I. J. B. Lin, C. S. Vasam, *J. Organomet. Chem.* **2005**, *690*, 3498 – 3512; c) J. Dupont, *Acc. Chem. Res.* **2011**, *44*, 1223 – 1231.
[12] a) H. Weingärtner, *Angew. Chem.* **2008**, *120*, 664 – 682; *Angew. Chem. Int. Ed.* **2008**, *47*, 654 – 670; b) J. Dupont, *J. Braz. Chem. Soc.* **2004**, *15*, 341 – 350.
[13] H. Mehdi, K. Binnemans, K. Van Hecke, L. Van Meervelt, P. Nockemann, *Chem. Commun.* **2010**, *46*, 234 – 236.
[14] a) Y. Yoshida, G. Saito, *J. Mater. Chem.* **2006**, *16*, 1254 – 1262; b) I. de Pedro, D. P. Rojas, J. Albo, P. Luis, A. Irabien, J. A. Blanco, J. Rodriguez Fernandez, *J. Phys. Condens. Matter* **2010**, *22*, 296006; c) I. de Pedro, D. P. Rojas, J. A. Blanco, J. Rodriguez Fernandez, *J. Magn. Magn. Mater.* **2011**, *323*, 1254 – 1257.
[15] A. García-Saiz, I. de Pedro, J. A. Blanco, J. González, J. R. Fernández, *J. Phys. Chem. B* **2013**, *117*, 3198 – 3206.
[16] a) T. Bäcker, O. Breunig, M. Valldor, K. Merz, V. Vasylyeva, A.-V. Mudring, *Cryst. Growth Des.* **2011**, *11*, 2564 – 2571; b) A. Mudring, *Aust. J. Chem.* **2010**, *63*, 544 – 564.
[17] C. Zhong, T. Sasaki, A. Jimbo-Kobayashi, E. Fujiwara, A. Kobayashi, M. Tada, Y. Iwasawa, *Bull. Chem. Soc. Jpn.* **2007**, *80*, 2365 – 2374.
[18] R. S. Rowland, R. Taylor, *J. Phys. Chem.* **1996**, *100*, 7384 – 7391.
[19] a) C. Roth, T. Peppel, K. Fumino, M. Kockerling, R. Ludwig, *Angew. Chem.* **2010**, *122*, 10419 – 10423; *Angew. Chem. Int. Ed.* **2010**, *49*, 10221 – 10224; b) A. Wulf, K. Fumino, R. Ludwig, *Angew. Chem.* **2010**, *122*, 459 – 463; *Angew. Chem. Int. Ed.* **2010**, *49*, 449 – 453.
[20] E. Arunan, G. R. Desiraju, R. A. Klein, J. Sadlej, S. Scheiner, I. Alkorta, D. C. Clary, R. H. Crabtree, J. J. Dannenberg, P. Hobza, H. G. Kjaergaard, A. C. Legon, B. Mennucci, D. J. Nesbitt, *Pure Appl. Chem.* **2011**, *83*, 1637 – 1641.
[21] K. Fumino, A. Wulf, R. Ludwig, *Angew. Chem.* **2008**, *120*, 8859 – 8862; *Angew. Chem. Int. Ed.* **2008**, *47*, 8731 – 8734.
[22] I. Skarmoutsos, D. Dellis, R. P. Matthews, T. Welton, P. A. Hunt, *J. Phys. Chem. B* **2012**, *116*, 4921 – 4933.
[23] K. Matsumoto, R. Hagiwara, Z. Mazej, P. Benkič, B. Žemva, *Solid State Sci.* **2006**, *8*, 1250 – 1257.
[24] a) K. Fumino, T. Peppel, M. Geppert-Rybczynska, D. H. Zaitsau, J. K. Lehmann, S. P. Verevkin, M. Kockerling, R. Ludwig, *Phys. Chem. Chem. Phys.* **2011**, *13*, 14064 – 14075; b) T. Peppel, C. Roth, K. Fumino, D. Paschek, M. Kockerling, R. Ludwig, *Angew. Chem.* **2011**, *123*, 6791 – 6795; *Angew. Chem. Int. Ed.* **2011**, *50*, 6661 – 6665.
[25] I. de Pedro, A. Garcia Saiz, J. A. Gonzalez, I. Ruiz de Larramendi, T. Rojo, C. Afonso, S. Simeonov, J. C. Waerenborgh, J. A. Blanco, J. Rogriguez, *Phys. Chem. Chem. Phys.* **2013**, *15*, 12724 – 12733.
[26] J. C. Bonner, M. E. Fisher, *Phys. Rev.* **1964**, *135*, A640 – A658.
[27] G. S. Rushbrooke, P. J. Wood, *Mol. Phys.* **1958**, *1*, 257 – 283.
[28] a) J. A. Zora, K. R. Seddon, P. B. Hitchcock, C. B. Lowe, D. P. Shum, R. L. Carlin, *Inorg. Chem.* **1990**, *29*, 3302 – 3308; b) J. Campo, J. Luzón, F. Palacio, G. J. McIntyre, A. Millán, A. R. Wildes, *Phys. Rev. B* **2008**, *78*, 054415.
[29] a) O. A. Petrenko, C. Ritter, M. Yethiraj, D. McK Paul, *Phys. Rev. Lett.* **1998**, *80*, 4570 – 4573; b) J. E. Greedan, C. R. Wiebe, A. S. Wills, J. R. Stewart, *Phys. Rev. B* **2002**, *65*, 184424.
[30] A. Zheludev, A. Grand, E. Ressouche, J. Schweizer, B. G. Morin, A. J. Epstein, D. A. Dixon, J. S. Miller, *Angew. Chem.* **1994**, *106*, 1454 – 1457; *Angew. Chem. Int. Ed. Engl.* **1994**, *33*, 1397 – 1399.
[31] B. N. Figgis, P. A. Reynolds, R. Mason, *Inorg. Chem.* **1984**, *23*, 1149 – 1153.

ChemPubSoc Europe

CHEMISTRY
A European Journal
Communication

[32] G. Román-Pérez, J. M. Soler, *Phys. Rev. Lett.* **2009**, *103*, 096102.
[33] J. Kohanoff, C. Pinilla, T. G. Youngs, E. Artacho, J. M. Soler, *J. Chem. Phys.* **2011**, *135*, 154505.
[34] a) C.-R. Lee, C.-C. Wang, K.-C. Chen, G.-H. Lee, Y. Wang, *J. Phys. Chem. A* **1999**, *103*, 156 – 165; b) B. N. Figgis, L. Khor, E. S. Kucharski, P. A. Reynolds, *Acta Crystallogr. Sect. B* **1992**, *48*, 144 – 151.
[35] R. Caballol, O. Castell, F. Illas, I. de P. R. Moreira, J. P. Malrieu, *J. Phys. Chem. A* **1997**, *101*, 7860 – 7866.
[36] M. M. Turnbull, C. P. Landee, B. M. Wells, *Coord. Chem. Rev.* **2005**, *249*, 2567 – 2576.

Received: September 11, 2013
Published online on December 10, 2013

CHEMISTRY
A EUROPEAN JOURNAL

Supporting Information

A Magnetic Ionic Liquid Based on Tetrachloroferrate Exhibits Three-Dimensional Magnetic Ordering: A Combined Experimental and Theoretical Study of the Magnetic Interaction Mechanism

Abel García-Saiz,[a] Pedro Migowski,[b] Oriol Vallcorba,[c] Javier Junquera,[a] Jesús Angel Blanco,[d] Jesús Antonio González,[a] María Teresa Fernández-Díaz,[e] Jordi Rius,[c] Jairton Dupont,[b] Jesús Rodríguez Fernández,[a] and Imanol de Pedro*[a]

chem_201303602_sm_miscellaneous_information.pdf

Supplementary Material

Synthesis

10 g of the 1,3-dimethylimidazolium iodide were dissolved in 100 mL of distilled water and passed through an Amberlite IRA-400 column (OH- form) chloride free (Volhard test). The resulting basic aqueous solution was neutralized with concentrated hydrochloric acid until the pH was 7 and the water removed in a rotary evaporator. The remaining water was removed by heating the resulting oil at 100ºC under vacuum. The resulting material was then dissolved in dichloromethane and dried over anhydrous Na_2CO_3, filtered and the solvent removed under vacuum, affording 9.1 g of (91%) of 1,3-dimethylimidazolium chloride. Inside the glove-box 2 g of 1,3-dimethylimidazolium chloride (15 mmol) was mixed with 1.61 g of anhydrous $FeCl_3$ (15 mmol) in a 8 mL vial. The resulting mixture rapidly melted due to the highly exothermic reaction. The final product, 3.61 g (100% yield), was obtained as a brown-reddish solid.

Elemental Analysis and Thermal Investigations

Chemical analysis: Microanalytical data (C, H and N) were obtained with an Elemental model Vario 51 MACRO elemental analyser. The iron and chlorine contents were determined with a Spectra Spectrometer DCP-AEC after dissolving a weight amount of sample in water (aq).
Elemental analysis for $C_5N_2H_9Cl_4Fe$. Calcd: C, 20.37; N, 9.50; H, 3.08; Cl, 48.10; Fe, 18.95%. found: C, 20.24; N, 9.45; H, 3.05; Cl, 48.26; Fe, 19.0%.
Thermal analysis: A Mettler-Toledo (TGA/SDTA851 and DSC822) was used for the thermal analyses in an oxygen dynamic atmosphere (50 mL/min) at a heating rate of 10 °C/min. In all cases, *ca*. 15 mg of powder sample was thermally treated, and blank runs were performed. Heat capacity measurements were carried out by a two-tao relaxation method using a standard QD PPMS magnetometer. The sample was a plate of 0.3 mm thickness and ≈7 mg weight obtained by compressing the original polycrystalline powder. Data were collected with zero field from 2 to 300 K.

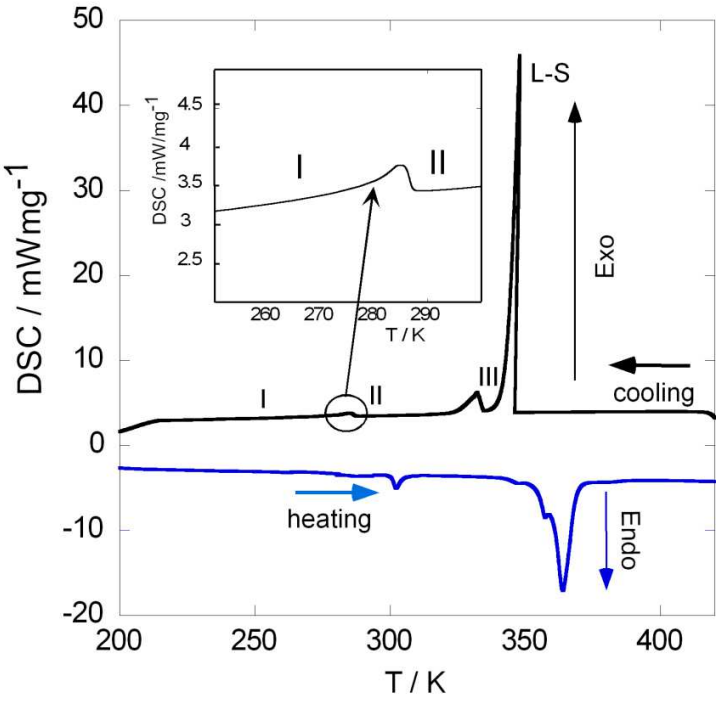

Figure S1. DSC-thermogram of Dimin[$FeCl_4$]. Black line: 1st cooling cycle; blue line: 2nd heating cycle. Heating rate 10 K/min. The inset shows an enlargement of room temperature region of 1st cooling cycle.

Table S.1. Transition temperatures and enthalpies for Dimin[$FeCl_4$]

	First cooling			Second heating			
	T/ K	ΔH/ kJmol^{-1}	ΔS/ Jmol^{-1}K^{-1}	T/K	ΔH/ kJmol^{-1}	ΔS/ Jmol^{-1}K^{-1}	ΔS_f/ Jmol^{-1}K^{-1}
Phase I-II	285	-4.3	-15.35	303	9.2	33.7	
Phase II-III	332	-21.8	-65.90	357	28.8	81.8	
mp Phase III				364			424.5

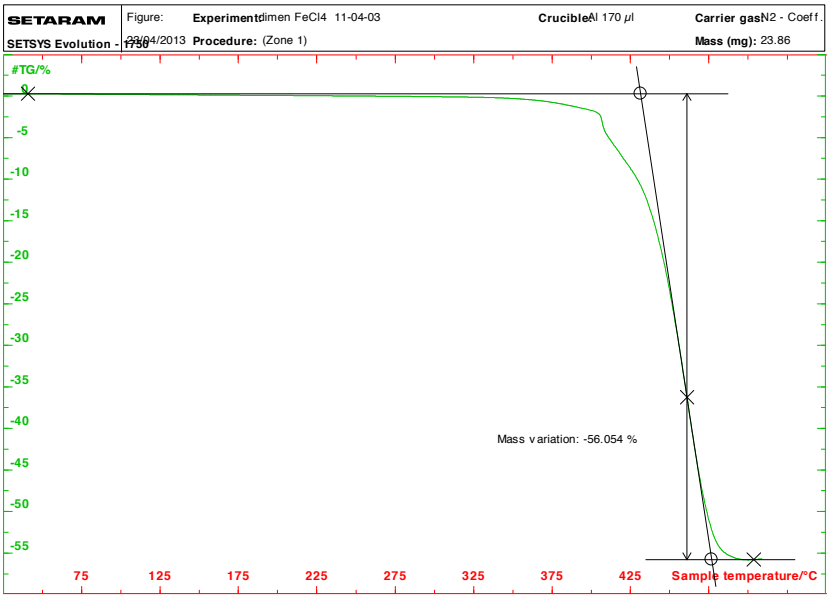

Figure S.2. TGA curve recorded in the inert atmosphere.

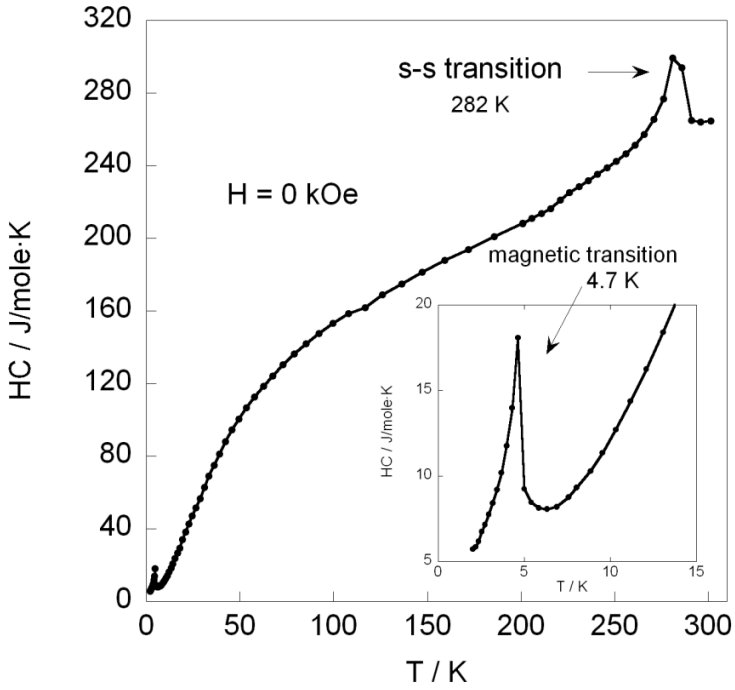

Figure S.3. Experimental specific heat data (Cp) of Dimin[$FeCl_4$] between 2 and 300 K. The inset shows an enlargement of low temperature region where a lambda anomaly associated with a three-dimensional long range magnetic ordering is observed.

Structural characterization: High and low resolution neutron diffraction experiments and Raman spectroscopy

Neutron Powder diffraction: Neutron powder diffraction measurements were performed on the D1B and D2B instruments at the Institute Laue-Langevin (ILL) of Grenoble, using a wavelength of 2.520 and 1.594 Å, respectively. About 3 g of polycrystalline Dimin[$FeCl_4$], packed in a cylindrical vanadium container and held in a liquid helium cryostat, was employed in the experiments. The high resolution of the D2B instrument was used to obtain structural data at room temperature over a large angular range, $10 < 2\theta < 150^{o}$. The crystal structures of phase I and II of Dimin[$FeCl_4$] were solved by the direct-space methodology implemented in TALP[1] using intensities extracted with DAJUST[2] and introducing a similar reported structure[3] as starting model. The final restrained Rietveld refinement were performed with the computer program RIBOLS18[4] by applying the restraints taken from respective DFT calculations.

Raman spectroscopy: The Raman spectra were taken at room temperature under atmospheric pressure in backscattering geometry with a Horiba T64000 triple spectrometer using the 514.5 nm line of a Coherent Innova Spectrum 70C Ar^{+}-Kr^{+} laser and a nitrogen-cooled CCD (Jobin-Yvon *Symphony*) with a confocal microscope and a 100x objective for detection. The integration time was 40 s and the power was kept below 40 mW to avoid laser-heating effects on the tested material and the concomitant softening of the observed Raman peaks. The low temperature measurements were performed in a horizontal microscopy cryostat (MicrostatHe2) from Oxford Instruments and the temperature was measured with a precision of ± 1 K at low temperatures and for the Raman detection we used a 20x objective in the confocal microscope.

Table S2. Crystallographic data and structure refinement details at 300K (D2B) and 9K (D1B) for DiminFeCl_4.

	Phase II (D2B)	**Phase I (D1B)**
Molecular formula	$C_5H_9N_2$, Cl_4Fe	$C_5H_9N_2$, Cl_4Fe
Formula weight	294.8	294.8
Crystal System	Monoclinic	Orthorhombic
Space group	$P2_1$	$P2_12_12_1$
a (Å)	6.5419(27)	9.0915(13)
b (Å)	14.0374(26)	13.7309(16)
c (Å)	6.5357(30)	8.9738(12)
α (º)	90	90
β(º)	90.006(23)	90
γ(º)	90	90
Volume ($Å^3$)	600.2(4)	1120.2(3)
Z	2	4
Calculated density (g/cm^3)	1.631	1.748
Measurement Temperature (K)	300K	9K
Radiation (wavelengths in Å)	1.594	2.520
F(000)	132	265
Measured 2ϑ range, stepsize (º)	8.05–159.90, 0.05	8.09–128.09, 0.1
Rietveld refinement details:		
Profile function	Gaussian	Gaussian
2ϑ range used	8.05–80.00	15.2-90.1
Num. of reflections	355	139
Data points	1440	750
Parameters	72	72
Restraints	63	63
R_{wp}	0.0079	0.0124
R_{exp}[a]	0.0104	0.0245
$\chi_{Rietveld}/\chi_{Pattern\text{-}Matching}$	1.407	1.435

(a) The strong background in the neutron diffraction pattern (due mainly to the Hydrogen atoms in the compound) led to an anomalously high R_{exp}.

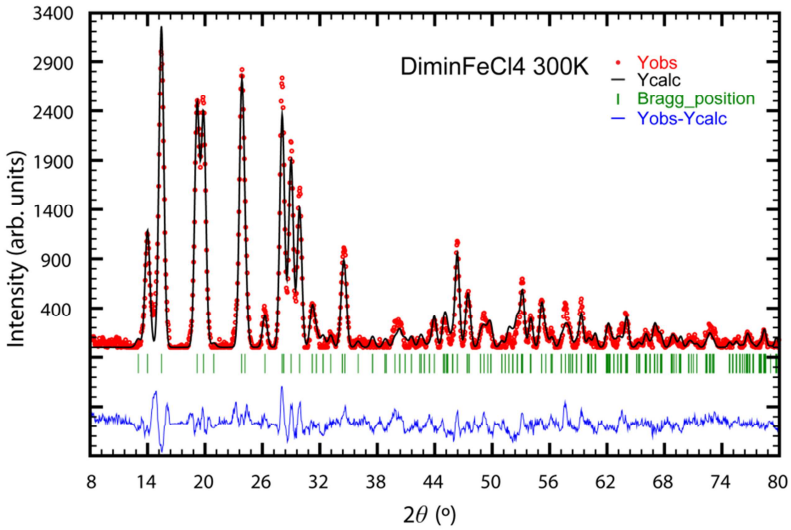

Figure S4. Rietveld refinement for DiminFeCl_4 at 300K (phase **II**): Observed (points), calculated (line) and difference profile (bottom).

Table S3. Atomic coordinates of phase **II** at 300 K referring to unit cell a = 6.5419(27) Å, b = 14.0374(26) Å, c = 6.5357(30) Å, $\alpha = \gamma = 90°$, β = 90.006(23) °. Space group $P2_1$.

Atom	*x/a*	*x/b*	*x/c*
N1	0.4209(32)	0.6507(15)	0.0900(35)
C2	0.3990(31)	0.6055(16)	-0.0836(35)
H2	0.2699(35)	0.6096(19)	-0.1794(43)
N3	0.5629(34)	0.5551(15)	-0.1278(34)
C4	0.6911(31)	0.5672(16)	0.0243(36)
H4	0.8345(33)	0.5344(16)	0.0413(46)
C5	0.6025(33)	0.6259(16)	0.1617(34)
H5	0.6734(42)	0.6487(18)	0.2964(34)
C1'	0.2770(38)	0.7108(16)	0.1800(42)
H1A'	0.1307(37)	0.6884(42)	0.1302(98)
H1B'	0.3039(91)	0.7824(16)	0.1314(99)
H1C'	0.2825(93)	0.7016(46)	0.3422(42)
C1"	0.5768(44)	0.4978(16)	-0.3023(35)
H1A"	0.4324(71)	0.4987(35)	-0.3794(50)
H1B"	0.6895(57)	0.5215(36)	-0.4058(67)
H1C"	0.5936(98)	0.4241(16)	-0.2621(52)
Fe	0.2240(24)	0.3624(23)	0.2581(24)
Cl1	0.5520(25)	0.3620(29)	0.2987(36)
Cl2	0.1397(46)	0.3776(31)	-0.0635(28)
Cl3	0.0774(47)	0.2310(27)	0.3821(51)
Cl4	0.0889(55)	0.4864(29)	0.4112(50)

Full occupancies for all atoms and $B_{overall}$ = 5.4(9)$Å^2$.

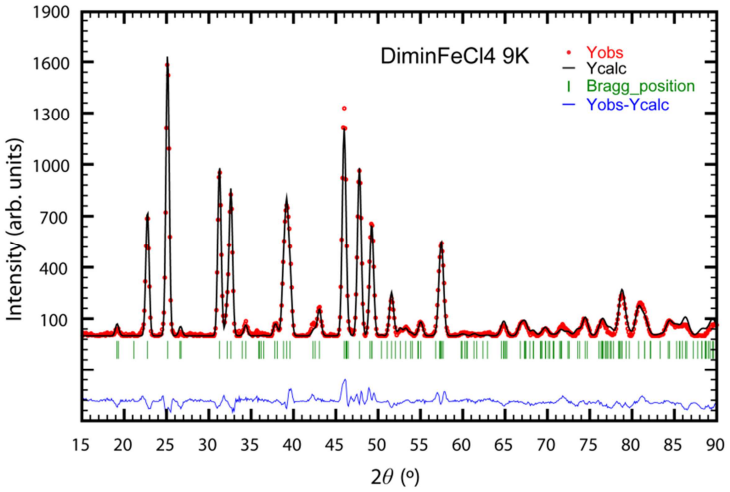

Figure S5. Rietveld refinement for DiminFeCl_4 at 9K (phase **I**): Observed (points), calculated (line) and difference profile (bottom).

Table S4. Atomic coordinates of phase **I** at 9K referring to unit cell a = 9.0915(13) Å, b = 13.7309(16) Å, c = 8.9738(12) Å, $\alpha = \beta = \gamma = 90°$. Space group $P2_12_12_1$.

Atom	*x/a*	*x/b*	*x/c*
N1	-0.0677(17)	0.4636(9)	0.2371(17)
C2	0.0191(17)	0.5021(11)	0.3362(14)
H2	0.0165(26)	0.4867(15)	0.4514(14)
N3	0.1142(15)	0.5585(9)	0.2706(17)
C4	0.0873(16)	0.5563(10)	0.1235(16)
H4	0.1449(22)	0.5994(11)	0.0463(24)
C5	-0.0252(16)	0.4968(11)	0.1029(14)
H5	-0.0802(21)	0.4775(13)	0.0043(18)
C1'	-0.1805(16)	0.3964(10)	0.2662(27)
H1A'	-0.2772(22)	0.4205(27)	0.2140(59)
H1B'	-0.1488(39)	0.3270(14)	0.2231(63)
H1C'	-0.1996(46)	0.3907(33)	0.3831(29)
C1"	0.2220(17)	0.6140(11)	0.3434(26)
H1A"	0.3261(16)	0.5875(35)	0.3120(67)
H1B"	0.2112(53)	0.6877(13)	0.3073(68)
H1C"	0.2112(54)	0.6111(45)	0.4614(25)
Fe	0.2540(12)	0.2516(15)	0.2617(23)
Cl1	0.3969(23)	0.3773(16)	0.2379(42)
Cl2	0.1116(24)	0.2480(23)	0.0719(19)
Cl3	0.3747(25)	0.1150(16)	0.2788(35)
Cl4	0.1300(29)	0.2702(19)	0.4644(20)

Full occupancies for all atoms and $B_{overall}$= 2.9(3)Å^2 .

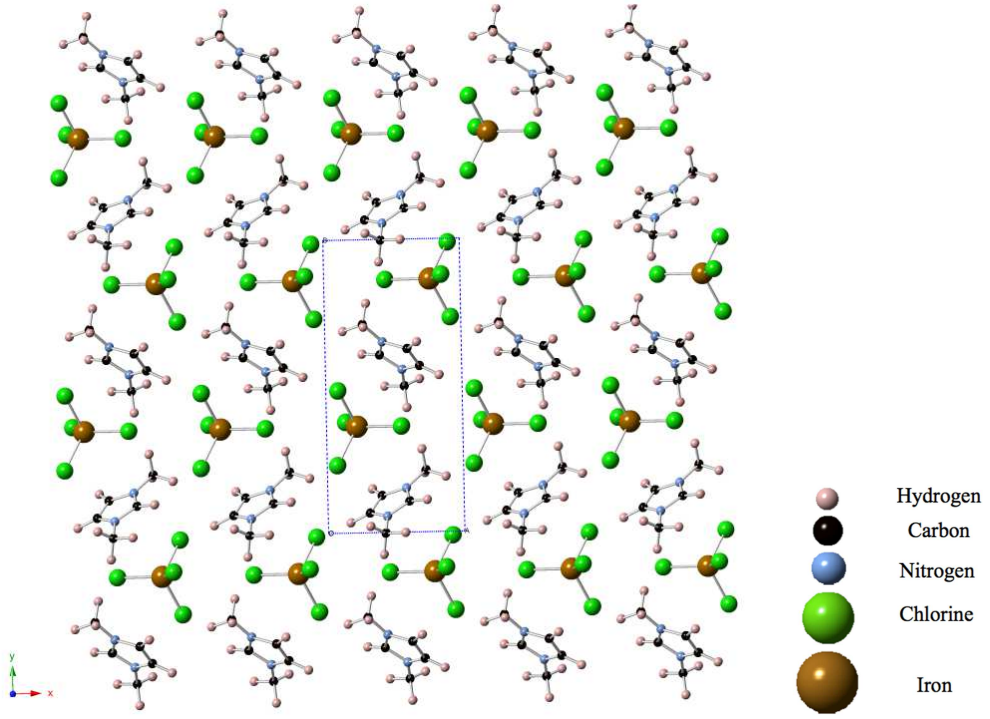

Figure S6. Crystal structure view along the |001| direction of phase **II** at 300 K.

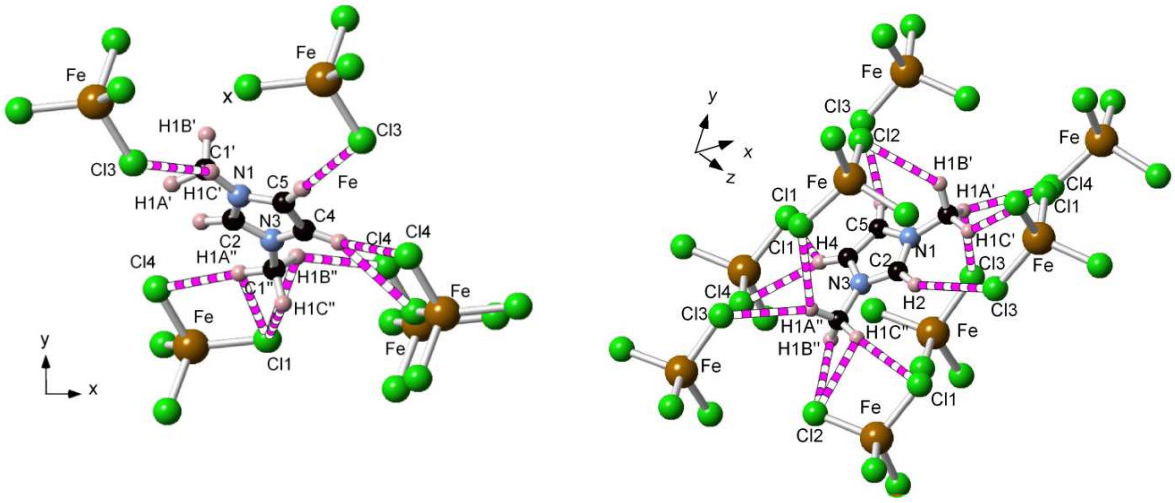

phase **II** phase **I**

Figure S7. Hydrogen-bonding network in phase **II** and **I** (H—Cl contact up to 3.1 Å are marked with pink and white stripes).

Table S5. Hydrogen-bonding in phase II and I.

Hydrogen Bond	Length (Å)	Angle (º)
Phase II		
C4-H4 – Cl2	3.05(4)	151(2)
C4-H4 --Cl4	3.01(4)	133(2)
C5-H5 -- Cl3	2.90(4)	169(2)
C1'-H1C' -- Cl3	2.99(6)	124(4)
*C1''-H1A'' -- Cl1	2.95(5)	95(3)
C1''-H1A'' -- Cl4	2.64(6)	174(4)
*C1''-H1B'' -- Cl1	3.09(6)	88(3)
C1''-H1B'' -- Cl4	2.92(5)	147(3)
*C1''-H1C'' -- Cl1	3.01(4)	92(3)
Phase I		
C2-H2 -- Cl3	3.08(3)	151(2)
C4-H4 – Cl4	2.82(3)	153(2)
C4-H4 – Cl1	2.81(4)	130(2)
C5-H5 -- Cl3	2.87(3)	158(2)
C1'-H1A' -- Cl1	3.03(3)	137(3)
C1'-H1A' -- Cl3	2.81(4)	124(3)
C1'-H1B' -- Cl2	2.94(5)	136(3)
C1'-H1C' -- Cl4	3.03(5)	126(3)
C1''-H1A'' -- Cl1	3.03(5)	125(3)
C1''-H1A'' -- Cl3	2.86(3)	152(3)
*C1''-H1B'' --Cl2	3.00(6)	89(3)
C1''-H1C'' -- Cl1	2.67(5)	163(4)
C1''-H1C'' -- Cl2	2.71(6)	106(3)

* Hydrogen bond plotted but not allowed according to IUPAC considerations.

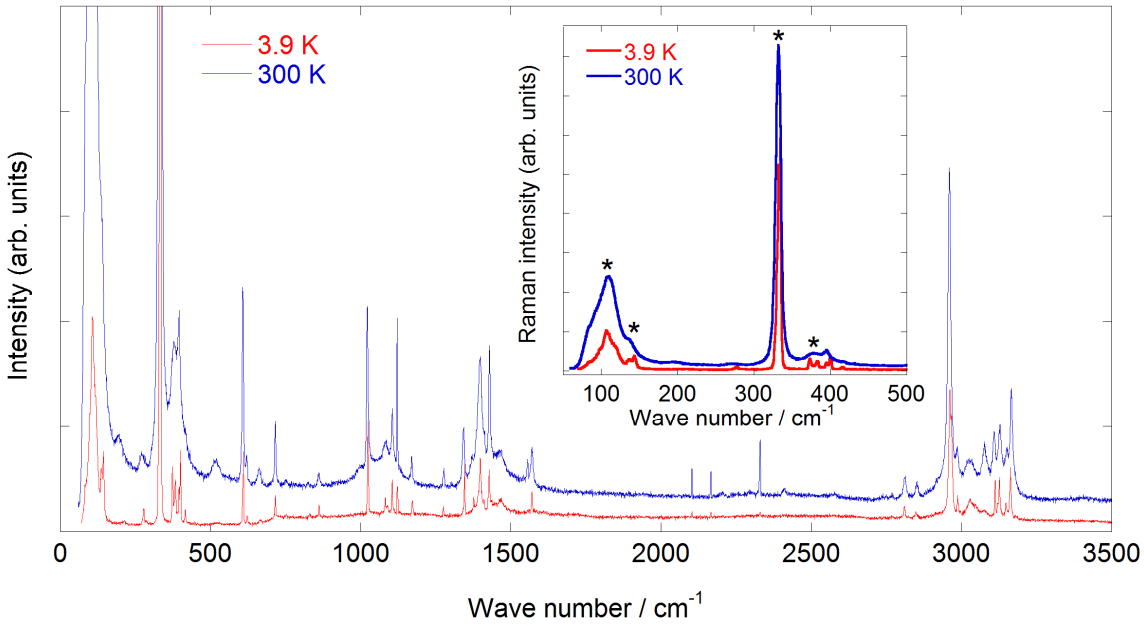

Figure S.8. Raman spectra of Dimin[$FeCl_4$] between 100 and 3500 cm^{-1} at 4 and 300 K. The inset shows an enlargement of the low wave number region where the $[FeCl_4]^-$ bands are marked with * symbol.

Table S.6. Vibrational assignment (cm^{-1}) of Dimin[$FeCl_4$] in the phase II (300 K) and phase I (4 K).

Assignment	**Phase II 300 K** Frequency/cm^{-1}	**Phase I 4 K** Frequency/ cm^{-1}
Fe-Cl Sym-Bend	110.9	107.3 118.5
Fe-Cl Asym-Bend	137.0	136.9 143.4
Fe-Cl Sym-Stretch	329.4	331.8 334.5
Fe-Cl Asym-Stretch	373.5	370.7 376.0
[Ring] op asym bend, N-CH_3 stretch	607.8	609.1
[Ring] op asym bend, N-CH_3 stretch	620.8	622.7
[Ring] op asym bend, N-CH_3 stretch	661.9	665.6
[Ring] ip asym bend, N-CH_3 stretch	715.9	716.0
[Ring] HC=CH asym bend	860.5	861.3
[Ring] ip sym stretch	993.1	993.2
[Ring] ip sym stretch	1022.2	1024.3
[Ring] ip sym stretch, [Ring] C=C stretch	1083.7	1089.0
[Ring] HC=CH sym bend, [Ring] N-CH_3 bend	1105.4	1104.8
[Ring] HC=CH sym bend, [Ring] ip sym stretch	1121.8	1122.3
[Ring] N-CH_3 bend	1169.7	1172.3
[Ring] ip asym stretch, [Ring] HC=CH sym stretch	1276.7	1275.2
[Ring] ip sym stretch, [Ring] N-CH_3 stretch	1343.0	1345.7
[Ring] ip sym stretch, [Ring] N-CH_3 stretch	1369.8	1376.6
[Ring] ip asym stretch, [CH_3] HCH bend	1398.0	1397.8
[Ring] ip asym stretch, HC=CH stretch,	1428.8	1427.9
[Ring] N-CH_3 stretch	1460.2	1467.0
[Ring] ip asym stretch, [Ring] N-CH_3 stretch	1570.2	1570.5
[CH_3] H-C-H sym stretch	2811.8	2810.4
[CH_3] H-C-H sym stretch	2851.8	2848.5
[CH_3] H-C-H sym stretch	2959.8	2961.4 2967.3
[CH_3] H-C-H asym stretch	2986.3	2988.0
[CH_3] H-C-H asym stretch	3027.5	3028.4
[CH_3] H-C-H asym stretch	3078.1	3076.7
[CH_3] H-C-H asym stretch	3108.7	3112.2
[Ring N-C(H)-N] C-H stretch	3128.4	3127.0
[Ring] HC=CH asym stretch	3150.3	3148.7
[Ring] HC=CH sym stretch, [Ring] ip sym stretch	3166.6	3163.7

Magnetic Properties

Magnetic measurements: Variable-temperature magnetic susceptibility measurements were performed using a standard QD PPMS magnetometer whilst heating from 2 to 300 K at 1 kOe after cooling in either the presence (field cooling, FC) or the absence (zero field cooling, ZFC) of the applied field. Magnetization as a function of field (*H*) was measured using the same magnetometer in the -85 ≤ *H*/*kOe* ≤ 85 range at 2 K after cooling the sample in zero field.

The field dependence on the magnetization at 2 K continuously increases without showing any tendency to saturation up to 85 kOe. The magnetization value obtained in this magnetic field (4.18 μB/Fe ion) is lower than that corresponding to the theoretical saturation (5 μB/Fe ion) indicating the existence of a strong magnetocrystalline anisotropy. In addition, the magnetization shows no hysteresis suggesting the absence of any ferromagnetic component down to 2K.

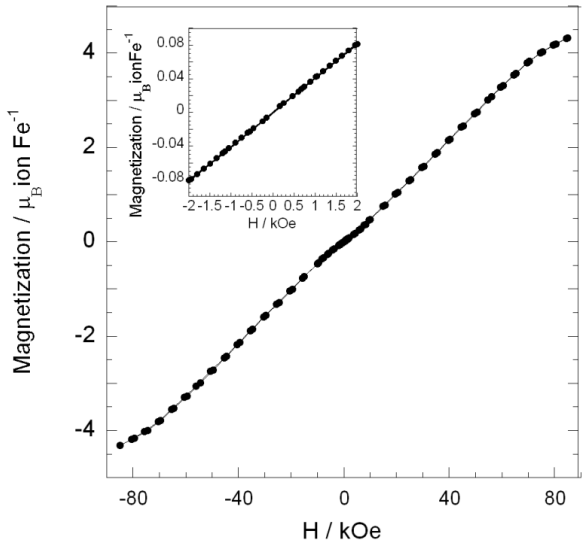

Figure S9. Magnetization versus applied magnetic field at 2 K for Dimin[$FeCl_4$]. The inset shows an enlargement of the low magnetic field region.

Magnetic Fit Calculations

The magnetic data were fitted in the paramagnetic range using the Curie-Weiss law for S= 5/2 in the molecular field approximation[4], Eq.(1), in order to clarify the significance of magnetic exchange between the Fe^{3+} ions in the crystal lattice

$$\chi_m = \frac{C}{T-\theta_P} = \frac{N\mu_0\mu_B^2 g^2 S(S+1)}{3k\left(T-\frac{zJS(S+1)}{3k}\right)} \qquad (1)$$

where N is Avogadro's number, g is the spectroscopic splitting factor, μ_B is the Bohr magneton, k is the Boltzmann constant, J is the exchange coupling parameter defined by $\mathcal{H}_{ex} = \sum_{nn} 2J\boldsymbol{S_i}\cdot\boldsymbol{S_j}$ and z is the number of nearest neighbour Fe^{3+} atoms. The least-squares fit of the experimental data from 20 to 300 K, with z = 4, gives a J value of -0.30 K. The Curie constant and Curie-Weiss temperature, C and θ_P, obtained by the fitting, have a value of 4.34 emuK/molOe and -7.0 K, respectively.

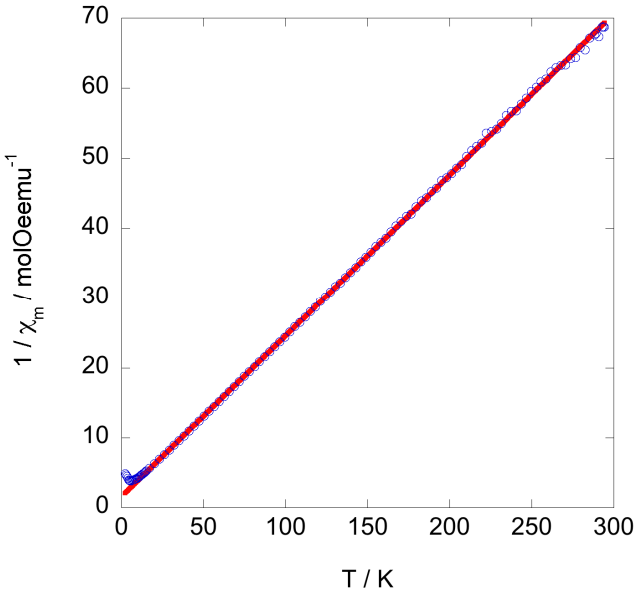

Figure S10. Inverse of the magnetic susceptibility versus the temperature. The red line is the fit according to Eq(1).

In order to determine the relation between the interplane and intraplane interaction, a combined expression of an antiferromagnetic linear chain and a 2D framework of spin 5/2 has been used to fit the whole range of temperature in the χ_m data, considering the total susceptibility as

$$\chi_m = \frac{1}{3}\chi_\perp + \frac{2}{3}\chi_\parallel \quad (2)$$

where the linear chain model for the interplane exchange interaction is a modified expression[5] of the Bonner and Fisher model[6] and the susceptibility is given by

$$\chi_\perp = \frac{NS(S+1)}{3kT}\mu_B^2 g^2 \frac{1+u(K)}{1-u(K)} \quad (3)$$

being

$$u(K) = \coth K - 1/K$$
$$K = -2JS(S+1)/kT$$

where J was defined as positive for antiferromagnetic coupling, considering $\mathcal{H}_{ex} = \sum_{nn} 2J\mathbf{S_i}\cdot\mathbf{S_j}$. In addition, the magnetic susceptibility for the 2D antiferromagnetic framework, $\chi_\parallel$ for S=5/2 is given by the Rushbrook and Wood expression[7]

$$\chi_\parallel = \left(\frac{N\mu_B^2 g^2 S(S+1)}{3kT}\right)\cdot(1 - 23.333x + 147.78x^2 - 405.48x^3 + 8171.3x^4 - 6461.8x^5 - 158110x^6)^{-1} \quad (4)$$

where $x = -J/kT$, with J positive value for antiferromagnetic coupling.

The least-squares fit of the experimental data from 2 to 300 K, with z = 4, gives a g=2.03, $J_\perp$=0.511 K value for the interplane exchange interaction and $J_\parallel$=0.329 K for the intraplane interaction, as indicated by the solid curve of χ_m and χ_mT in Figure 1.

Notice that the values of J in the manuscript have been included as negative numbers following the typical notation of antiferromagnetic exchange interaction.

Neutron Powder Diffraction

High flux and medium resolution of D1B at 2.525 Å were used to study the temperature evolution of the magnetic structure in the temperature range 2 – 9 K. The diffraction patterns were collected over 60 min every 0.5 K in the angular range $4 \leq 2\theta \leq 90$.

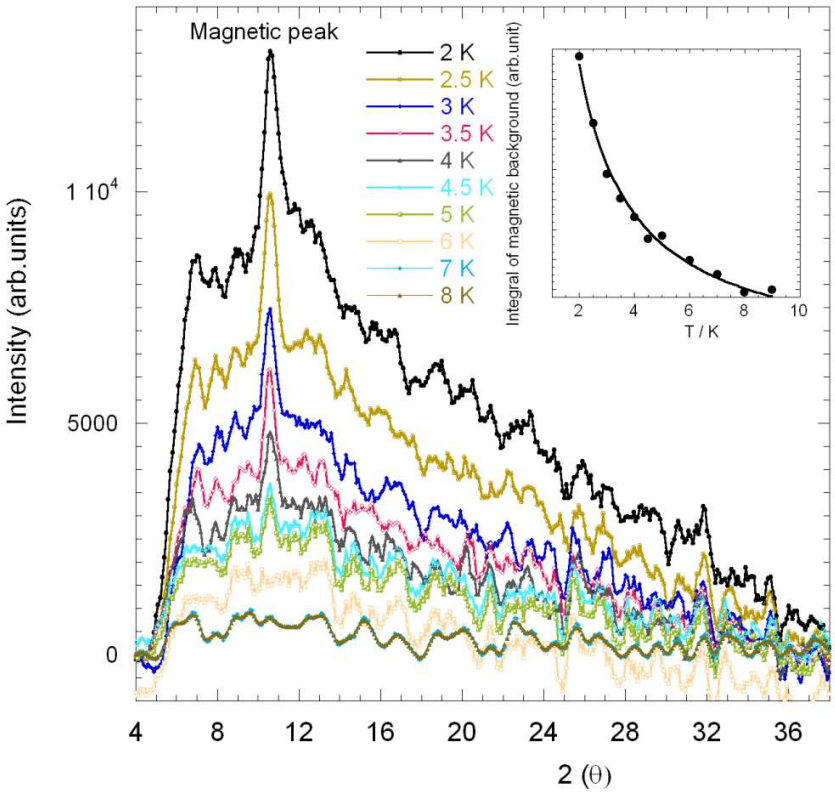

Figure S.11. Temperature dependence of the difference diagrams of D1B patterns between 2 and 8 K which have been obtained subtracting the nuclear contribution (pattern at 9 K) has been subtracted. The inset displays the evolution of the magnetic background integrated as a function of the temperature.

DFT calculations. Computational details.

We have carried out density functional first-principles simulations based on a numerical atomic orbital method as implemented in the SIESTA code[8]. All the calculations have been carried out within the efficient implementation[9] of the van der Waals (vdw) density functional of Dion et al.[10]. This fully non-local van der Waals correlation has been recently tested on imidazolium-based ionic liquids[11], showing spectacular improvements in the interatomic geometries, equilibrium volume and internal geometry with respect to the local density (LDA) and generalized gradient approximation (GGA) at a very modest computational cost.

Core electrons were replaced by *ab-initio* norm conserving pseudopotentials, generated using the Troullier-Martins scheme[12], in the Kleinman-Bylander fully non-local separable representation[13]. In order to avoid the spiky oscillations close to the nucleus we have included small partial core corrections[14] for all the atoms. The reference configuration and cutoff radii for each angular momentum shell, and the matching radius between the full core charge density and the partial core charge density for the nonlinear core corrections (NLCCs) for the pseudopotentials used in this work can be found in Table 1 for H, C, N, Cl, Fe.

The one-electron Kohn-Sham eigenstates were expanded on a basis of strictly localized numerical atomic orbitals[15]. We used a double-ζ plus polarization for the valence states of all the atoms. The atomic shells explicitly included in the simulations are the 1*s*, 2*p* for H; 2*s*, 2*p*, 3*d* for C and N; 3*s*, 3*p*, 3*d* for Cl; and 4*s*, 4*p*, 3*d* for Fe. All the parameters that define the shape and range of the basis functions were obtained by a variational optimization of the enthalpy[16] (with a pressure P=0.1 GPa), using the coordinates of Dimim[$FeCl_4$] obtained by Rietveld refinement of neutron powder diffraction data.

The electronic density, Hartree, and exchange correlation potentials, as well as the corresponding matrix elements between the basis orbitals, were calculated in a uniform real space grid. An equivalent plane wave cut-off of 350 Ry was used to represent the charge density. For the Brillouin zone integrations we use a Monkhorst-Pack sampling[17] of 3 × 2 × 3, equivalent to a real-space cut-off of 10Å[18].

Starting from the experimental coordinates obtained by neutron powder diffraction data, a full optimization of the crystal lattice parameters and atomic positions was carried out, until a maximum component of the force on any atom was smaller than 0.01 eV/Å and the maximum component of the stress tensor was smaller than 0.0001 eV/$Å^3$.

The intramolecular geometries and distances of the $Dimin^+$ cation and $FeCl_4^-$ anion obtained by DFT calculations lie in the expected range comparable to those found in experimental data (overestimation within the range from 2 to 3 %). The intermolecular distances and orientations are in good agreement with the experimental results, thus confirming that the VDW functionals do not introduce any unwanted features in the description of the low temperature structure.

Table S.7. Reference configuration and cutoff radii of the pseudopotentials used in our study. Units in Bohr.

Reference		H $1s^1, 2p^0, 3d^0, 4f^0$	C $2s^2, 2p^2, 3d^0, 4f^0$	N $2s^2, 2p^3, 3d^0, 4f^0$	Cl $3s^2, 3p^5, 3d^0, 4f^0$	Fe $4s^2, 4p^0, 3d^6, 4f^0$
Core radius	*s*	1.00	1.30	1.35	1.40	2.10
	p	1.25	1.30	1.35	1.40	2.40
	d	1.25	1.30	1.35	1.50	2.00
	f	1.25	1.30	1.35	1.50	2.00
Scalar relativistic ?		no	no	no	no	yes
Core corrections ?		no	yes (1.40)	yes (1.30)	yes (1.30)	yes (0.70)

Table S.8. Mulliken spin populations obtained by DFT. The atoms in the imidazolium cation have a value of 0.

atom	Spin population
Fe	3.916
Cl1	0.262
Cl2	0.273
Cl3	0.252
Cl4	0.273

Theoretical calculation of the exchange coupling constant.

Calculations of different magnetic interactions between the irons were carried out in order to obtain an estimation of the intra and interplane exchange coupling. To achieve that it was used a Hamiltonian of the type $\mathcal{H} = \sum 2J_{ij}S_i \cdot S_j$ where J_{ij} is the exchange constant and defined positive for an antiferromagnetic coupling, and the product $S_i \cdot S_j$ is taken as +1 for ferromagnetic coupling and -1 for antiferromagnetic coupling.

Figure S12 shows the schematic view of the possible exchange pathways for Dimin[$FeCl_4$] via (a) interplane and (b) intraplane Fe–Cl--Cl–Fe bridges. Being careful not to repeat interactions, according tosymmetry rules, the following expression for theoretical calculation of the exchange coupling constant obtained is:

$$E(configuration) = E_0 + 2 \cdot (\pm 4J_{\perp} \pm 8J_{\parallel}) \qquad (5)$$

where E_0 is the cell Energy without magnetic interactions; $J_{\perp}$ and $J_{\parallel}$ the inter and intraplane exchange coupling constants respectively.

The configurations calculated with the energy and the differences of energies from the ground state are depicted in Table S.9. Indeed, the value of the exchange constants can be obtained calculating the difference between configurations.

Table S.9. Energy and difference of energy from ground state (GS) for the different spin configurations calculated by DFT.

Type	Interplane coupling	Intraplane coupling	Energy / eV/cell	$\Delta E \cdot 10^3$ from GS / eV/cell
G	AF	AF	-16739.274073	GS
C	F	AF	-16739.270353	+3.72
A	AF	F	-16739.265381	+8.69
F	F	F	-16739.263488	+10.59

With this result, the value of the exchange coupling constants obtained are $J_{\perp}$= -5.6± 0.5 and $J_{\parallel}$ = -1.0± 0.5 K for the interplane and intraplane interactions, respectively.

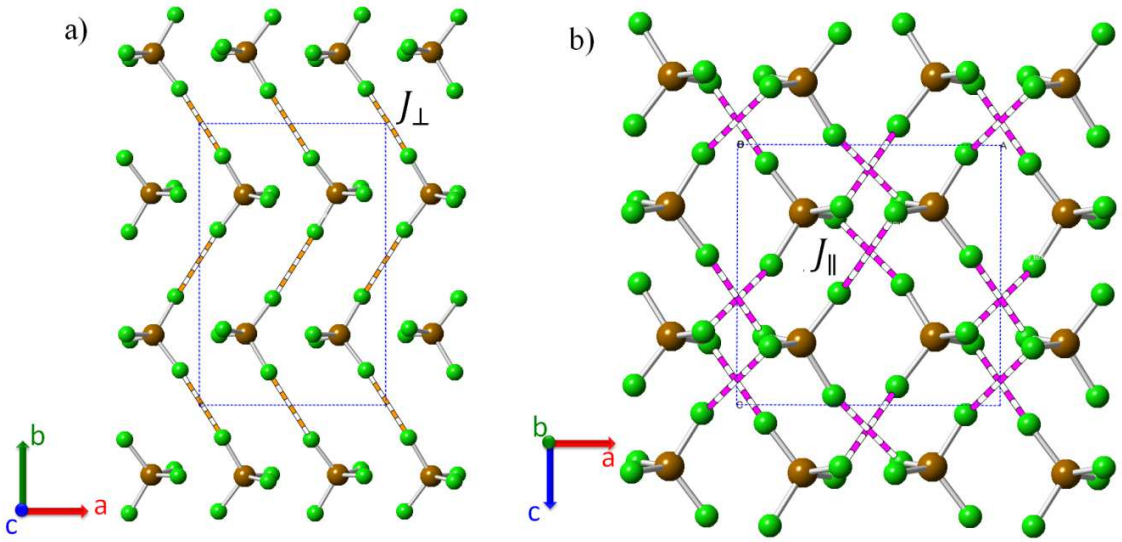

Figure S.12. Schematic view of the possible magnetic exchange pathways for Dimin[$FeCl_4$] via (a) interplane and (b) intraplane Fe–Cl--Cl–Fe bridges.

Table S.10. Selected geometrical parameters, bond lengths (Å) and angles (°) obtained from neutron diffraction (experimental) and DFT (calculated) related to the possible magnetic exchange pathways for Dimin$FeCl_4$.

Magnetic exchange Pathways	Direct distance Fe-Fe/Å	Length of exchange pathway/Å	Bond/Å Fe-Cl	Bond/Å Cl-Cl	Bond/Å Fe-Cl	Angle/° Fe-Cl-Cl	Angle/° Cl-Cl-Fe
J1 (exp.)	8.197 (1)	8.220	2.178	3.871	2.171	173.4	174.4
J2 (exp.)	6.537 (1)	8.120	2.171	3.808	2.140	91.1	154.4
J3 (exp.)	6.242 (1)	7.964	2.178	3.631	2.155	89.6	157.2
J1 (calc.)	8.480 (1)	8.506	2.275	3.960	2.271	174.7	173.2
J2 (calc.)	6.799 (1)	8.357	2.271	3.819	2.267	93.3	158.2
J3 (calc.)	6.529 (1)	8.434	2.275	3.886	2.273	87.0	156.8

References of Supplementary Material:

[1] O. Vallcorba, J. Rius, C. Frontera, C. Miravitlles, *Journal of Applied Crystallography* **2012**, *45*, 1270-1277.
[2] O. Vallcorba, J. Rius, C. Frontera, I. Peral, C. Miravitlles, *Journal of Applied Crystallography* **2012**, *45*, 844-848.
[3] T. Bäcker, O. Breunig, M. Valldor, K. Merz, V. Vasylyeva, A.-V. Mudring, *Crystal Growth & Design* **2011**, *11*, 2564-2571.
[4] J. Rius, ribols18 A Computer Program for Least-Squares Refinement from Powder Diffraction Data Institut de Ciència de Materials de Barcelona (CSIC), Barcelona, Spain **2009**.
[5] G. R. Wagner, S. A. Friedberg, *Physics Letters* **1964**, *9*, 11-13.
[6] J. C. Bonner, M. E. Fisher, *Physical Review* **1964**, *135*, A640-A658.
[7] G. S. Rushbrooke, P. J. Wood, *Mol Phys* **1958**, *1*, 257-283.
[8] M. S. José, A. Emilio, D. G. Julian, G. Alberto, J. Javier, O. Pablo and S.-P. Daniel, *J. Phys.: Condens. Matter* **2002**, 14, 2745-2750.
[9] G. Román-Pérez, J. M. Soler, *Physical Review Letters* **2009**, *103*, 096102.
[10] M. Dion, H. Rydberg, E. Schröder, D. C. Langreth, B. I. Lundqvist, *Physical Review Letters* **2004**, *92*, 246401.
[11] J. Kohanoff, C. Pinilla, T. G. Youngs, E. Artacho, J. M. Soler, *The Journal of chemical physics* **2011**, *135*, 154505.
[12] N. Troullier, J. L. Martins, *Physical Review B* **1991**, *43*, 1993-2006.
[13] L. Kleinman, D. M. Bylander, *Physical Review Letters* **1982**, *48*, 1425-1428.
[14] S. G. Louie, S. Froyen, M. L. Cohen, *Physical Review B* **1982**, *26*, 1738-1742.
[15] aO. F. Sankey, D. J. Niklewski, *Physical Review B* **1989**, *40*, 3979-3995; bE. Artacho, D. Sánchez-Portal, P. Ordejón, A. García, J. M. Soler, *physica status solidi (b)* **1999**, *215*, 809-817.
[16] E. Anglada, J. M. Soler, J. Junquera, E. Artacho, *Physical Review B* **2002**, *66*, 205101.
[17] H. J. Monkhorst, J. D. Pack, *Physical Review B* **1976**, *13*, 5188-5192.
[18] J. Moreno, J. M. Soler, *Physical Review B* **1992**, *45*, 13891-13898.

3.3. Artículo IV

Artículo en preparación “Slow Dynamically Solid-to-Solid Phase Transition Induced by Thermal Treatment on DimimFeCl4 Magnetic Ionic Liquid”

Slow Dynamically Solid-to-Solid Phase Transition Induced by Thermal Treatment on DimimFeCl$_4$ Magnetic Ionic Liquid

Abel García-Saiz[†], Imanol de Pedro[†]*, Oscar Fabelo[Ψ], , Oriol Vallcorba[¥], Javier Junquera[†], Jesús Angel Blanco[Ж], João Carlos Waerenborgh[Л], D. Andreica[¥], Andrew Wildes[Ψ], María Teresa Fernández-Díaz[Ψ], and Jesús Rodríguez Fernández[†]

[†] CITIMAC, Facultad de Ciencias, Universidad de Cantabria, 39005 Santander.
[¥] ALBA Synchrotron Light Source, Cerdanyola del Vallés, Barcelona, Spain.
[Ψ] Institut Laue-Langevin, BP 156X, F-38042 Grenoble Cedex, France.
[Ж]Departamento de Física, Universidad de Oviedo, 33007 Oviedo, Spain.
[Л] Centro de Ciências e Tecnologias Nucleares, Instituto Superior Técnico, Universidade de Lisboa, 2695-066 Bobadela LRS, Portugal
[¥] Faculty of Physics, Babes-Bolyai University, 400084 Cluj-Napoca, Romania

ABSTRACT: As in other liquids, the crystal structure of the solid phases of 1,3-dimethylimidazolium tetrachlorideferrate (DimimFeCl$_4$) magnetic ionic liquid (MIL), is closely related with the thermal history. In this work we describe a series of solid-to-solid phase transitions from the room temperature (RT), phase **II** [space group (s.g.) = $P2_1$]**,** to low temperature phases, **I-a** [s.g. = $P2_12_12_1$] or **I-b** [s.g. = $P2_1$/c], depending on the cooling procedure [quenching or fast cooling (**II → I-a**) or slow cooling with temperature stabilization (**II → I-b**)]. The temperature evolution of these phases in a warming procedure was characterized (from **I-a** to **I-b** and from **I-b** to **II**). The **I-a** to **I-b** solid-to-solid phase transition involves a slow translational and reorientational dynamical process of both, the imidazolium cation and the tetrachlorideferrate anion. These processes have been characterized using synchrotron powder X-ray and neutron powder diffraction and DFT (density functional theory) studies.

The results reported here represent one of the few direct experimental evidences supporting the existence of a solid to solid phase transition induced by thermal treatment, and, to our knowledge, the first in these systems. This is connected with the modification of the super-exchange pathways of both low temperature phases (**I-a** and **I-b**) which show a global antiferromagnetic behavior. A combination of several experimental methods: magnetometry, Mössbauer and Muon spectroscopy together with polarized and non-polarized neutron powder diffraction has been used in order to shed more light and characterize the different features observed in these phases.

INTRODUCTION

Nowadays, there is an increasing scientific effort to design and synthesize ionic liquids (ILs), with novel applications on the horizon. Ionic Liquids (ILs) designed for specific tasks can now be found,[1-5] for energy applications such as batteries and ultracapacitors,[6-9] ILs which capture the carbon dioxide,[10,11], that dissolve cellulose[12,13] etc. Among them one of the highlight are the magnetic ionic liquids (MILs)[14]. Owing to their magnetic nature, these compounds have been exploited in a wide range of applications including magnetic hydraulics in engineering,[15] or magnetic surfactants.[16]

Despite the quest for new ILs for technical applications, their physical properties are still not fully understood. For example, there is large research and debate if the structure of these molecular liquids can be inferred from its parent solid crystal; i.e. if the mixture and intensity of their intermolecular forces induces a strong association or self-assembly in the liquid state.[17] In this sense, the effect of temperature on imidazolium ILs nanostructure has been examined via numerous experimental and theoretical techniques [17,18]. Among them, the X-ray scattering experiments[19] and molecular dynamic simulations[20] provide an useful information about their structural correlations. In the case of MILs, without doubt, there is a large scientific interest to search the nature and consequences of their ion self-assembly. This is due to the fact that the structural ordering [21,22] appears to be more pronounced in MILs than in conventional ILs and has a strong influence on the macroscopic properties of the fluid[23]. Moreover, molecular motion in crystalline solids are also attracting the interest of the scientific community.[24,25] Materials that are capable of rotational motion, such as imidazolium based compounds,[26,27] in response to outside driving forces such as light, heat, or electric fields are extremely useful for the development of nanoscale devices or for obtaining new ferroelectric materials.

In a previous study,[28] we have performed a preliminary investigation of the thermal properties, (by differential scanning calorimetry) the crystal structure (by neutron powder diffraction and DFT calculations) and of the magnetic properties (by magnetic susceptibility and magnetization measurements) of Dimin$FeCl_4$. It showed two solid–solid (s–s) phase transitions around 332 and 285 K upon a fast cooling from above the melting point (348 K). The RT solid phase, labelled as phase **II,** crystallizes in the polar space group $P\,2_1$ (No. 4) with a = 6.5434(2) Å, b = 14.0286(3) Å, c = 6.5314(2) Å, β = 89.921(1)° unit cell and V = 599.55(4) Å^3. The low temperature phase, labelled as **I** (in the present work it is phase **I-a**) crystalizes in the acentric space group $P2_12_12_1$. (No. 19) with a = 9.1242(1) Å, b = 13.8132(2), c = 9.0359(1) Å, V = 1138.84(2) Å^3 at 10 K. Both unit cell are related by a rotation of 45º along the monoclinic axis ($a' = a + c$, $b' = b$, $c' = a\text{-}c$) plus a translation. Their crystal structures can be described as a succession of organic and inorganic layers extended in *ab*-plane and stacked along the *b*-axis. The shortest intra-layer Fe-Fe distances is about 6.5 Å; distance which is notability smaller than the shortest Fe-Fe inter-layer

distance (ca 8.2 Å). Although the change of the space group produces changes on the orientation of both the imidazolium counterion and the tetrachlorideferrate anion, the topology of both networks is the same. A detailed descriptions of both crystal structures as well as a tabulated list of the most important crystallographic parameters can be consulted on ref. 28.

Below the temperature of the solid-to-solid phase transition, the phase **I-a** is stable, under fast cooling ratio, down to 2 K (base temperature). Their neutron diffraction data show the occurrence of long range magnetic order below 3 K. However, all our attempts to determine their magnetic structure were unsuccessful due to the occurrence of very weak magnetic reflections.[28]

In this paper, we connect our preliminary study[28] with the investigation of a new phase, hereafter referred to as **I-b**, obtained after a simple thermal treatment. Initially, phase **I-b** was not observed by differential scanning calorimetry or specific heat using PPMS (see ref 28) neither on cooling nor on warming the sample. In this work we have determined its crystal structure combining synchrotron and neutron powder diffraction, corroborated by with the results of density functional theory studies.

We have also investigated the mechanism of transformation from phase **I-a** to phase **I-b**. This study has been connected with the alterations observed of the macroscopic magnetic interactions. Although both phases show a global antiferromagnetic behavior, a combination of magnetometry, Mössbauer and Muon spectroscopy data together with non-polarized and polarized powder neutron diffraction experiments have been needed to shed light to the unusual features observed at low temperature in both phases. Finally, we have used non-polarized neutron diffraction data to determine the magnetic structure of phase **I-b,** which shows similar characteristic than phase **I-a**. Moreover, a remarkable increase of background at low temperatures has been detected in the non-polarized neutron diffraction analysis. This effect is much more evident in the phase **I-a**, appearing at a similar temperature range that the long-range magnetic ordering, which initially suggests a magnetic source. Polarized neutron diffraction through the xyz-polarized analysis technique have been used to understand the origin of this unusual behavior.

RESULTS AND DISCUSSION

Phase transition induced by thermal treatment. From the previous X-ray and neutron diffraction data, we know that the Diminf$FeCl_4$ compound present a structural phase transition from RT (**II**) to a low temperature phase (**I-a**). In the previous publication, the sample was always cooled down using a "fast" protocol, either using a thermal quenching of the sample in a N_2 flux (down to about 100 K), or within a cryo-stream device for X-ray powder diffraction or placing the sample into a standard orange cryostat, pre-cooled to increase the cooling rate.

Surprisingly, while warming up from 100 to 300 K, the Dimim$FeCl_4$ displays an unexpected phase transition [Figure S1 (a)]. The occurrence of this phenomena depends on the warm-up velocity. It could be stabilized from phase **I-a** only when the temperature was kept above 180 K several minutes (Figure S2). The same protocol was followed in cooling mode from phase **II** with a cooling velocity of circa 2 K/min but the phase **I-b** was not obtained. However, phase **II** exhibits a thermo-structural change to phase **I-a** at similar temperatures as those obtained from DTA data (280 K). [Figure S1(b)]. For lower velocities, a mixture of both phases (**I-a** and **I-b)** appears sometimes (up to now we could not obtain a pure phase **I-b** in cooling mode). This is indicative of a decrease of reversibility compared with the warm-up protocol. It is worth mentioning that after phase **I-b** is formed it is stable down to the base temperature. Above 260 K, it transforms to phase **II** [Figure S1 (a)], which is stable at RT.[28]

Crystal Structure Determination. The Rietveld analysis of phase **I-b** was completed using a multipattern approach, combining the synchrotron data with the high resolution neutron diffraction pattern. The details are presented in the supplementary material. The experimental, calculated and difference powder diffraction profiles are shown in Figure 1 and Figure S3. The final structural parameters and figures of merit of the last refinements are summarized in Tables S1 and S2 and the positional parameters are given in Tables S3, S4 and S5.

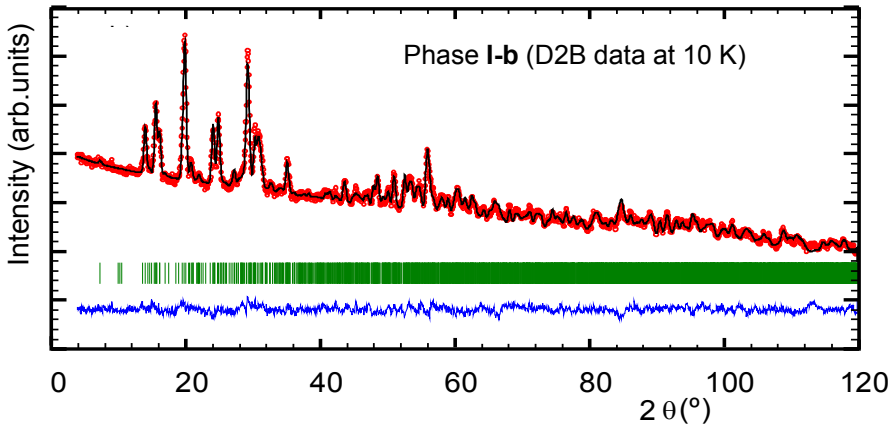

Figure 1. Observed (red points) and calculated (blue solid line) powder diffraction pattern for phase **I-b** of Dimim[$FeCl_4$] at 10 K obtained in the NPD D2B (λ = 1.5938 Å). Positions of the Bragg reflections are represented by vertical bars. The observed-calculated difference patterns are depicted as a blue line in the bottom of the figure.

The phase **I-b** crystallizes in the centrosymmetric monoclinic space group $P2_1/c$ (No. 14) with a = 14.1391(3) Å, b = 13.7039(3) Å, c = 13.2935(3) Å, β = 115.539(2)°, V = 2324(4) Å^3, Z = 2 ρ_{calc} =1.685 g/cm^3, T = 220 K. The crystal structure can be described as a stacking of organic $[Dimim]^+$ and inorganic $[FeCl_4]^-$ layers extended in the *ac*-plane and pillared along the *b*-axis, following a *ABCDABCD* sequence similar to that observed on phases **II** and **I-a**. Each of the *ac*-layers are built up from two independent $[Dimim]^+$ counterions and two $[FeCl_4]^-$ anions. Although the

topology of phase **I-b** is the same as that of the previous ones,[28] the occurrence of two crystallographically independent cations and anions give rise to two different orientations of this building blocks. The change of the orientation of the two independent $[FeCl_4]^-$ metal complex is not very dramatic, and can be seen as a slight rotation with respect to the initial position. The Fe···Fe distances within the *ac*-layer is larger than 6.2 Å, slightly shorter that those observed in phases **II** and **I-a**. However, the $[FeCl_4]^-$ anions in all phases are fairly regular [mean values of Cl-Fe-Cl bond angles are 109(4)º, 110(3)º and 108(3)º for **II**, **I-a** and **I-b**, respectively] with similar bond lengths [mean values 2.18(6) Å , 2.20(2) Å and 2.21(2) Å].

The $[Dimim]^+$ cations of phase **I-b**, after the phase transition from **I-a**, present a reorientation which involve a non-negligible atomic displacements. In order to better understand the changes after this phase transition induced by thermal treatment, the crystal structure of **I-b** displays zig-zag organic-inorganic planes stacked in the [-1, 0, 1] direction whereas for the phase **I-a**, these are extended in the *bc*-plane and pillared along the *a*-axis (see Figure 2). In phase **I-b,** these layers can be described as chains of the imidazolium cations extended along the [1, 0, 1] direction and separated by chains of $[FeCl_4]^-$ anions extended along the same position. Within these chains the $[Dimim]^+$ cation shows a flip along the *c*-axis within a small distortion along the *a*-direction. This reorientation was not observed in any of the previous phases (**II** and **I-a**).[20] The dihedral angles of the imidazolium ring to the methyl groups [∠ (C-N-C-N)] in all phases range from 177 to 180°. The refined values for the C-C and C-N bond lengths of **I-b** lie in the expected range and are comparable to those found in other imidazolium compounds, as for example in DimimX (X = Cl and Br),[29] $Bmim_2[XCl_4]$ (X = Fe, Ni and Co)[30] $EdimimFeX_4$ (X = Cl and Br)[21] and $EmimFeCl_4$.[31]

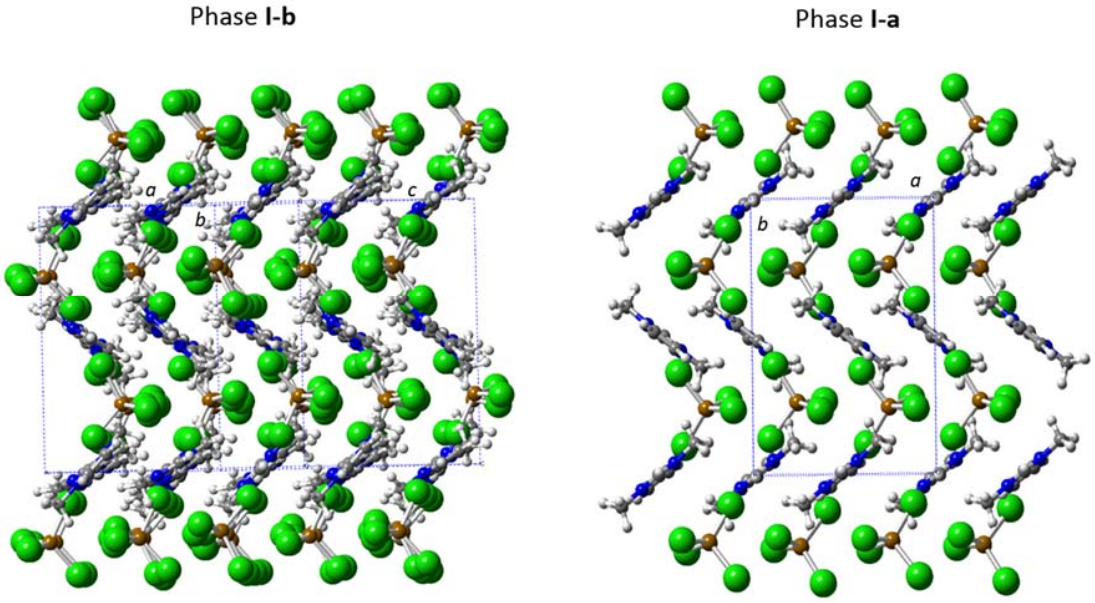

Figure 2. Crystal structures of phase **I-b** and **I-a**. Orange (iron), gold (chloride), grey (carbon), blue (nitrogen) and white (hydrogen). The blue dashed square represents the unit cell

Physical Characterization: Magnetometry measurements. The reorientations of the cation and anion groups after the phase transition modifies the super-exchange interactions observed in the phase **I-a**, and therefore their magnetic behavior. In order to unambiguously compare the magnetometry measurements of both phases the magnetic measurements were carried out according to the following thermal treatment: the sample, crystallized in the RT phase (**II**), was quenched at 100 K using the SQUID cryostat in order to obtain the phase **I-a**. After that, the temperature was cooled and the magnetic study performed. In order to transform phase **I-a** into phase **I-b**, the temperature was warmed until 220 K and it was kept constant for 1 hour (in order to ensure that the sample is completely converted into phase **I-b**). After that, the temperature was decreased and the magnetic study of the phase **I-b** was performed.

Figure 3 (a) shows the temperature dependence of the molar magnetic susceptibility (χ_m) and inverse susceptibility ($1/\chi_m$) curves of phases **I-a** and **I-b**, measured at 1 kOe after cooling without an applied magnetic field (ZFC). The molar magnetic susceptibilities increase with decreasing temperature up to 3.1 and 5.4 K for phase **I-a** and **I-b** respectively, where a broad maximum is observed suggesting the existence of a long-range magnetic ordering. It disappears in the phase **I-a** for fields higher than 20 kOe, suggesting a partial compensation of the antiferromagnetic interactions. However, the magnetic behaviour as a function of the external magnetic field in the phase **I-b** is slightly different; the maximum of χ_m is shifted to lower temperatures. It is located at 4.15 K for an applied field of 50 kOe, suggesting that the antiferromagnetic interactions remain mainly unchanged (Figure S4). The magnetic data at 1 kOe were fitted in the paramagnetic range using the Curie-Weiss law for S= 5/2 in the molecular field approximation[32]. The least-squares fit of the experimental data from 10 to 220 K is shown in Figure 3 (a). The Curie constant (C) and Curie-Weiss temperature (θ_P), obtained by the fitting, have a values of 4.38 and 4.44 emuK/molOe and of -6.9 and -8.5 K, for phase **I-a** and **I-b** respectively, while, the fit gives a value of *zJ,* for **I-a** and **I-b**, of -0.29 and -0.35 K respectively. This value points to weak antiferromagnetic interactions, in accordance with the large distances between iron complex anions (longer than 6.5 Å) being in agreement with the values previously reported for this type of magnetic pathways.[21,22,33]. This Curie constant corresponds to an effective paramagnetic moment μ_{eff} = 5.92 and 6.01 μ_B/Fe ion, in good agreement with the expected value of 4.38 emuK/molOe (5.92 μ_B) for Fe^{3+} ion with a magnetic spin S = 5/2 and with those found for other paramagnetic compounds based on $[FeCl_4]^-$ ion.[34] Moreover, the temperature dependence of ZFC-FC curves at 10 Oe of each phase does not show any splitting below the broad maxima detected [see inset in Figure 3 (a)], discarding the occurrence of a weak spin-canting or a weak ferromagnetic signal coming from the non-compensation of the different magnetic sites. The possible dynamical

response of the magnetic ordering of both phases up to 2 K was discarded by AC magnetic susceptibility measurements (Figure S5).

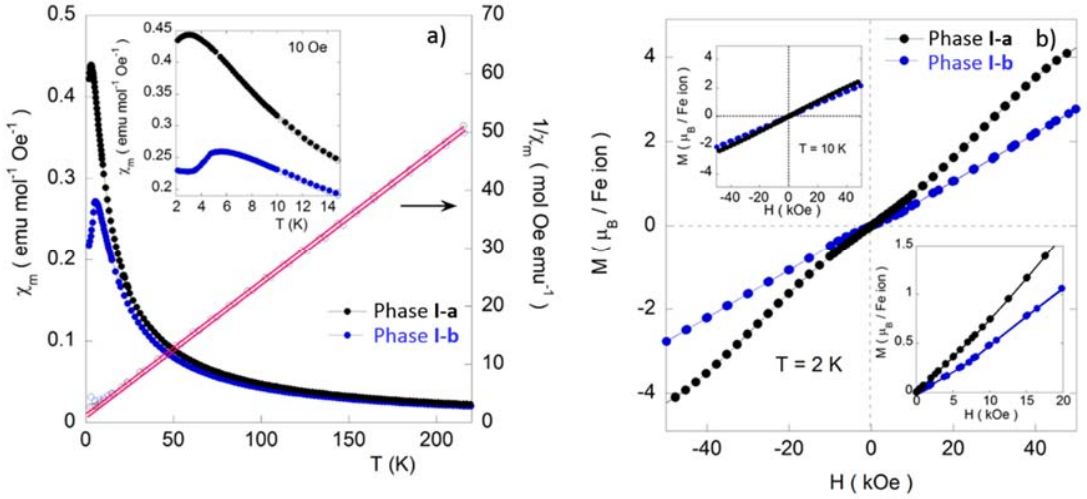

Figure 3. (a) Temperature dependence of χ_m and $1/\chi_m$ for phase **I-a** and **I-b** measured under 1kOe. The solid red line is the fit according to Eq. (1) of the manuscript. The upper inset shows the low temperature ZFC-FC magnetic susceptibility at 10 Oe.(b) Magnetization vs. applied magnetic field at 2 and 10 K (upper inset) for phase **I-a** and **I-b**.

The field dependence of the magnetization of phase **I-a** and **I-b** at 10 K shows a linear behaviour in the whole applied field range confirming the paramagnetic behaviour at this temperature [see upper inset of Figure 3 (b)]. At 2 K, below the Néel temperature of both compounds, the M(H) curves are anhysteretic confirming the absence of a ferromagnetic component. The value obtained at 50 kOe for the phase **I-a** (4.20 μ_B/Fe ion) is not far from the expected fully-saturated value for a Fe^{3+} ion (5 μ_B/Fe ion). However, after the structural transition to **I-b** the magnetization at 50 kOe is only 2.15 μ_B/Fe ion. This value is far away from the data reported for other MILs based on tetrachloroferrate exhibiting three-dimensional ordering, where the magnetization tends towards saturation for magnetic fields lower than 50 kOe [21,35,36] This feature indicates that in this system with isotropic exchange interactions [as is expected for Fe(III)], the anisotropy of the magnetic structure plays an important role. Finally, the field dependence of the magnetization of **I-b** displays a small inflection point near 10 kOe, which is connected with the suppressed drop of magnetic susceptibility measurements for fields higher than 10 kOe; therefore, this could be the result of a modification of the magnetic structure that changes under the effect of the magnetic field (see description of the magnetic structure).

Mössbauer measurements. The Dmim[$FeCl_4$] sample was cooled at a constant rate of approximately 10 K /minute from room temperature down to 70 K in order to perform a thermal quenching. The spectra of phase **I-a** were then obtained in the range 70-1.9 K. Afterwards, the sample was heated up to 220 K and kept at this temperature for one hour in order to guarantee the

occurrence of the solid to solid phase transition. After this treatment the sample was cooled down to 70 K and the Mössbauer study of phase **I-b** was performed.

The Mössbauer spectra of phase **I-a** and **I-b** Dmim[$FeCl_4$] (Figure 4) at 6 K and above consist of a single absorption peak similar to that observed for choline[$FeCl_4$][34] and the analogous tetrahalometallate ionic liquid, Dimim[$FeBr_4$].[22] The analysis of the spectra reveals that this peak is not adequately fitted by a single lorentzian line. It consists of a quadrupole doublet with quadrupole splitting, QS, smaller than the line widths of the individual lines (Table S6). This denotes a small electric field gradient at the iron nucleus, and consequently a highly symmetric electric charge distribution around the iron cation with the sp^3 orbitals giving rise to an almost perfect tetrahedral environment. The estimated isomer shifts relative to metallic Fe at 295 K, IS, for phases **I-a** and **I-b** are equal within experimental error to those of high-spin Fe^{3+} (spin state S=5/2) in compounds where Fe^{3+} is tetrahedrally coordinated by Cl^- [34,37,38] and slightly lower than in $FeCl_3$ where Fe^{3+} has octahedral environment.[39] The fact that no magnetic splittings are observed shows that Fe^{3+} is in a paramagnetic state, the relaxation frequency of the Fe^{3+} magnetic moments, ω_R, being much faster than 10^{-8} Hz, the Larmor precession frequency of the ^{57}Fe nucleus, ω_L.

Below 6 K the spectra depend on the crystallographic phase. Phase **I-a** spectra show that all the Fe^{3+} remains in a paramagnetic state down to 2.1 K. Below this temperature, at 1.9 K, a significant broadening of the doublet peaks is observed (Table S6, Figure 4) consistent with a slowing down of ω_R and with the onset of magnetic ordering observed by magnetic susceptibility measurements near 3 K. In contrast to the magnetic behaviour of phase **I-a**, **I-b** at 4 K and below displays a well-defined six-peak pattern which implies that ω_R has dropped well below 10^{-8} Hz. The abrupt change in ω_R within a narrow temperature range is typical of the establishment of long-range magnetic correlations of the Fe^{3+} sublattice. The sharpness of the transition as well as the narrow peaks observed in the Mössbauer spectra further suggest long range magnetic ordering rather than a spin-glass-like transition. Noteworthy, the six-peak patterns observed at 4 K and below are not symmetrical revealing that two magnetic hyperfine splittings are necessary to fit each spectrum. Both magnetic sextets have equal areas within experimental error (Table S6), in agreement with two different Fe^{3+} magnetic sublattices each containing equal numbers of Fe^{3+}. Quadrupole shifts, (2ε), are also different for each sextet which is related with occurrence of two different directions of iron magnetic moments with respect to the crystallographic axes. The temperature dependence of the (2ε) values is shown in Figure S6.

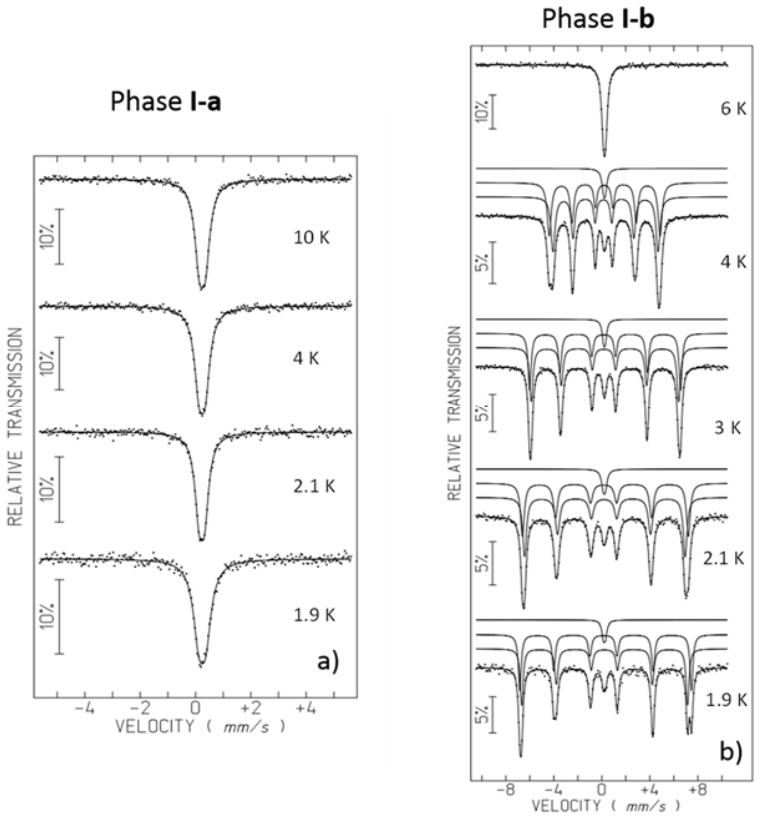

Figure 4. Mössbauer spectra of phases **I-a** and **I-b** collected at different temperatures between 10 and 1.9 K. In phase **I-b** approximately 6% of the Fe^{3+} in the polycrystalline Mössbauer absorber remains paramagnetic probably incorporated in domains with defects at the surface of the small crystal particles.

Muon Spin Spectroscopy. The μSR experiments were performed in zero applied field in the temperature range 1.6–200 K. The sample was mounted in a special "cup shape" aluminium container covered with a thin layer of mylar tape to prevent leakage. The thermal quenching-heating process was done using a Quantum cryostat following the same experimental protocol as in the NPD experiment.

Low temperature μSR spectra recorded on the phase **I-a** are shown in Figure 5, within a comparison with the μSR results on the phase **I-b**. As can be see, there is a huge difference between the first and second cooling process. However, if compared at the same time scale, the runs at 5.2 K, in the paramagnetic state, are not very different.

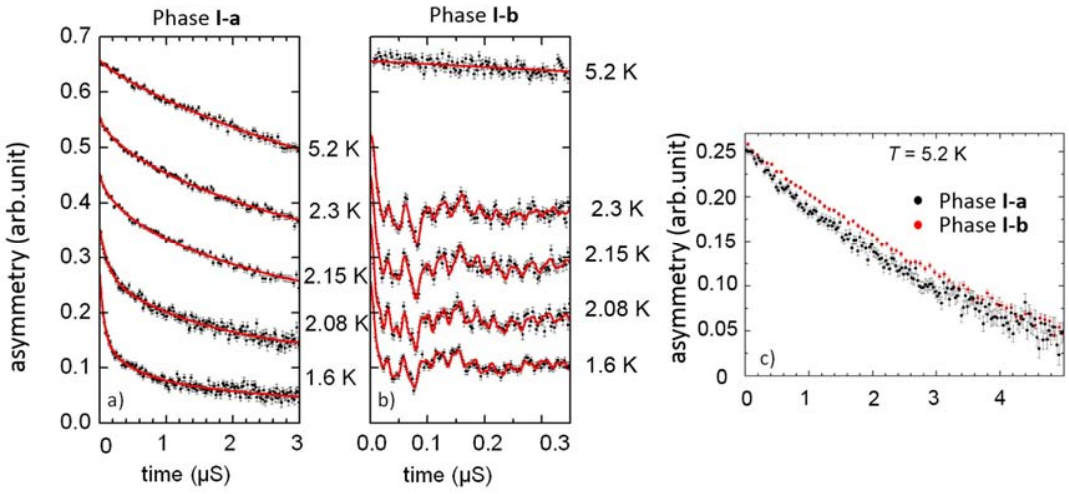

Figure 5. Comparison of spectra recorded and fitted of phase **I-a** (a) and phase **I-b** (b). Observe the different time scale. (c) μSR spectra recorded on two phases at 5.2 K.

On one hand, the phase **I-a** spectra recorded down to 2.07 K were fitted with a product of a Kubo-Toyabe[40] and a stretched exponential characteristic of a depolarization due to a static field distribution created by the nuclear magnetic moments and a distribution of fluctuation rates of the electronic moments (see Figures S7 and S8):

$$AP(t) = A\left(\frac{1}{3} + \frac{2}{3}\Delta^2 t^2\right) e^{-\frac{\Delta^2 t^2}{2}} e^{-(\lambda t)^{\beta}} \quad (1)$$

where $\beta = 1$ corresponds to a pure exponential relaxation rate while for β = 2, the relaxation rate is Gaussian.

Below 2.07 K, spectra could not be fitted using the same function. Instead, a combination of fast (2/3 term) /slow (1/3 term) relaxing exponentials with an amplitude ratio of about 2/1 was used, as expected for a magnetic sample: $AP(t) = \left(A_1 e^{-\lambda_1 t} + A_2 e^{-\lambda_2 t}\right) + A_3 e^{-\lambda_3 t}$. The "magnetic part" of the μSR spectra of **I-a** phase could be described by a purely exponential $A_{magn} P_{magn}(t)$, i.e. no oscillations are observed in the μ_{SR} spectra. The fitted parameters up to 1.6 K (see supplementary material and Figures S9 and S10) confirm the onset of a magnetic ordering detected by Mössbauer measurements and suggest that the ordering can not be static below 2K.

On the other hand, the phase **I-b** spectra recorded below 5.2 K indicates that the sample becomes magnetic. For example, at 2.3 K one clearly observe clearly that a fast component develops with several oscillations. These spectra were fitted using 4 oscillatory components,

$$AP(t) = A_1 e^{-\lambda_1 t}\cos(2\pi\nu_1 t + \varphi_1) + A_2 e^{-\lambda_2 t}\cos(2\pi\nu_2 t + \varphi_2) + \\ + A_3 e^{-\lambda_3 t}\cos(2\pi\nu_3 t + \varphi_3) + A_4 e^{-\lambda_4 t}\cos(2\pi\nu_4 t + \varphi_4) + A_5 e^{-\lambda_5 t} + A_6 e^{-\lambda_6 t} \quad (2)$$

which describe the behavior of muons stopped in an interstitial site where they "see" magnetic field (see Figure S.11). For more details of the technique, functions and thermal fitted parameters see the supplementary material.

Magnetic structure determination. In order to determine the magnetic structure of phase **I-b**, we have carried out low temperature neutron diffraction using the high flux D1B diffractometer, working with λ = 2.52 Å. Initially, the sample was milled and placed in a cylindrical vanadium container at room temperature (phase **II**). After that, it was placed inside the orange cryostat at 100 K in order to perform the thermal quenching of the sample (phase **I-a**). Next, the temperature was warmed following a ramp up to 220 K and after waiting10 min, the sample **I-a** was completely converted to phase **I-b**. [see Figure S2]. This suggests that the structural transformation occurs when the temperature is stable during enough time to allow the moving of the anions in the system. Therefore, the crystal phase transition should be dependent on the time in a temperature range between 180 and 260 K (temperature where the phase transition to **I-b** structure was observed). After that, the sample with the phase **I-b** structure was cooled down to 1.8 K to collect the neutron diffraction data in the magnetic order phase.

The magnetic ordering of phase **I-a** was previously studied by high flux (D1B with λ = 2.52 Å) and high resolution neutron powder diffraction patterns (D2B with λ = 1.5938 Å). The comparative view of the D1B nuclear pattern (10 K) and the magnetic ones (1.8 K) of phase **I-a** reveals a small sharp Bragg peak (marked with * in Figure 6). This additional elastic intensity is weak, but sufficient to prove the long range antiferromagnetic order. The temperature evolution of the D1B patterns between 1.8 and 10 K [see right inset Figure 6 (a)] shows that the magnetic peaks disappear at temperatures below around 3 K. Moreover, a considerable diffuse scattering overlapping is detected below around 2θ = 40º, which increases in a monotonous way below 9 K. Rietveld refinements above the magnetic phase transition show that The $P2_12_12_1$ symmetry is maintained from 1.8 to 10 K. Initially, the presence of this unusual behavior was linked to additional magnetic phenomena such as short-range magnetic ordering superposed to the long range magnetic order, as observed in other geometrically frustrated antiferromagnetic materials.[41,42] However, it could arise from other causes such as, nuclear spin-incoherent scattering, random or internal strain.[43] Therefore, 'xyz'-polarization analysis was performed in order to understand its origin (see below).

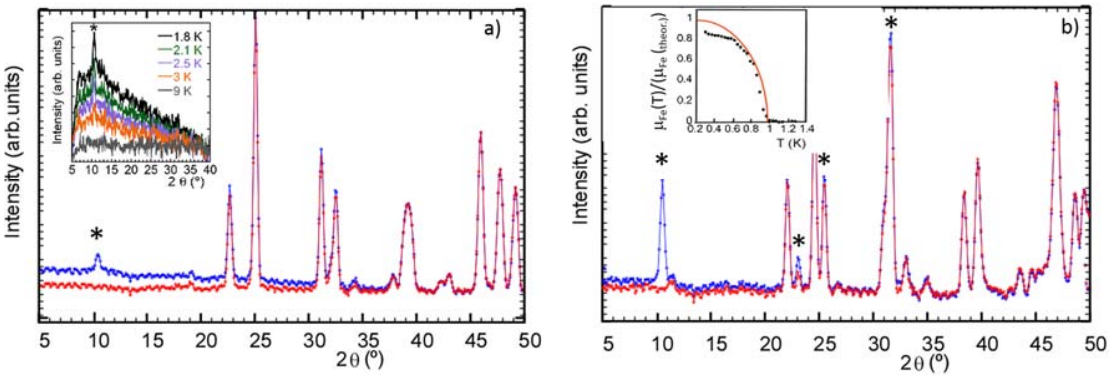

Figure 6. The neutron diffraction profiles of phase **I-a** (a) and **I-b** (b) at 10 (red) and 1.8 K (blue) obtained in D1B. The (*) dots show the magnetic contributions. [left inset (a)] Temperature dependence of the difference diagrams of D1B patterns between 1.8 and 9 K which have been obtained subtracting the nuclear contribution (pattern at 10 K). [Right inset (b)] The temperature dependence of the normalized Fe magnetic moment (calculated from $\mu_{Fe}(T)/\mu_{Fe}$, the μ_{Fe} being the theoretical value of ca. 5 μ_B) obtained from the fit of the neutron diffraction pattern and the expected theoretical dependence for the Brillouin function with S = 5/2 (red line).

On the other hand, the comparison of the paramagnetic pattern (10 K) and the magnetically ordered (1.8 K) [Figure 6 (b)] of phase **I-b** reveals the occurrence of several well defined magnetic peaks. The temperature evolution of the neutron diffraction pattern places the onset of a magnetic ordering around T_N=5.5 K. Moreover, the diffuse scattering almost disappears, showing a significant difference between the **I-a** and **I-b** phases. Focusing on the magnetic structure of phase **I-b** (phase **I-a** does not show enough magnetic peaks to propose a realistic magnetic model), below T_N, the magnetic reflections can be indexed with the propagation vector **k** = (0, 0, 0), indicating that the magnetic and nuclear unit cells are the same. Details of the magnetic structure calculation using Bertaut's symmetry analysis method [44] are described in supplementary material and in Table S7.

The magnetic model obtained matches to ferromagnetic layers extended into the *ac*-plane, which are antiferromagnetically coupled along the *b*-axis with a possible canting that would produce a global ferromagnetic behavior. According to magnetometry data, the occurrence of a canting is discarded. Moreover, Mössbauer data display six-peak in the patterns below Néel temperature which are not symmetrical (two magnetic hyperfine splittings are necessary to fit each spectrum). Therefore, the magnetic structure of phase **I-b** should have two Fe^{3+} magnetic sublattices with different magnetization directions relative to the crystallographic axes. Thus, the relative orientation of the magnetic moments of both symmetry related magnetic sites present in this phase were refined. The best fitting of the D1B data at 1.8 K gives for iron $Fe(1)^{3+}$ sublattice R_{tetha}= 176º(5) and for $Fe(2)^{3+}$ R_{tetha}= 140º(10) in good agreement with the Rietveld refinement of the D2B data at 2 K. The refined magnetic moment for both Fe^{3+} magnetic sublattices have been constrained to be equal, giving a refined value of 4.64(1) μ_B; lower than the expected value of 5

μ_B for Fe^{3+} in high-spin configuration due to the fact that the spin density is not strictly localized on the iron ions, but is partially delocalized onto the iron environment[28] (see details in theoretical calculations). In order to avoid overparameterization and due to the negligible value obtained in the first refinements for the magnetic moment component along the *b* axis (ϕ angle, in spherical coordinates), it was kept equal to zero, giving rise to a collinear antiferromagnetic behavior which is in good agreement with the macroscopic magnetic measurements. The final refinements are shown in Figure S12 of Supplementary Material and the corresponding magnetic structure is shown in Figure 7. The nuclear and magnetic discrepancy factors are R_p = 22.6 % and 12.4 %, R_{wp} = 15.7 % and 12.1 %, R_{Bragg} = 11.9 % and 5.8 % and R_{mag} = 8.7 % and 6.8 % for D1B and D2B data respectively. Finally, sequential refinements of D1B between 1.8 and 10 K were performed using the FullProf suite[45] in order to follow the temperature dependence of the modulus of the Fe^{3+} magnetic moment, μFe. The right inset of Figure 6 (b) display this evolution with the theoretical dependence corresponding to the Brillouin type S = 5/2.[46]

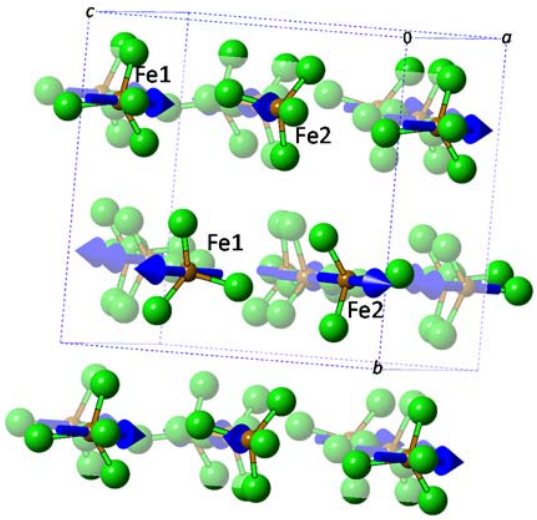

Figure 7. Magnetic structure of phase **I-b** at 1.8 K. The Dimim counterions have been omitted for the sake of clarity.

Neutron polarization analysis The same thermal process than in the previous nonpolarized neutron measurements was used for the xyz-polarization analysis experiment at D7 diffractometer. The temperature evolution of the total cross section of phase **I-a** between 1.5 and 15 K is shown in Figure 8 (up-left). The separated magnetic cross sections for the total one displays three magnetic peaks at temperatures below around 3 K. The separation works well and the statistics are good despite the very large incoherent scattering signal due to the presence of 13 H atoms in the organic part of $DimimFeCl_4$ sample. The successful separation of the magnetic contribution was confirmed checking that the sample does not have preferred orientation and hence the component of the magnetization perpendicular to the scattering vector is isotropic. After

thermal stabilization, phase **I-b** [Figure 8 (up-right)] shows the same number of magnetic reflections, in the same Q positions, but now these disappear at temperatures lower that 6 K. This result allows us to propose that both magnetic structures could be similar with stronger magnetic couplings in phase **I-b**. The first magnetic reflection located at Q = 0.47 $Å^{-1}$ at 1.5 K, displays in phase **I-b** an intensity almost twice as high as in phase **I-a**, which should be related with the modification of the super-exchange interactions after the phase transition.

At 1.5 K, the spin-incoherence of phase **I-a** increases in a monotonous way below around Q = 1.4 $Å^{-1}$ with no tendency to saturation for the lowest Q studied [Figure 8 (centre-left)]. Moreover at this Q, its intensity drops about 10% as temperature increases up to 10 K. A similar behaviour is found for the phase **I-b** but now its intensity increases less than 5% from 10 to 1.5 K. This issue confirms that the increase of background at low temperature detected with nonpolarized neutron diffraction data (D2B and D1B) has no magnetic origin (inelastic magnetic background). However, it is modified with the cooling-heating process achieving significant difference between both phases. As far as we know is the first time that this behaviour is observed in molecular-based material. Our hypothesis is that this behavior could arise from the hydrogen atoms that could produce changes in the nuclear spin-incoherence term. The presence of correlations between neighboring atoms (short range order) is discarded since this would produce smooth fluctuations in intensity across a wide range of Q-space.[47] Therefore quasielastic neutron scattering (QENS) and inelastic neutron scattering (INS) data will be obtained to give us more detail about this unusual behavior.

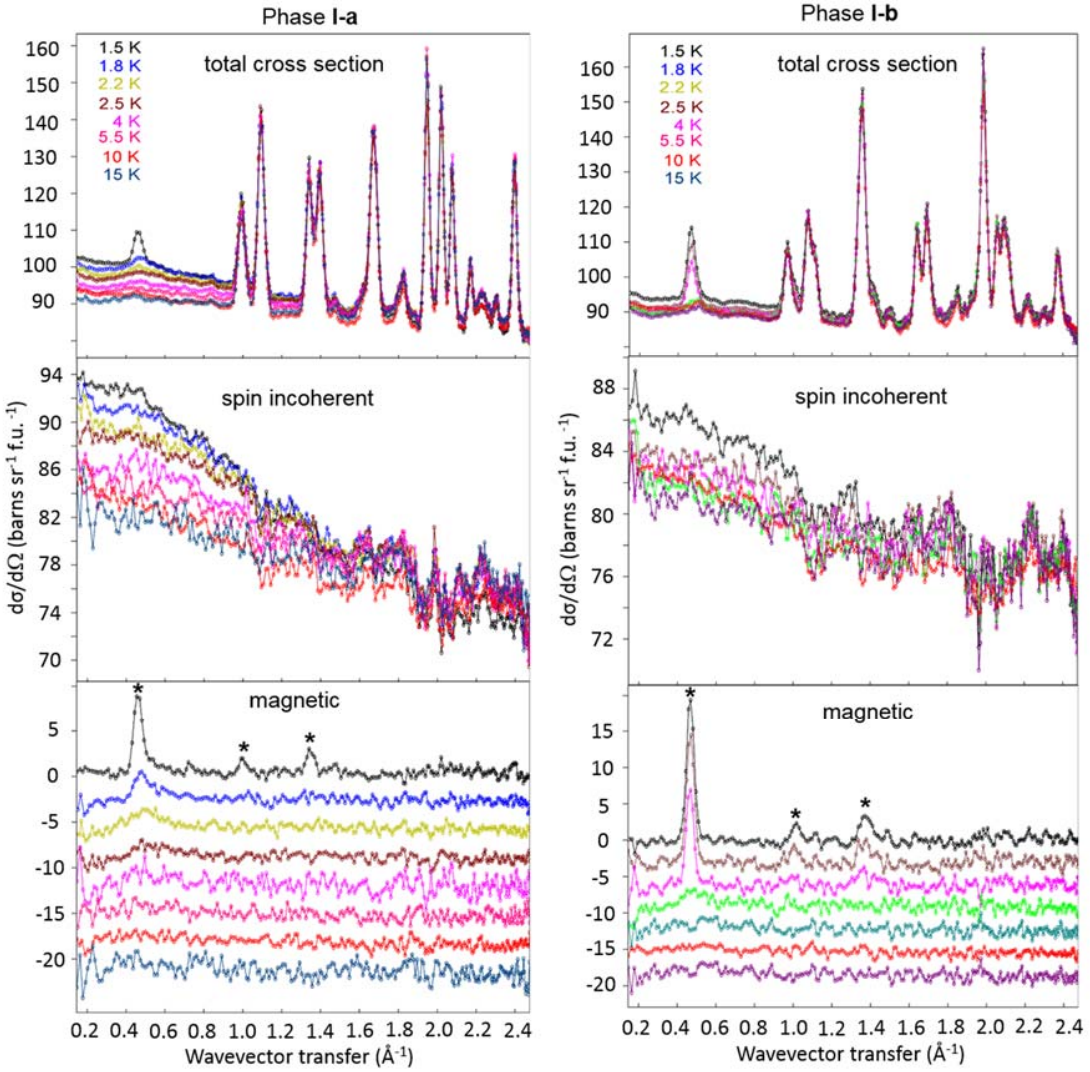

Figure. 8. Separation of nuclear and spin incoherent magnetic (The patterns have been shifted 2 barns sr^{-1} $f.u.^{-1}$ for clarity) from the total neutron scattering cross sections of phase **I-a** (left) phase **I-b** (right) measured using XYZ-polarization analysis on D7 at several temperatures between 1.5 and 15 K. The (*) dots show the magnetic peaks.

Density functional theory calculations. The crystal and magnetic structure of phase **I-a** and **I-b** were also investigated by ab initio calculations. Density functional theory (DFT), introduced within the SIESTA[48] code, was employed as it offers an efficient and accurate quantum mechanical method to optimize crystal structures, to calculate the equilibrium energies, to obtain the charge distributions and to predict van der Waals (vdW) interactions in the DFT context. It was used with a formalism to deal with vdW interactions, which have been successfully applied to the study of ILs[49].

We carried out a structural relaxation of phase **I-a**[28] and **I-b** to refine the atomic coordinates starting from the experimental coordinates obtained by the D2B Rietveld analysis at 10 K (Table S.8). The intramolecular geometries (reduced coordinates) and distances between $[Dimim]^+$

cation and $[FeCl_4]^-$ anion gained by DFT are not too far away from the starting point, with only an overestimation below of 3% relative to the experimental data, within the standard deviations of the functional approach.[50] In one hand, we obtain that the E_0 of phase **I-b**, which represents the energy per atom of the compound under investigation in its ground state, i.e., at 0 K and without external stress is 37 meV/84 atoms more stable than the phase **I-a**. Therefore, we confirm that after the solid-to-solid transition the crystal structure (**I-b**) is more stable. On the other hand, we check the existence of attractive anion-π interactions[51] using the projected density of states (PDOS) of the imidazolium with the chloride of the metal complex anion (see Figure S13 of supplementary material). Figure 9 displays how the wave function can connect Fe(1) and Fe(2) atoms from layer to layer across the π orbital of the imidazolium ring. Thus, an electronic transmitting mechanism can be propagated via anion-π interactions, the anion residing above the ring centroid, which is characteristic of strong anion-π interactions.[52]

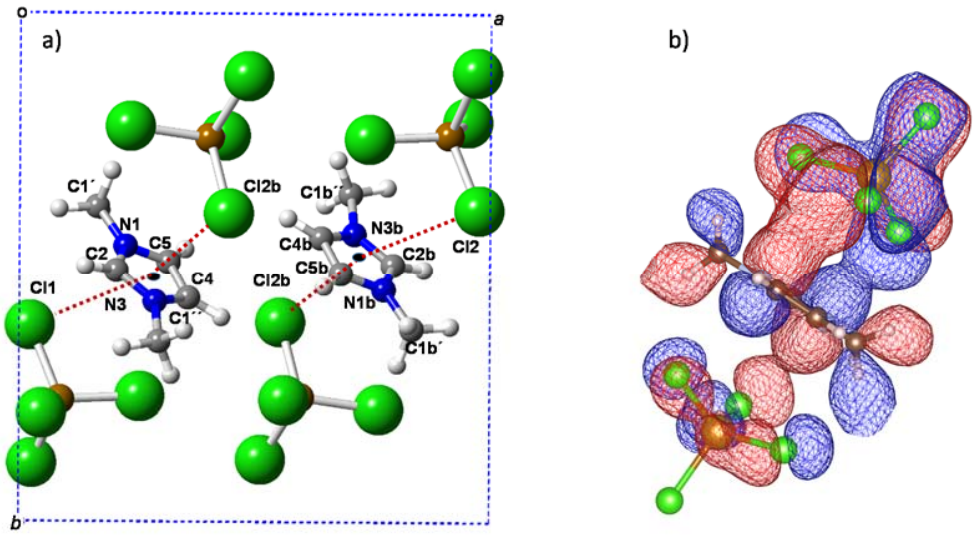

Figure 9 (a). Shorter π−d interaction distances between the metal complex and imidazolium centroid. Relevant distances and orientations are display in Table 2 which show potential anion–π interactions between on imidazolium and tetrachlorideferrate ions in phase **I-b** according IUPAC recommendation. **(b):** Representation of the wave function for the state with energy of −2.34 eV below the Fermi energy, where there is orbital overlapping (red and blue colors represent the positive and negative part, respectively).

We checked the stability of the proposed antiferromagnetic structure of phase **I-b** with respect to the other three possible magnetic configurations allowed in this space group. The calculations display the lowest energy for this configuration, in good agreement with the result obtained by the neutron experimental data. The sum of the Mulliken populations obtained gives a value of 4.98 μ_B, which is expected for a Fe^{+3} with a high spin of S=5/2.[28] The quantity of spin transferred to one chloride atoms is 0.26 μ_B, the total transfer being 1.04 μ_B, which represents about 21 % of

the magnetic moment. These numbers are consistent with a direct integration of the charge density over spheres surrounding atoms, assuming non-overlapping spheres around Fe and Cl of 2.4 Bohr. Comparing the present result with that obtained for phase **I-a** , we obtain that the delocalization is similar (total spin density transfer from Fe to Cl = 1.06 μ_B),[28] being also in good agreement with the data reported in other Fe^{+3} materials.[53]

Magneto structural correlations. For the magneto-structural discussion, the crystal structure at 10 K (high resolution NPD) will be taken due to the better determination of atomic positions near of the magnetic ordering. A comparative of the most relevant interatomic distances of phases **I-a** and **I-b** is displayed in Table 1 and 2. The data obtained from SXPD are shown in Table S9.

Seeing the structural features of both phases, direct Fe···Fe interactions are not present due to the shorter Fe···Fe distances through the space range between 6.16 and 8.16 Å (see Table 2). Therefore, direct super-exchange anion−anion interactions (Fe−Cl···Cl−Fe) transmit magnetic couplings between an iron ion and its first shell of neighbouring iron ions. In addition, phase **I-b**, in agreement with the DFT calculations should also display indirect super-exchange anion−anion interactions through anion-π interactions (Fe−Cl···Im···Cl− Fe), where Im represents an imidazolium donor cation (see Table 1).

Figure 10 displays a comparative scheme of the possible super-exchange anion−anion interactions projected on the *ac*-plane on both phases, **I-a** and **I-b**, according to the most appropriate model of the magnetic structure obtained from neutron diffraction data. The strength of these super-exchange anion−anion interactions of both phases, (Fe−Cl···Cl−Fe), can be qualitatively compared according to the issue that shorter Cl···Cl distances, larger Fe−Cl···Cl angles, and torsion angles near 0 and 180° are correlated with stronger magnetic exchange constants.[54] Two intraplane interactions, $J_{\perp}$, defined by J_1 and J_2, connect the iron atoms in linear chains in the *ac*-plane on both phases. In one hand, the magnetic couplings of phase **I-a** show a Cl···Cl distances of 3.603 and 3.564 Å for J_1 and J_2. These are smaller than the sum of the vdW radii of two chloride atoms (3.70 Å), showing remarkable agreement with other reported magnetic coupling lengths in several metal−organic materials.[55] For the phase **I-b**, some of these contacts are longer, range from 3.601 to 4.064 Å. In the other hand, the four ligand atoms involved in these magnetic pathways for phase **I-a** display a mixture of super-exchange angles: (i) Fe−Cl···Cl, with 157.1 and 158.5° and (ii) Cl···Cl−Fe, with 87.8 to 95.8° and τ of 155.2 and 171.3° for J_1 and J_2, respectively. These parameters are nearly maintained after the phase transition to phase **I-b** where Fe−Cl···Cl, range between 130.3 and 164.4° and Cl···Cl−Fe, vary from 82.8 to 164.4° with τ from 149.8 to 179.3°. According to the magnetic structure obtained, these types of magnetic coupling should present a ferromagnetic behaviour.

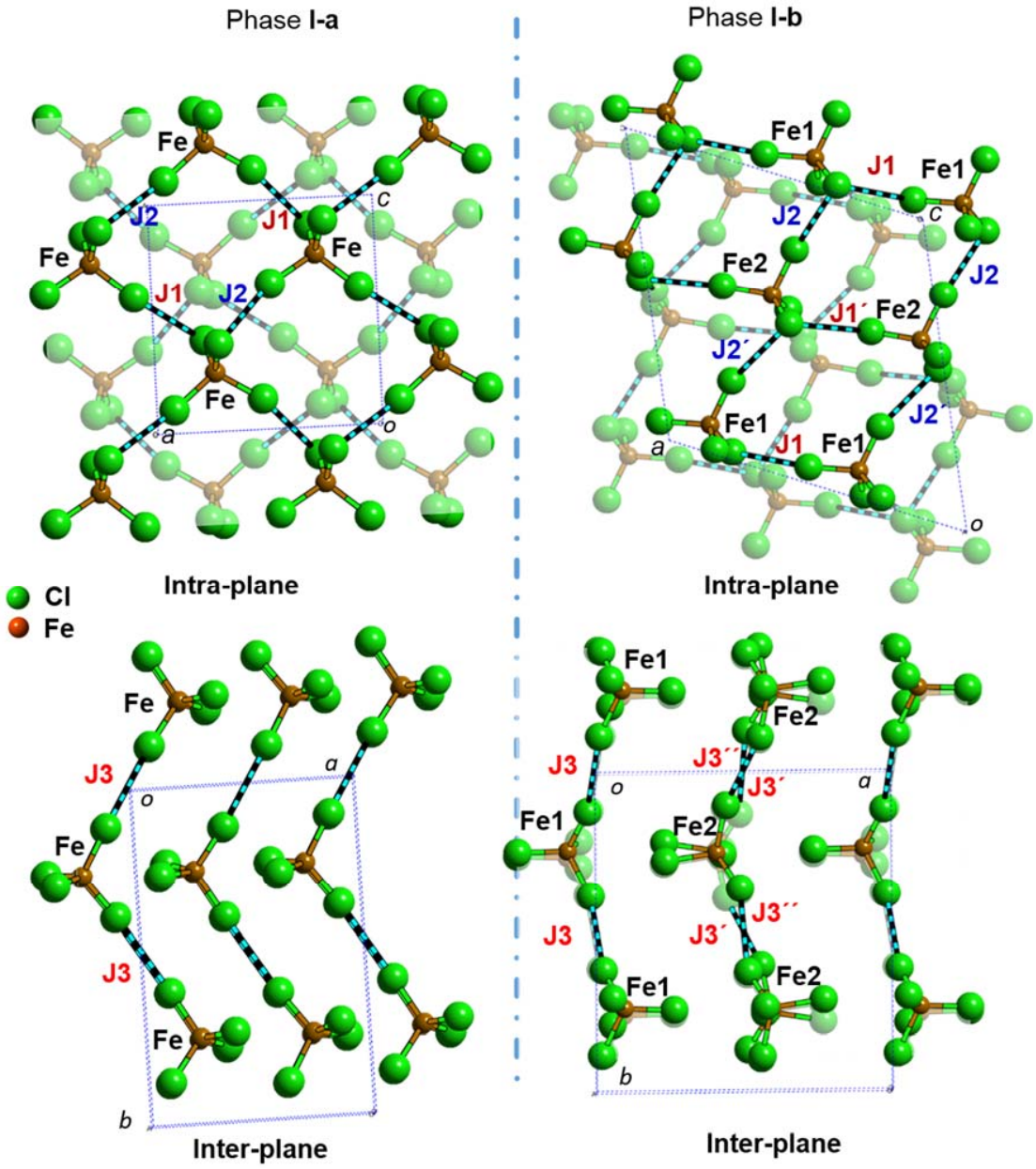

Figure 10. Schematic view of the possible intra and inter-plane magnetic exchange pathways for phase **I-a** and **I-b** via Fe−Cl···Cl−Fe bridge

The J_3 interaction, $J_\perp$ or interplane super-exchange magnetic coupling, gives rise to zigzag chains to set up a ladder structure that goes parallel to the *b* direction [Figure 10]. This is the strongest coupling, according to the predominant antiferromagnetic behaviour of both phases. On one hand, phase **I-a** display a Cl···Cl distance of 3.77 Å. After the solid-transition, this length decreases varying from 3.435 to 3.77 Å depending which iron metal complexes are connected [Fe(1) or Fe(2)] [see right picture of Figure 10 (b)]. On the other hand, J_3 of phase **I-a** shows Fe−Cl···Cl and Cl···Cl−Fe angles of 170.6 and 173.5° with τ of 14.35° while in phase **I-b**, Fe−Cl···Cl ranges from 148.0 to 156.5° and Cl···Cl−Fe, vary between 148 to 165.5° with τ from 120.5 to 180.0°.

The analysis of these parameters unravels the reason why the strength of these super-exchange anion−anion interactions (Fe−Cl···Cl−Fe) can be stronger within phase **I-b**. The main factor should be attributed to shorter Cl···Cl distances which are correlated with stronger magnetic exchange constants. Moreover, it should be taken in consideration that phase **I-b** could also have indirect super-exchange antiferromagnetic interaction through anion-π pathway (Fe−Cl···Im···Cl− Fe) between adjacent planes.

Conclusions

In the present work we have shown how the application of thermal treatment can induce a solid-to-solid phase transition. The solid phase of Dimim$FeCl_4$, after a thermal quenching, (**I-a** phase) crystallizes in the orthorhombic structure with a three-dimensional antiferromagnetic ordering below 3 K. After a thermal treatment,, a crystal structure transformation to a monoclinic phase take place, involving a translational and reorientational process of the Dimim counterions and $[FeCl_4]^-$ anions. This feature is connected with the modification of the super-exchange pathways after the solid-to-solid phase transition which increases the magnetic long-range order temperature, T_N from below around 3 to 5.4 K. The magnetic structure formed can be described as antiferromagnetic layers pillared along the *b*-axis. Using polarized neutron diffraction we have studied the origin of the increase of the background detected below 9 K for both phases. The results unambiguously show that this signal has no magnetic origin and therefore should be related with structural features probably due to the hydrogen atoms.

As stated above, cooling rate could be a very important variable for the dynamical process, structural transformations and magnetic properties of MILs. This observation could pave the way towards novel stimuli-responsive materials by temperature effect. Similar trends are expected in ILs in which bulky cations exhibit a strong electrostatic coupling with small anions, such as halides.

ASSOCIATED CONTENT

*Supporting Information

Supporing information contains Experimental details of high-resolution synchrotron X-ray diffraction, Neutron non-polarization and polarization diffraction experiments, magnetic and Mössbauer measurements, Muon spin relaxation (μSR) spectroscopy data, DFT calculations with computational details and crystallographic information (CIF data).

This material is available free of charge via the Internet at http://pubs.acs.org.

ACKNOWLEDGMENTS

Financial support from the Spanish Ministerio de Ciencia e Innovación (Project MAT2014-55049-R, MAT2014-5611-2-R, and FC-15-GRUPIN14-037), the Romanian UEFISCDI (Project PN-II-ID-PCE-2011-3-0583 (85/2011) and Becas Iberoamericas Jóvenes Profesores Investigadores, 2011, Santander Universidades is acknowledged. The authors also gratefully acknowledge the computer resources, technical expertise, and assistance provided by the Red Española de Supercomputación. The paper is (partly) based on the results of experiments carried out at Paul Scherrer Institut, Villigen, Switzerland, ALBA synchrotron light source in Barcelona and Institute Laue-Langevin (ILL) of Grenoble.

REFERENCES

(1)Giernoth, R. *Angewandte Chemie International Edition* **2010**, *49*, 2834.
(2)Bates, E. D.; Mayton, R. D.; Ntai, I.; Davis, J. H. *Journal of the American Chemical Society* **2002**, *124*, 926.
(3)Lee, S.-g. *Chemical Communications* **2006**, 1049.
(4)Zhang, Z.; Xie, Y.; Li, W.; Hu, S.; Song, J.; Jiang, T.; Han, B. *Angewandte Chemie International Edition* **2008**, *47*, 1127.
(5)Tang, S.; Baker, G. A.; Zhao, H. *Chemical Society Reviews* **2012**, *41*, 4030.
(6)Lewandowski, A.; Świderska-Mocek, A. *Journal of Power Sources* **2009**, *194*, 601.
(7)Xu, K. *Chemical reviews* **2004**, *104*, 4303.
(8)Simon, P.; Gogotsi, Y. *Nature materials* **2008**, *7*, 845.
(9)Lin, M.-C.; Gong, M.; Lu, B.; Wu, Y.; Wang, D.-Y.; Guan, M.; Angell, M.; Chen, C.; Yang, J.; Hwang, B.-J. *Nature* **2015**.
(10)Huang, X.; Margulis, C. J.; Li, Y.; Berne, B. J. *Journal of the American Chemical Society* **2005**, *127*, 17842.
(11)Gurkan, B. E.; de la Fuente, J. C.; Mindrup, E. M.; Ficke, L. E.; Goodrich, B. F.; Price, E. A.; Schneider, W. F.; Brennecke, J. F. *Journal of the American Chemical Society* **2010**, *132*, 2116.
(12)Swatloski, R. P.; Spear, S. K.; Holbrey, J. D.; Rogers, R. D. *Journal of the American Chemical Society* **2002**, *124*, 4974.
(13)Socha, A. M.; Parthasarathi, R.; Shi, J.; Pattathil, S.; Whyte, D.; Bergeron, M.; George, A.; Tran, K.; Stavila, V.; Venkatachalam, S. *Proceedings of the National Academy of Sciences* **2014**, *111*, E3587.
(14)Branco, A.; Branco, L. C.; Pina, F. *Chemical Communications* **2011**, *47*, 2300.
(15)Scovazzo, P.; Portugal, C. A. M.; Rosatella, A. A.; Afonso, C. A. M.; Crespo, J. G. *Journal of Colloid and Interface Science* **2014**, *428*, 16.
(16)Brown, P.; Bushmelev, A.; Butts, C. P.; Cheng, J.; Eastoe, J.; Grillo, I.; Heenan, R. K.; Schmidt, A. M. *Angewandte Chemie International Edition* **2012**, *51*, 2414.
(17)Hayes, R.; Warr, G. G.; Atkin, R. *Chemical reviews* **2015**, *115*, 6357.
(18)Urahata, S. M.; Ribeiro, M. C. *The Journal of chemical physics* **2004**, *120*, 1855.
(19)Triolo, A.; Russina, O.; Bleif, H.-J.; Di Cola, E. *The Journal of Physical Chemistry B* **2007**, *111*, 4641.
(20)Bodo, E.; Gontrani, L.; Caminiti, R.; Plechkova, N. V.; Seddon, K. R.; Triolo, A. *The Journal of Physical Chemistry B* **2010**, *114*, 16398.
(21)García-Saiz, A.; de Pedro, I.; Vallcorba, O.; Migowski, P.; Hernández, I.; Barquin, L. F.; Abrahams, I.; Motevalli, M.; Dupont, J.; Gonzalez, J. A., Rodríguez Fernández, J. *RSC Advances* **2015**, *5*, 60835.

(22) Garcia-Saiz, A.; de Pedro, I.; Migowski, P.; Vallcorba, O.; Junquera, J.; Blanco, J. A.; Fabelo, O.; Sheptyakov, D.; Waerenborgh, J. C.; Fernandez-Diaz, M. T.; Rius, J.; Dupont, J.; Gonzalez, J. A.; Fernandez, J. R. *Inorg Chem* **2014**, *53*, 8384.
(23) Bernardes, C. E. S.; Mochida, T.; Canongia Lopes, J. N. *Physical Chemistry Chemical Physics* **2015**, *17*, 10200.
(24) Harada, J.; Ohtani, M.; Takahashi, Y.; Inabe, T. *Journal of the American Chemical Society* **2015**, *137*, 4477.
(25) Abendroth, J. M.; Bushuyev, O. S.; Weiss, P. S.; Barrett, C. J. *ACS nano* **2015**, *9*, 7746.
(26) Zhang, X.; Shao, X.-D.; Li, S.-C.; Cai, Y.; Yao, Y.-F.; Xiong, R.-G.; Zhang, W. *Chemical Communications* **2015**, *51*, 4568.
(27) Sun, Z.; Chen, T.; Luo, J.; Hong, M. *Angewandte Chemie International Edition* **2012**, *51*, 3871.
(28) García-Saiz, A.; Migowski, P.; Vallcorba, O.; Junquera, J.; Blanco, J. A.; González, J. A.; Fernández-Díaz, M. T.; Rius, J.; Dupont, J.; Rodríguez Fernández, J.; de Pedro, I. *Chemistry – A European Journal* **2014**, *20*, 72.
(29) de Pedro, I.; García-Saiz, A.; Dupont, J.; Migowski, P.; Vallcorba, O.; Junquera, J.; Rius, J.; Rodríguez Fernández, J. *Crystal Growth & Design* **2015**, *15*, 5207.
(30) Zhong, C.; Sasaki, T.; Jimbo-Kobayashi, A.; Fujiwara, E.; Kobayashi, A.; Tada, M.; Iwasawa, Y. *Bulletin of the Chemical Society of Japan* **2007**, *80*, 2365.
(31) Bäcker, T.; Breunig, O.; Valldor, M.; Merz, K.; Vasylyeva, V.; Mudring, A.-V. *Crystal Growth & Design* **2011**, *11*, 2564.
(32) Boca, R. *A Handbook of Magnetochemical Formulae*; Elsevier, 2012.
(33) Zora, J. A.; Seddon, K. R.; Hitchcock, P. B.; Lowe, C. B.; Shum, D. P.; Carlin, R. L. *Inorganic Chemistry* **1990**, *29*, 3302.
(34) de Pedro, I.; Garcia Saiz, A.; Gonzalez, J. A.; Ruiz de Larramendi, I.; Rojo, T.; Afonso, C.; Simeonov, S.P.; Waerenborgh, J. C.; Blanco, J. A.; Ramajo, B.; Rodriguez Fernandez, J. *Physical Chemistry Chemical Physics* **2013,** *15*, 12724.
(35) de Pedro, I.; Rojas, D. P.; Albo, J.; Luis, P.; Irabien, A.; Blanco, J. A.; Rodriguez Fernandez, J. *Journal of Physics-Condensed Matter* **2010**, *22,* 296006.
(36) de Pedro, I.; Rojas, D. P.; Blanco, J. A.; Rodriguez Fernandez, J. *Journal of Magnetism and Magnetic Materials* **2011**, *323*, 1254.
(37) Briers, J.; Eevers, W.; De Wit, M.; Geise, H. J.; Wauters, J.; Van Bavel, M.; Bemelmans, H.; Langouche, G. *The Journal of Physical Chemistry* **1995**, *99*, 12971.
(38) Waerenborgh, J. C.; Rabaça, S.; Almeida, M.; Lopes, E. B.; Kobayashi, A.; Zhou, B.; Brooks, J. S. *Physical Review B* **2010**, *81*, 060413.
(39) Greenwood, N. N.; Gibb, T. C. *Mössbauer spectroscopy*; Chapman and Hall London, 1971.
(40) Hayano, R.; Uemura, Y.; Imazato, J.; Nishida, N.; Yamazaki, T.; Kubo, R. *Physical Review B* **1979**, *20*, 850.
(41) Petrenko, O. A.; Ritter, C.; Yethiraj, M.; McK Paul, D. *Physical Review Letters* **1998**, *80*, 4570.
(42) Greedan, J. E.; Wiebe, C. R.; Wills, A. S.; Stewart, J. R. *Physical Review B* **2002**, *65*, 184424.
(43) Stewart, J.; Deen, P.; Andersen, K.; Schober, H.; Barthélémy, J.-F.; Hillier, J.; Murani, A.; Hayes, T.; Lindenau, B. *Journal of Applied Crystallography* **2009**, *42*, 69.
(44) Bertaut, E. *Acta Crystallographica Section A* **1968**, *24*, 217.
(45) Rodríguez-Carvajal, J. *J. Appl. Crystallogr. 14 (1981) 149*.
(46) Blanco, J. A.; Espeso, J. I.; García Soldevilla, J.; Gómez Sal, J. C.; Ibarra, M. R.; Marquina, C.; Fischer, H. E. *Physical Review B* **1999**, *59*, 512.
(47) De Vries, M.; Stewart, J.; Deen, P.; Piatek, J.; Nilsen, G.; Rønnow, H.; Harrison, A. *Physical review letters* **2009**, *103*, 237201.
(48) Soler, J. M.; Artacho, E.; Gale, J. D.; García, A.; Junquera, J.; Ordejón, P.; Sánchez-Portal, D. *Journal of Physics Condensed Matter* **2002**, *14*, 2745.
(49) Del Pópolo, M. G.; Lynden-Bell, R. M.; Kohanoff, J. *The Journal of Physical Chemistry B* **2005**, *109*, 5895.
(50) Dion, M.; Rydberg, H.; Schröder, E.; Langreth, D. C.; Lundqvist, B. I. *Physical Review Letters* **2004**, *92*, 246401.

(51) Schottel, B. L.; Chifotides, H. T.; Dunbar, K. R. *Chemical Society Reviews* **2008**, *37*, 68.
(52) Salonen, L. M.; Ellermann, M.; Diederich, F. *Angewandte Chemie International Edition* **2011**, *50*, 4808.
(53) Campo, J.; Luzón, J.; Palacio, F.; McIntyre, G. J.; Millán, A.; Wildes, A. R. *Physical Review B* **2008**, *78*, 054415.
(54) Bertani, R.; Sgarbossa, P.; Venzo, A.; Lelj, F.; Amati, M.; Resnati, G.; Pilati, T.; Metrangolo, P.; Terraneo, G. *Coordination Chemistry Reviews* **2010**, *254*, 677.
(55) Turnbull, M. M.; Landee, C. P.; Wells, B. M. *Coordination Chemistry Reviews* **2005**, *249*, 2567.

Table 1. Interatomic distances between the imidazolium and the metal complex anion in the crystal structures of phases **I-a** and **I-b** at 10 K obtained from Rietveld refinements of high resolution neutron powder diffraction data.

$[FeCl]^{-}\cdots[Dimim]^{+}$ (potential π-d interactions)		
Phase **I-a**		
	length (Å)	angle (º)
Fe1-Cl1··centroid1	3.904(8)	81.5(3)
Fe1-Cl3··centroid1	3.907(9)	80.7(3)
Phase **I-b**		
Fe1-Cl2··centroid1	3.88(2)	81.6(7)
Fe1-Cl1··centroid2	3.61(2)	89.9(8)
Fe2-Cl2b··centroid1	3.56(2)	88.6(8)
Fe2-Cl2b··centroid2	3.67(2)	93.1(8)

Table 2. Selected geometrical parameters, bond lengths (Å) and angles (deg) obtained from high-resolution neutron diffraction (experiment at 10 K) related to the possible magnetic exchange pathways for phase **I-a** and **I-b**.

	Intra-plane						
	Magnetic exchange Pathways	**Direct distance Fe-Fe/Å**	**Bond/Å Cl-Cl**	**Angle/° Fe-Cl-Cl**	**Angle/° Cl-Cl-Fe**	**Torsion angle (τ)/°**	**Direction**
Phase **I-a**	**J1**	6.623	3.603	158.50	95.82	171.32	*ac*/**F**
	J2	6.162	3.564	157.06	87.75	155.16	*ac*/**F**
Phase **I-b**	**J1 *(Fe1-Fe1)***	6.571	4.064	130.31	88.08	144.75	*ac*/**F**
	J1´ *(Fe2-Fe2)*	6.566	3.858	150.09	91.15	152.91	*ac*/**F**
	J2 *(Fe1-Fe2)*	6.270	3.601	164.42	85.81	162.43	*ac*/**F**
	J2´ *(Fe2-Fe1)*	6.336	3.914	149.99	82.80	179.30	*ac*/**F**
	Inter-plane						
	Magnetic exchange Pathways	**Direct distance Fe-Fe/Å**	**Bond/Å Cl-Cl**	**Angle/° Fe-Cl-Cl**	**Angle/° Cl-Cl-Fe**	**Torsion angle (τ)/°**	**Direction /Type**
Phase **I-a**	**J3**	8.164	3.765	170.6	173.5	14.35	*b*/**AF**
Phase **I-b**	**J3 *(Fe1-Fe1)***	8.092	3.767	156.22	164.51	120.45	*b*/**AF**
	J3´ *(Fe2-Fe2)*	7.843	3.435	166.48	165.48	180.00	*b*/**AF**
	J3´´ *(Fe2-Fe2)*	7.581	3.630	147.97	147.96	180.00	*b*/**AF**

TOC

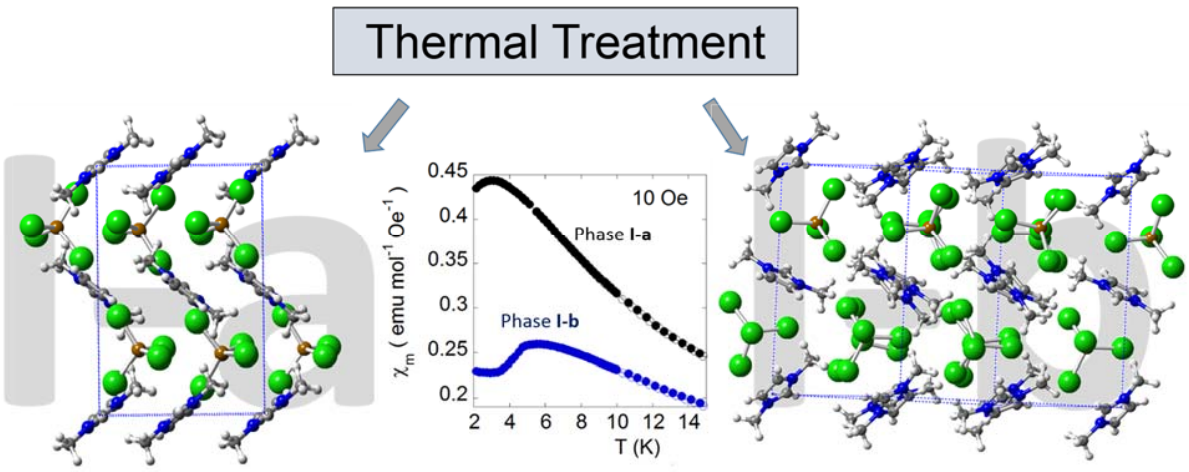

ELECTRONIC SUPLEMENTARY MATERIAL

Slow Dynamically Solid-to-Solid Phase Transition Induced by Thermal Treatment on DimimFeCl4 Magnetic Ionic Liquid

Abel García-Saiz[†]*, Imanol de Pedro[†], Oriol Vallcorba[¥], Oscar Fabelo[Ψ], Javier Junquera[†], Jesús Angel Blanco[Ж], João Carlos Waerenborgh[Л], D. Andreica[¥], Andrew Wildes[Ψ], María Teresa Fernández-Díaz[Ψ], and Jesús Rodríguez Fernández[†]

[†] CITIMAC, Facultad de Ciencias, Universidad de Cantabria, 39005 Santander.
[¥] ALBA Synchrotron Light Source, Cerdanyola del Vallés, Barcelona, Spain.
[Ψ] Institut Laue-Langevin, BP 156X, F-38042 Grenoble Cedex, France.
[Ж]Departamento de Física, Universidad de Oviedo, 33007 Oviedo, Spain.
[Л] Centro de Ciências e Tecnologias Nucleares, Instituto Superior Técnico, Universidade de Lisboa, 2695-066 Bobadela LRS, Portugal
[¥] Faculty of Physics, Babes-Bolyai University, 400084 Cluj-Napoca, Romania

Corresponding author: depedrovm@unican.es

ELECTRONIC SUPLEMENTARY MATERIAL

Table of Contents

Synthesis and Experimental Methods ……..……..…..S5

Supplementary Figure S1. SXRD thermodiffractogram of Dimim[$FeCl]_4$ heating from 100 to 300 K after a thermal quenching using a cryo-stream device and cooling between 300 and 100 K at 3 K /min……...…….……. S7

Supplementary Figure S2. Neutron diffractograms collected at D1B diffractometer at 220 K in function of time……..……..S7

Powder data solution and refinement:..... S8

Supplementary Figure S3. Observed (red points) and calculated (blue solid line) SXPD patterns for phase I-b at 220 K. Positions of the Bragg reflections are represented by vertical bars. The observed-calculated difference patterns are depicted at the bottom of each figure…….……..S8

Magnetometry measurements……..……S9

Supplementary Figure S4. Low temperature ZFC magnetic susceptibility for phase I-a and I-b at different fields from 1 to 50 kOe. The inset o figure b shows the evolution of Néel temperature (T_N) with the applied magnetic field……...……... S9

Supplementary Figure S5. Temperature dependence of the real (χ') and imaginary (χ'') components of the ac magnetic susceptibility for phase **I-a** and **I-b** measured under an ac field hac = 1 Oe and frequencies from 1 to 100 Hz for phase **I-a** and **I-b**…….S10

Supplementary Figure S6. (a) Temperature dependence of (2ε) and (b) B_{hf} for both magnetic sublattices of phase **I-b.**…….……..... S10

Muon Spin Spectroscopy detail and refinements…….……S11

Supplementary Figure S7. Examples of μ_{SR} spectra of phase **I-a** recorded at low temperatures. Lines are fits of the data using the fit function specified in the text……..……. S11

Supplementary Figure S8. Temperature dependence of the fit parameter β and λ (inset) of phase **I-a**. The line is guide to the eye. β gradually decreases down to about 0.5 at 2.07 K , while λ drastically increases from 0.25 at 5 K to 0.90 at 2.07 K ……..S11

Supplementary Figure S9. μ_{SR} spectra of phase **I-a** fitted using a combination of exponentials, as described in the text……...……..... S12

ELECTRONIC SUPLEMENTARY MATERIAL

Supplementary Figure S10. Temperature dependence of λ_1 and λ_2 of phase **I-a**. The lines are guide to the eye……..……..……..S12

Supplementary Figure S11.a) Magnetic transition is in-between 4.9 and 5.23 K of phase **I-b**. b) μSR spectra recorded below 4.90 K. c) The temperature dependence of the fitted frequencies……..…….S13

Details of Magnetic structure determination……S14

Supplementary Figure S12. D2B and D1B neutron diffraction data of phase **I-a** at 2 and 1.8 K, respectively. Positions of the Bragg reflections for the nuclear (first row) and magnetic (second row) structures are presented. The difference curves are plotted at the bottom……..…….S14

DFT calculations of anion-π interaction in phase I-b…..... S15

Supplementary Figure S13: PDOS of bromines from a $[FeCl_4]^-$ ion (black marks) with the atoms in the imidazolium ring (color lines). Dashed line shows the state with energy of −2.34 eV below the Fermi energy, where there is orbital overlapping……..……..……S15

Supplementary Table S1. Crystallographic data and structure refinement details for $DiminFeCl_4$ from SXPD data at 300 K (phase **II**), 100 K (phase **I-a**) and 220 K (phase **I-b**)……..….S16

Supplementary Table S2. Crystallographic data and structure refinement details for $DiminFeCl_4$ from high resolution NPD data at 10 K for phase **I-a** and phase **I-b**.……..…..... S17

Supplementary Table S3. Final refined positional coordinates from SXPD and high resolution NPD pattern of Dimim[$FeCl_4$] at 300 K (phase **II**). Label of the atoms as in Figures 10.……..…….……..……..... S18

Supplementary Table S4. Final refined positional coordinates from SXPD at 100 K and high resolution NPD pattern at 10 K of Dimim[$FeCl_4$] (phase **I-a**). Label of the atoms as in Figures 10.……..…….....S19

Supplementary Table S5. Final refined positional coordinates from SXPD at 220 K and high resolution NPD at 10 K of Dimim[$FeCl_4$] (phase **I-b**). Label of the atoms as in Figures 10. …….……..... S20

Supplementary Table S6 Estimated parameters from the Mössbauer spectra of Dimim[$FeCl_4$] for phase **I-a** and **I-b** taken at different temperatures..... S21

ELECTRONIC SUPLEMENTARY MATERIAL

Supplementary Table S7. Basis vectors of the four possible irreducible representation of the space group $P2_1/c$ for k = (0, 0, 0) for the $Fe(1)^{3+}$ and $Fe(2)^{3+}$ ions located on the (0.0930, 0.7410, 0.1500) and (0.4080, 0.2550, 0.0660) positions, respectively..... S21

Supplementary Table S8. Final refined positional coordinates from DFT calculations at 0 K for phase **I-b** For the phase I-a these are included in Ref 28.....S22

Supplementary Table S9. Most Relevant Interatomic Distances in the crystal structures of phase **I-a** at 100 K, phase **II** at 300 K and phase **I-b** at 220 K obtained from Rietveld refinements of synchrotron powder diffraction data..... S23

References..... S24

ELECTRONIC SUPLEMENTARY MATERIAL

Synthesis. The synthesis of Dimim[$FeCl_4$], was performed following the method previously reported in reference 28 of the manuscript. The chemical and elemental characterization confirmed the C5N2H9Cl4Fe chemical formula. The crystal and magnetic structures were obtained by Synchrotron X-ray powder diffraction, high and low resolution neutron diffraction experiments. The physical characterization was realized using DC and AC magnetic susceptibility, magnetization, Mössbauer and muon spin relaxation measurements. Finally, density functional first-principles simulations based on a numerical atomic orbital method as implemented in the SIESTA code have been carried out.

Experimental Methods

High-resolution synchrotron X-ray diffraction (SXPD). Powder diffraction data were collected at the high resolution end station of beamline BL04 of the ALBA synchrotron using the microstrip Mythen II solid-state detector (six modules, 1280 channels/module, 50 μm/channel, sample-to-detector distance 550 mm). The wavelength used for the experiment was 0.61969 Å for all measurements except for 220 K, where a wavelength of 0.62093 Å was employed. The specimens were introduced into a 0.7 mm capillary and the temperature was controlled using an Oxford Cryostream Series 700. Sample were heated from 100 K up to 300 K and then cooled to 100 K at 5 K/min, collecting the pattern every 30 s from 2 to 45° (2θ). Longer acquisition time patterns (3 min) from 2 to 82° (2θ) were collected at 300, 220 and 100 K.

Non-polarized neutron diffraction experiments: Neutron powder diffraction measurements were performed on the D2B and D1B powder diffractometers at the Institute Laue-Langevin (ILL, Grenoble, France). About 3 g of Dimim[$FeCl_4$] were used in the experiments, this being placed in a cylindrical vanadium container and held in a liquid helium cryostat. A high-resolution powder diffractometer, D2B (λ = 1.5942 Å) was used to obtain extensive and accurate structural data at 10 and 2 K over a large angular angle $5 \leq 2\theta \leq 160^{\circ}$. High flux and medium resolution of D1B operated at λ = 2.525 Å were used to study the temperature evolution of the sample in the temperature range 2– 300 K to solve the magnetic contributions of the neutron patterns. Data from 2-10 K were collected every 0.5 K with an acquisition time of 30 min in the angular range $5 \leq 2\theta \leq 90^{\circ}$.

Polarized neutron diffraction experiments: Polarized neutron scattering experiments were carried out between 1.5 and 15 K on the diffuse scattering spectrometer D7 at the Institut Laue-Langevin (ILL). The incident wavelength and energy were 4.8 Å and the elastic Q range covered was $0.2 < Q < 2$ Å^{-1}.The total cross section was separated into magnetic, spin-incoherent, and nuclear/isotope-incoherent components using the xyz method detailed in ref 1 and 2. Data from spin-flip and non-spin-flip separations of the magnetic cross section were combined to form an average magnetic scattering cross section, $(d\sigma/d\Omega)_{mag}$. Finally, a normalization to vanadium data was performed to allow for conversion to absolute units.

Variable-temperature magnetic susceptibility measurements: Variable-temperature magnetic susceptibility measurements were performed using a standard Quantum Design MPMS magnetometer from 2 to 300 K in the $0.050 \leq H/\text{kOe} \leq 50$ range after cooling in either the presence (field cooling, FC) or the absence (zero field cooling, ZFC) of the applied field. Magnetization as a function of field (H) was measured using the same magnetometer in the $-50 \leq H/\text{kOe} \leq 50$ range at 2 and 10 K after cooling the sample in zero field. AC magnetic susceptibility measurements were carried out using the same device with an alternate excitation field (hac) of 1 Oe and frequencies from 1 to 100 Hz.

ELECTRONIC SUPLEMENTARY MATERIAL

Mössbauer mesurements: Mössbauer spectra taken in the temperature range 70 K - 1.9 K were collected in transmission mode using a conventional constant-acceleration spectrometer and a 25 mCi ^{57}Co source in a Rh matrix. The velocity scale was calibrated using α-Fe foil. Low-temperature spectra were collected using a bath cryostat with the sample immersed in liquid He for measurements between 4.0 and 1.9 K, or in He exchange gas above 4.0 K (temperature stability of 0.2 K). The spectra were fitted to Lorentzian lines using a non-linear least-squares method. Isomer shifts (Table S6) are given relative to metallic α-Fe at room temperature.

Muon spin relaxation (μSR) spectroscopy: Muon spin relaxation (μSR) experiments were performed in zero applied field at the Laboratory for Muon Spin Spectroscopy of the Paul Scherrer Institute, Switzerland using the GPS spectrometer in the temperature range 1.6–220 K. The sample was grinded and mounted in a special "cup shape" aluminum container covered with a thin layer of mylar tape to prevent leakage. Before cooling to the lowest temperature, a calibration run was recorded, in weak transverse field, at 10 K. The calibration run at 10 K offers information about the amplitude of the μSR signal and about a geometrical factor of the experiment. It is also recommended in order to ensure that of all the parts of the system are cooled down and secures a low and stable base temperature.

DFT calculations. Computational details: We have carried out density functional first-principles simulations on phase **I-a** and **I-b** based on a numerical atomic orbital method as implemented in the SIESTA[3] code. All the calculations have been performed within the efficient implementation[4] of the vdw density functional of Dion et al.[5] This fully non-local vdw correlation has been recently tested on imidazolium-based ionic liquids [6], showing spectacular improvements in the interatomic geometries, equilibrium volume and internal geometry with respect to the local density (LDA) and generalized gradient approximation (GGA) at a very modest computational cost.

Core electrons were replaced by ab-initio norm conserving pseudopotentials, generated using the Troullier-Martins scheme [7], in the Kleinman-Bylander fully non-local separable representation [8]. In order to avoid the spiky oscillations close to the nucleus we have included small partial core corrections [9] for all the atoms. The reference configuration and cutoff radii for each angular momentum shell and the matching radius between the full core charge density and the partial core charge density for the nonlinear core corrections (NLCCs) for the pseudopotentials used in this work can be found in Table S.1 of Supporting Information for H, C, N, Br and Fe.

The one-electron Kohn-Sham eigenstates were expanded on a basis of strictly localized numerical atomic orbitals [10]. We used a double-ζ plus polarization for the valence states of all the atoms. The atomic shells explicitly included in the simulations are the 1s, 2p for H; 2s, 2p, 3d for C and N; 4s, 4p, 4d for Br; and 4s, 4p, 3d for Fe. All the parameters that define the shape and range of the basis functions were obtained by a variational optimization of the enthalpy [11] (with a pressure P=0.1 GPa), using the coordinates of Dimim[$FeBr_4$] obtained by Rietveld refinement from high resolution neutron powder diffraction data as the reference configuration.

The electronic density, Hartree, and exchange correlation potentials, as well as the corresponding matrix elements between the basis orbitals, were calculated in a uniform real space grid. An equivalent plane wave cut-off of 350 Ry was used to represent the charge density. For the Brillouin zone integrations we use a Monkhorst-Pack sampling [12] of 4 × 2 × 4, equivalent to a real-space cut-off of 10 Å. [13]

Starting from the experimental coordinates obtained by high resolution neutron powder diffraction data at 10 K, a full optimization of the crystal lattice parameters and atomic positions

ELECTRONIC SUPLEMENTARY MATERIAL

was carried out, until a maximum component of the force on any atom was smaller than 0.01 eV/Å and the maximum component of the stress tensor was smaller than 0.0001 eV/$Å^3$.

The intramolecular geometries and distances of the $[Dimim]^+$ cation and $[FeCl_4]^-$ anion obtained by DFT calculations lie in the expected range comparable to those found in experimental data (overestimation within the range from 2 to 3 %). The intermolecular distances and orientations are in good agreement with the experimental results, thus confirming that the vdw functional does not introduce any unwanted features in the description of the low temperature structure. [4]

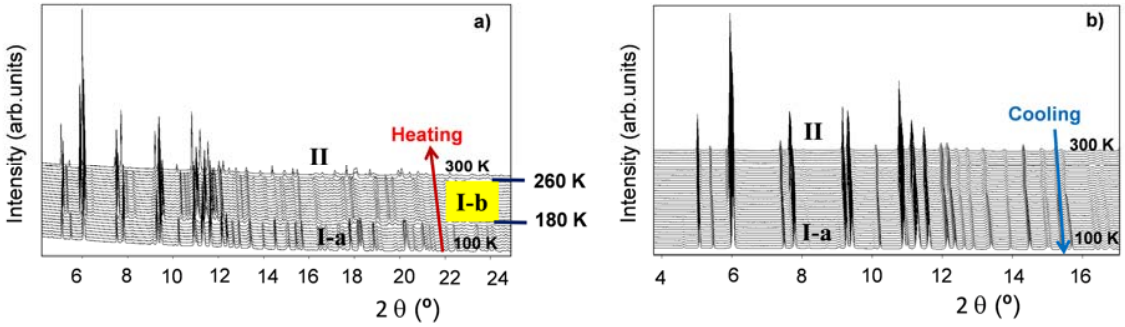

Figure S1. SXRD thermodiffractogram of Dimim[$FeCl]_4$ heating from 100 to 300 K after a thermal quenching using a cryo-stream device and cooling between 300 and 100 K at 5 K /min

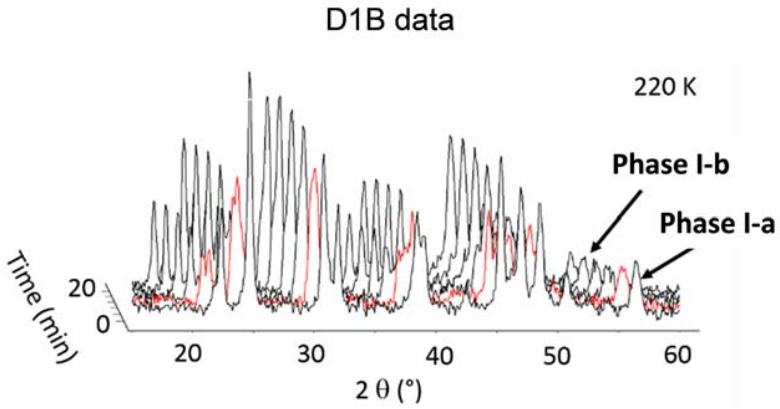

Figure S2. Neutron diffractograms collected at D1B diffractometer at 220 K in function of time. The red line show the spectra where the phase **I-a** starts to transit to phase **I-b.**

ELECTRONIC SUPLEMENTARY MATERIAL

Powder data solution and refinement. In order to determine the crystal structure of phase **I-b**, we use in a first step low temperature synchrotron powder data (ca. 220 K). The diffraction patterns collected at BL04-MSPD beamline at ALBA synchrotron (Barcelona, Spain), were indexed using DICVOL04 [14] and a whole-pattern matching and intensity extraction were performed with DAjust software.[15] The intensities were introduced in the direct-space solution program TALP[16] to obtain the candidate solution that was finally refined with the restrained Rietveld refinement program RIBOLS[17] using distance restraints taken from MOGUL.[18] For SXPD refinements, H atoms were placed in calculated positions and constrained to the respective C atoms. The Rietveld analysis was completed using a multipattern approach, combining the synchrotron data with the high resolution neutron diffraction pattern. The quality of the data allow to refine the hydrogen atoms during the last Rietveld refinement, using as starting point the hydrogen atoms coordinates of derived from Density Functional Theory (DFT) calculations.

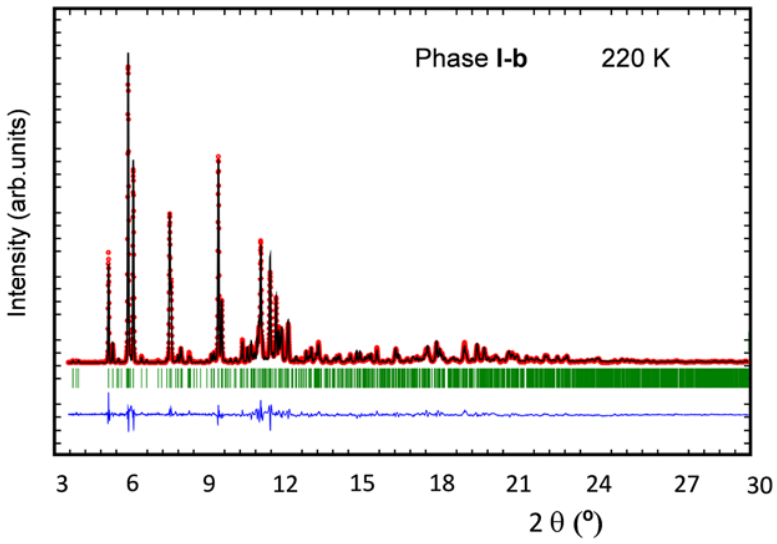

Figure S3. Observed (red points) and calculated (black solid line) SXPD patterns for phase **I-b** at 220 K. Positions of the Bragg reflections are represented by vertical bars. The observed-calculated difference patterns are depicted at the bottom of the figure.

ELECTRONIC SUPLEMENTARY MATERIAL

Magnetometry measurements. The magnetic field dependence of the maxima of both phases with the applied magnetic field was studied with another set of DC magnetic susceptibility measurements from 1 to 50 kOe, between 2 and 15 K after cooling in absence of the applied field (see Figure S4). On one hand, χ_m maxima of phase **I-a** located near of 3.1 K under 1 kOe field does not change when the magnetic field increases up to 10 kOe, disappearing for fields higher than 20 kOe. This suggests a partial overcome of the antiferromagnetic interactions present in the phase **I-a**. On the other hand, the behaviour of χ_m as a function of the external magnetic field in the phase **I-b** is slightly different, the maximum of χ_m is shifted to lower temperatures, being located at 4.15 K for an applied field of 50 kOe, suggesting that the antiferromagnetic interactions remain mainly unchanged.

The possible dynamical response of the magnetic ordering of both phases up to 2 K was checked by AC magnetic susceptibility measurements with an alternate excitation field (H_{ac}) of amplitude 1 Oe and frequencies from 1 to 100 Hz (Figure S5). The curves confirm the existence of long range order interactions and exclude the existence of a possible dynamical magnetic process up to 2 K (no-dependence of the position of magnetic peak on the frequency).[19, 20] The weak absorption in the imaginary component, χ'', in this temperature range ratifies the presence of an antiferromagnetic order, in good agreement with the results obtained above from the static magnetic susceptibility data.

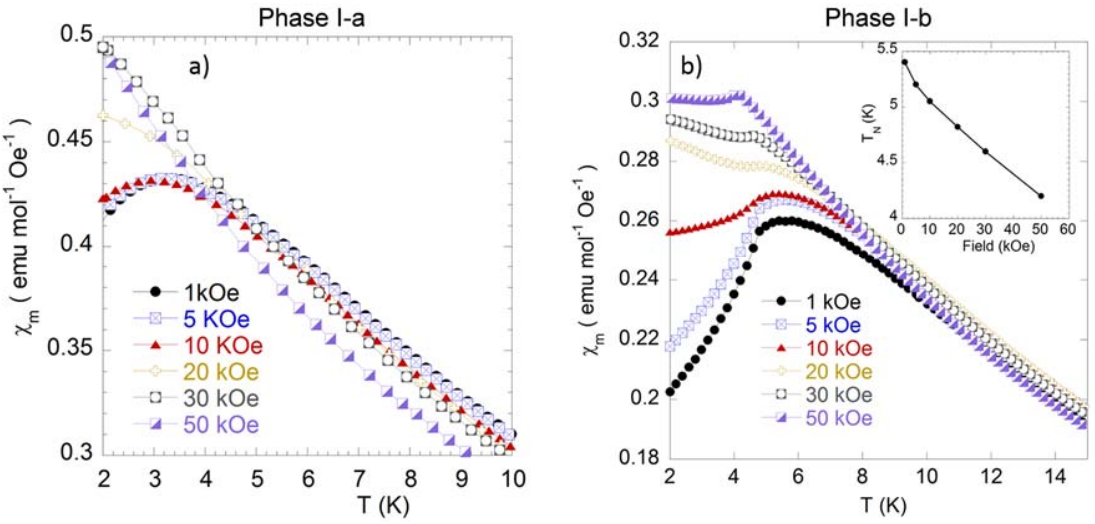

Figure S4. Low temperature ZFC magnetic susceptibility for phase **I-a** and **I-b** at different fields from 1 to 50 kOe. The inset o figure b shows the evolution of Néel temperature (T_N) with the applied magnetic field.

ELECTRONIC SUPLEMENTARY MATERIAL

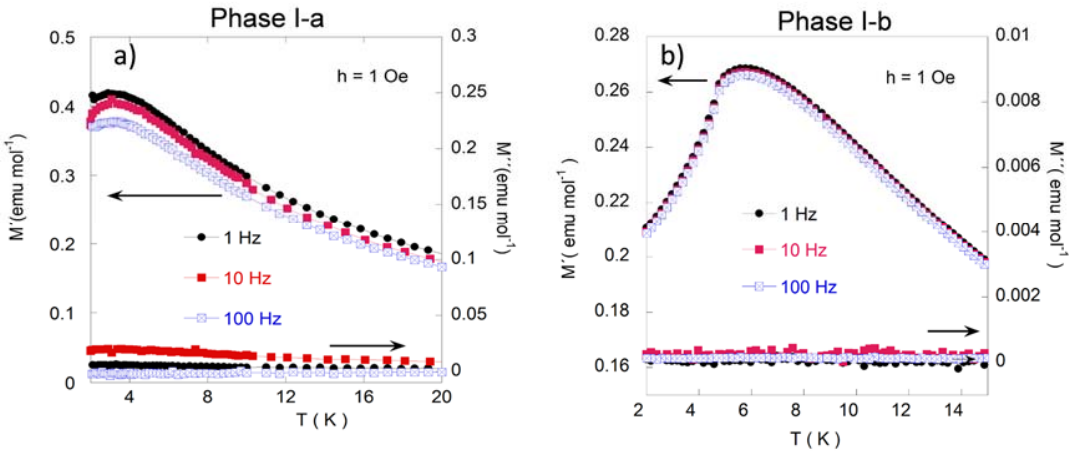

Figure S5. Temperature dependence of the real (χ') and imaginary (χ'') components of the ac magnetic susceptibility for phase **I-a** and **I-b** measured under an ac field hac = 1 Oe and frequencies from 1 to 100 Hz.

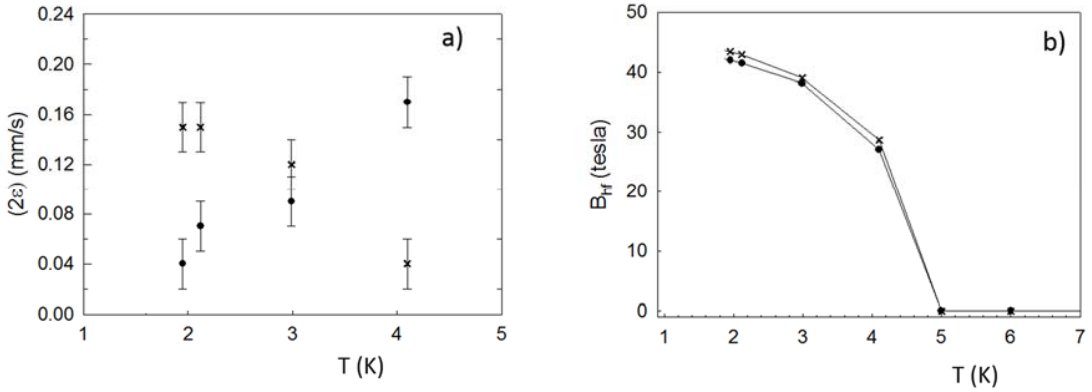

Figure S6. (a) Temperature dependence of (2ε) and (b) B_{hf} for both magnetic sublattices of phase **I-b**.

Both magnetic sextets have equal area within experimental error (Table S6), in agreement with two different Fe^{3+} magnetic sublattices. Quadrupole shifts, (2ε), are also different for each sextet which is related with occurrence of two different directions of iron magnetic moments with respect to the crystallographic axes. The temperature dependence of the (2ε) values (Table S6 Figure S6) of phase **I-b** suggest that the magnetic moment directions gradually change with temperature between T_N and 1.9 K.

ELECTRONIC SUPLEMENTARY MATERIAL

Muon Spin Spectroscopy details and refinements

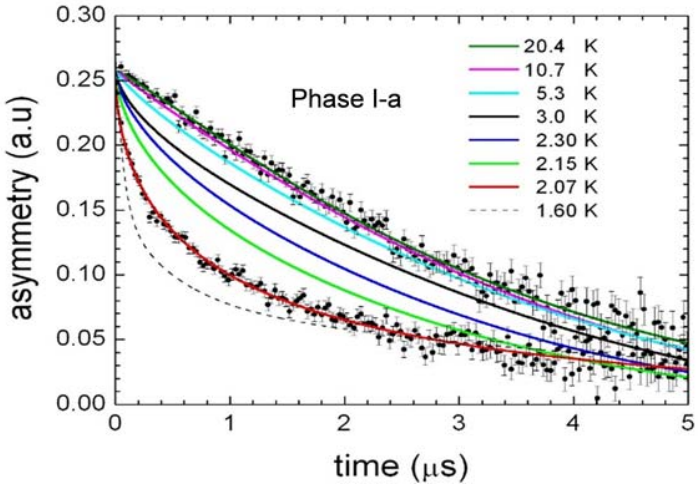

Figure S7. Examples of μSR spectra of phase **I-a** recorded at low temperatures. Lines are fits of the data using the fit function specified in the text: $KT \cdot e^{-(\lambda t)^{\beta}}$.

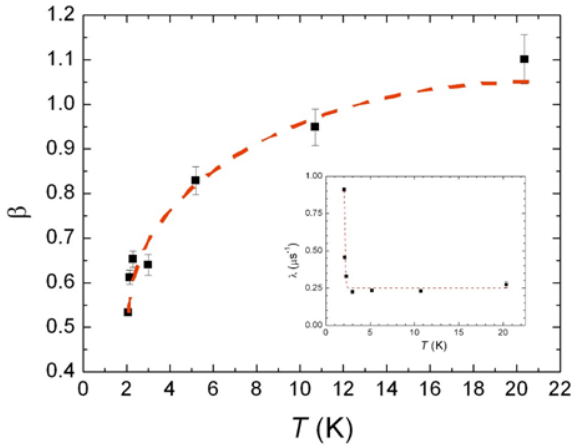

Figure S8. Temperature dependence of the fit parameter β and λ (inset) of phase **I-a**. The line is guide to the eye. β gradually decreases down to about 0.5 at 2.07 K , while λ drastically increases from 0.25 at 5 K to 0.90 at 2.07 K.

Data below 2.07 K spectra were fitted using a combination of fast (2/3 term) /slow (1/3 term) relaxing exponentials with an amplitude ratio of about 2/1, as expected for a magnetic sample: $AP(t) = \left(A_1 e^{-\lambda_1 t} + A_2 e^{-\lambda_2 t}\right) + A_3 e^{-\lambda_3 t}$. Recall that in the magnetic phase of a sample the muons ensemble is, in general, fast depolarized. An average of 2/3 of the muons (2 parts) will see magnetic fields perpendicular to their initial polarization ⇨ they perform Larmor precession around those fields, while 1/3 of the muons (one part) will sense magnetic fields parallel to their initial polarization and therefore will not process. Those muons are even not depolarized if the magnetism of the sample is static (neither a field distribution parallel to the initial polarization nor field dynamics along the initial muon polarization will produce depolarization/relaxation of the muon spin). However, if field fluctuations perpendicular to the muon spin are present, they can

ELECTRONIC SUPLEMENTARY MATERIAL

induce spin-flips and the 1/3 term becomes time dependent (exponential). The amplitude ratio of the 1/3 term (relaxing) and the 2/3 term (oscillating or fast depolarized) is 1/2. The "magnetic part" of the μSR spectra of phase **I-a** could be described by a purely exponential $A_{magn} P_{magn}(t)$, i.e. no oscillations are observed in the μSR spectra. The fitted spectra are displayed in Figure S9 and the temperature dependence of the fast relaxation rates λ_1 and λ_2 in Figure S10. These μSR data, confirms the onset of a magnetic ordering detected by magnetization and Mössbauer measurements in phase **I-a** at low temperatures. In addition, the values of λ_3 are similar to those of λ at high temperatures, indicating that the ordering below 2 K could be not static.

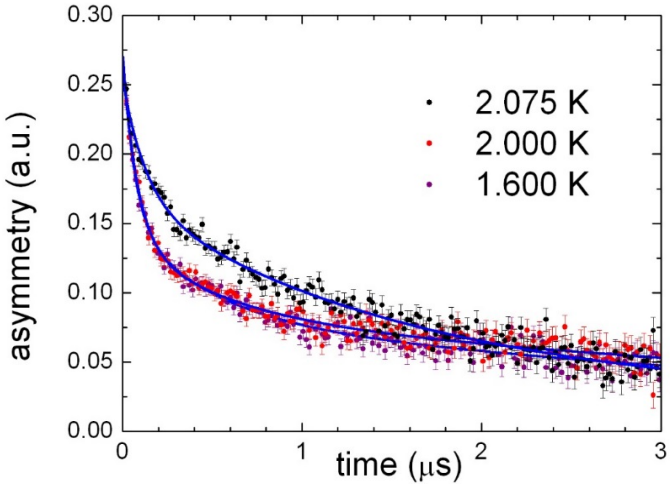

Figure S9. μSR spectra of phase **I-a** fitted using a combination of exponentials, as described in the text.

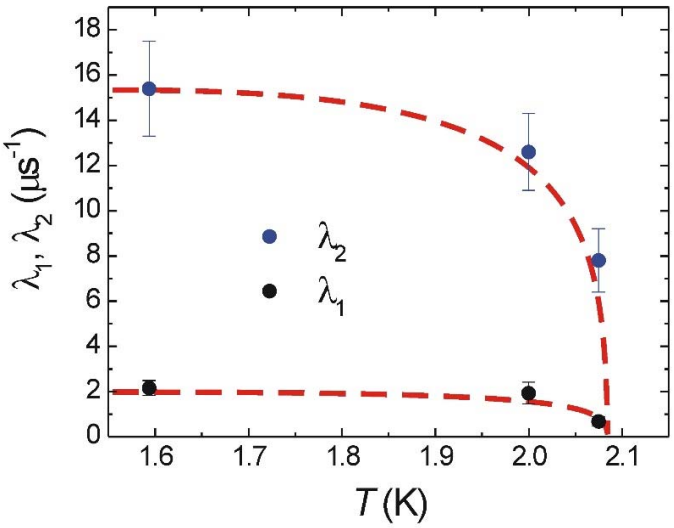

Figure S10. Temperature dependence of λ_1 and λ_2 of phase **I-a**. The lines are guide to the eye.

ELECTRONIC SUPLEMENTARY MATERIAL

The μSR spectra recorded 5.23 K of phase **I-b** (one can observe that a fast component develops below this temperature) indicates that the sample becomes magnetic. These data could be fitted using 4 oscillatory components (Figure S11),

$$AP(t) = A_1 e^{-\lambda_1 t}\cos(2\pi\nu_1 t + \varphi_1) + A_2 e^{-\lambda_2 t}\cos(2\pi\nu_2 t + \varphi_2) + \\ + A_3 e^{-\lambda_3 t}\cos(2\pi\nu_3 t + \varphi_3) + A_4 e^{-\lambda_4 t}\cos(2\pi\nu_4 t + \varphi_4) + A_5 e^{-\lambda_5 t} + A_6 e^{-\lambda_6 t} \quad (3)$$

The four oscillatory terms describe the behavior of muons stopped in an interstitial site where they "see" magnetic field: $\nu_i = \frac{\gamma}{2\pi} B_i$. Not all the phases in eq. 3 are close to zero, which can be understood as a wide field distribution. The fifth term, corresponds to muons sensing a large local field and/or field distribution, so large that the signal disappears before the first half of an oscillation. The last term is the 1/3 term, see the discussion above. The following equalities hold: $\frac{\sum_1^6 A_i}{3} = A_6$ or $\frac{\sum_1^5 A_i}{2} = A_6$ i.e. the sum of the amplitudes of the μSR signals corresponding to the fast depolarized signals is twice the amplitude of the μSR signal corresponding to the non-oscillating small relaxing term.

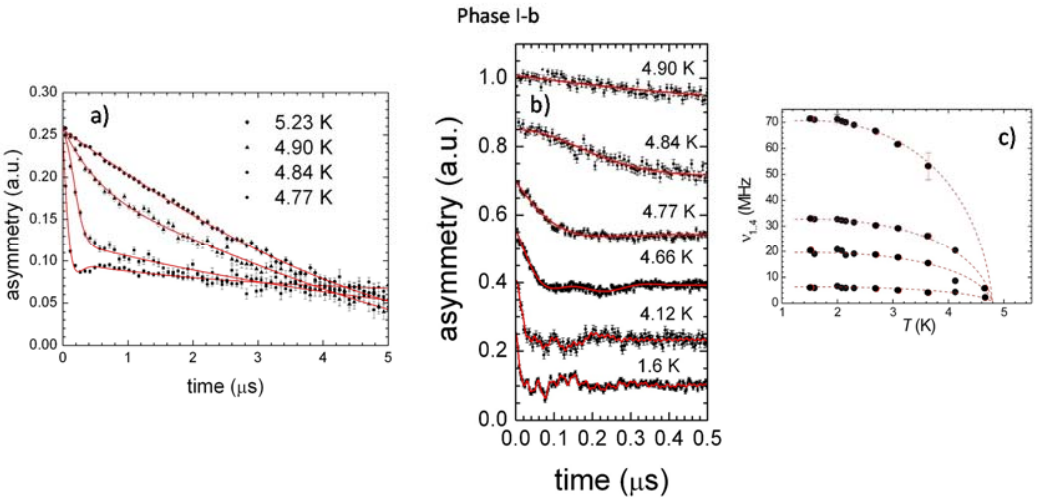

Figure S11.a) Magnetic transition is in-between 4.9 and 5.23 K of phase **I-b**. b) μSR spectra recorded below 4.90 K. c) The temperature dependence of the fitted frequencies.

ELECTRONIC SUPLEMENTARY MATERIAL

Detail of magnetic structure determination The possible magnetic structures, were checked using Bertaut's symmetry analysis method.[21] The irreducible representations (irreps) compatible with the indexed propagation vector [**k** = (0, 0, 0)] allows us to determine the symmetry constraints between the different magnetic moments of the Fe^{3+} atom within the magnetic unit cell. The total magnetic representation of the propagation vector group can be decomposed on four irreducible representations, all of them one-dimensional. The Γ_{mag} can be represented as Eq (4):

$$\Gamma_{mag} = 3(\Gamma_1 \oplus \Gamma_2 \oplus \Gamma_3 \oplus \Gamma_4). \qquad (4)$$

The magnetic moment of the $Fe(1)^{3+}$ and $Fe(2)^{3+}$ sites, both located on the 4*e* Wyckoff positions, are obtained from the basis vectors as; $\mathbf{m}_{4e}(1)$ = (u, v, w), $\mathbf{m}_{4e}(2)$ = (-u, v, -w), $\mathbf{m}_{4e}(3)$ = (-u, -v, -w) and $\mathbf{m}_{4e}(4)$ = (u, -v, w) for *irrep* Γ_1. For $\mathbf{m}_{4e}(1)$ = (u, v, w), $\mathbf{m}_{4e}(2)$ = (-u, v, -w), $\mathbf{m}_{4e}(3)$ = (u, v, w) and $\mathbf{m}_{4e}(4)$ = (-u, v, -w), the Γ_3 presents $\mathbf{m}_{4e}(1)$ = (u, v, w), $\mathbf{m}_{4e}(2)$ = (u, -v, w), $\mathbf{m}_{4e}(3)$ = (-u, -v, -w) and $\mathbf{m}_{4e}(4)$ = (-u, v, -w) while Γ_4 give rise to $\mathbf{m}_{4e}(1)$ = (u, v, w), $\mathbf{m}_{4e}(2)$ = (u, -v, w), $\mathbf{m}_{4e}(3)$ = (u, v, w) and $\mathbf{m}_{4e}(4)$ = (u, -v, w). In all cases there are three degrees of freedom (u, v, w) for each $Fe(1)^{3+}$ and $Fe(2)^{3+}$ sites, and therefore the global degree of freedom is six (see Table S7).

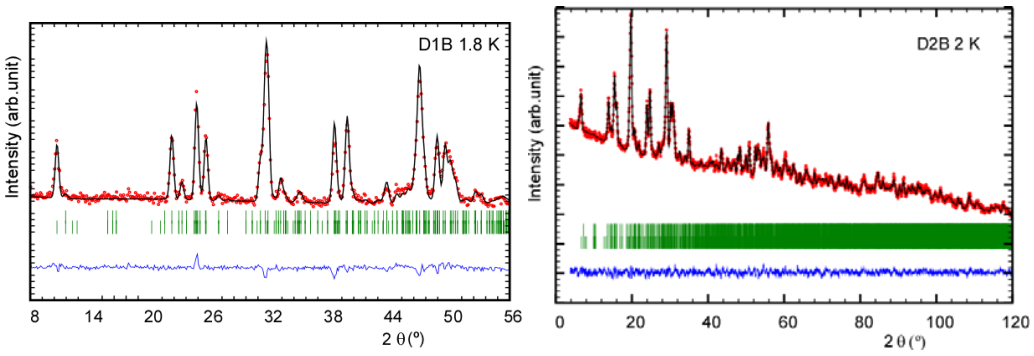

Figure S12. D1B and D2B neutron diffraction data of phase **I-a** at 1.8 and 2 K, respectively. Positions of the Bragg reflections for the nuclear (first row) and magnetic (second row) structures are presented. The difference curves are plotted at the bottom.

Rietveld refinement of the D1B (1.8 K) and D2B (2 K) patterns, where the atomic coordinates and isotropic temperature factors of the nuclear part were fixed to those obtained from the D2B pattern at 10 K, shows that Γ_1 is the only irrep that provides a satisfactory agreement between the calculated and the experimental diffraction pattern.

ELECTRONIC SUPLEMENTARY MATERIAL

DFT calculations of anion-π interactions. Taking the intermolecular distances obtained by high resolution NPD at 10 K and comparing them with IUPAC recommendation[22] [bonding contact should be shorter than the sum of the vdw (≤ 3.65 Å)], only phase **I-b** displays notable features that would support the existence of attractive anion-π interactions[23] [where chloride should be located over the center of the π system (θ = 90 ± 10º)]. To further check their presence in the condensed phase at 0 K, we obtain the projected density of states (PDOS) of the imidazolium with the chloride of the metal complex anion, [Figure S13]. We detected an extensive range of energies between 0 and -3 eV below the Fermi energy, where the PDOS reach a non-zero value, evidencing the existence of a bonding between them. To visualize the shape of one of these states, we have selected a representative state at the Gamma point, with an energy of -2.34 eV below the Fermi energy [Figure S13]. The isosurface for a value of the wave function of 0.012 displays how the wave function can connect Fe(1) and Fe(2) from layer to layer across the π orbital of the imidazolium ring (see Figure 10 of the article).

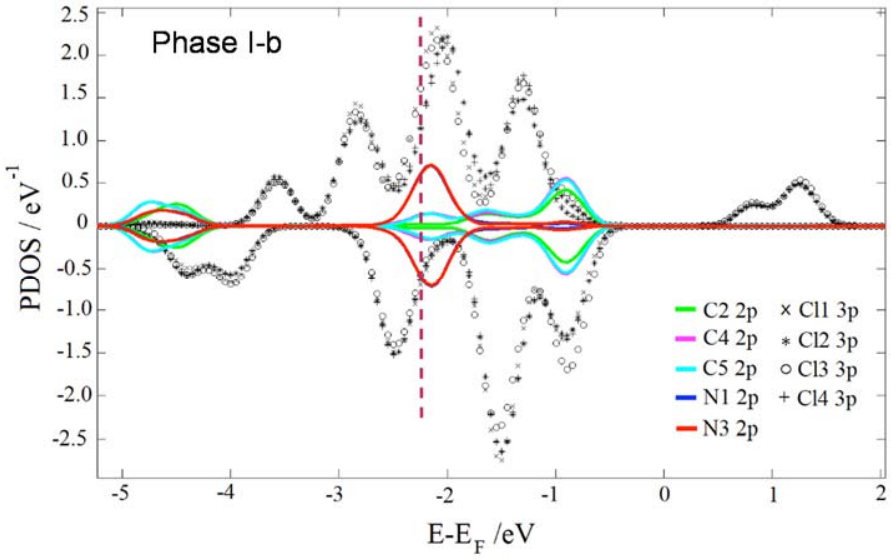

Figure S13: PDOS of clhorides from a $[FeCl_4]^-$ ion (black marks) with the atoms in the imidazolium ring (color lines). Dashed line shows the state with energy of −2.34 eV below the Fermi energy, where there is orbital overlapping.

ELECTRONIC SUPLEMENTARY MATERIAL

Table S1. Crystallographic data and structure refinement details for DiminFeCl_4 from SXPD data at 300 K (phase **II**), 100 K (phase **I-a**) and 220 K (phase **I-b**).

	DiminFeCl_4 at 300K	**DiminFeCl_4 at 100K**	**DiminFeCl_4 at 220K**
Molecular formula	$C_5H_9N_2$, Cl_4Fe	$C_5H_9N_2$, Cl_4Fe	$C_5H_9N_2$, Cl_4Fe
Formula weight	294.79	294.79	294.79
Crystal System	monoclinic	orthorhombic	monoclinic
Space group	$P2_1$	$P2_12_12_1$	$P2_1/c$
a (Å)	6.5434(2)	9.1242(1)	14.1391(3)
b (Å)	14.0286(2)	13.8132(2)	13.7039(3)
c (Å)	6.5314(2)	9.0359(1)	13.2935(3)
α (º)	90.0	90.0	90.0
β (º)	89.921(1)	90.0	115.539(2)
γ (º)		90.0	90.0
Volume (Å^3)	599.55(4)	1138.84(2)	2324(4)
Z	2	4	8
Calculated density (g/cm^3)	1.633	1.719	1.685
Measurement temp. (K)	300	100	220
Wavelength (Å)	0.61969	0.61969	0.62093
Measured 2θ range, step (º)	1.104 to 63.096, 0.006	1.104 to 63.096, 0.006	1.998 to 30.171, 0.004
Rietveld refinement details:			
Profile function	Pseudo-Voigt	Pseudo-Voigt	Pseudo-Voigt
2θ range used (º)	4.006 to 40.000	3.006 to 40.002	3.604 to 30.171
Num. of reflections	888	948	1442
Data points	5999	6166	6643
Parameters[a]	50[b]	50[a]	87[b]
Restraints	33	16	46
R_{wp}	0.061	0.058	0.037
R_{exp}	0.010	0.010	0.005
$\chi_{Rietveld}/\chi_{Pattern\text{-}Matching}$	1.421	1.241	2.295

[a]*Parameters: Atomic coordinates (x,y,z), isotropic atomic displacement parameters (dimim, Cl, Fe), 6 profile parameters, zero offset, scale factor, cell parameters.*
[b] *Restraints: Bond distances, angles and dimim plane.*

ELECTRONIC SUPLEMENTARY MATERIAL

Table S2. Crystallographic data and structure refinement details for Dimin$FeCl_4$ from high resolution NPD data at 10 K for phase **I-a** and phase **I-b**.

	Phase Ia	**Phase Ib**
Molecular formula	$C_5H_9N_2$, Cl_4Fe	$C_5H_9N_2$, Cl_4Fe
Formula weight	294.79	294.79
Crystal System	Orthorhombic	Monoclinic
Space group	$P2_12_12_1$	$P2_1/c$
a (Å)	9.0897(2)	13.9037(6)
b (Å)	13.7423(3)	13.5621(6)
c (Å)	8.97670(19)	13.1303(6)
α (º)	90.0	90.0
β (º)	90.0	115.453(3)
γ (º)	90.0	90.0
Volume (Å^3)	1121.31(4)	2235.59(16)
Z	4	8
Calculated density (g/cm^3)	1.746	1.752
Measurement Temperature (K)	10K	10K
Radiation (wavelengths in Å)	1.5942	1.5942
Measured 2θ range, stepsize (º)	0.00–159.95, 0.05	0.00–159.95, 0.05
Rietveld refinement details:		
Profile function	Pseudo-Voigt	Pseudo-Voigt
2θ range used (º)	6.00 to 140.0	6.00 to 120.00
Num. of reflections	1336	4529
Data points	2680	2280
Parameters	77	141
Restraints	43	86
R_{wp}	0.012	0.011
R_{exp}	0.009	0.010
$\chi_{Rietveld}/\chi_{Pattern\text{-}Matching}$	1.512	1.613

ELECTRONIC SUPLEMENTARY MATERIAL

Table S3. Final refined positional coordinates from SXPD and high resolution NPD pattern of Dimim[$FeCl_4$] at 300 K (phase **II**). Label of the atoms as in Figure 10.

	Dimim[$FeCl_4$] at 300K[a] from SXPD			Dimim[$FeCl_4$] at 300K[b][28] from NPD		
Atom	*x/a*	*y/b*	*z/c*	*x/a*	*y/b*	*z/c*
Fe	0.2366(7)	0.35963(7)	0.2652(4)	0.2240(24)	0.3624(23)	0.2581(24)
Cl1	0.1158(18)	0.2334(9)	0.4198(4)	0.0774(47)	0.2310(27)	0.3821(51)
Cl2	0.1951(11)	0.3617(12)	-0.0539(4)	0.1397(46)	0.3776(31)	-0.0635(28)
Cl3	0.1309(19)	0.4905(8)	0.4140(4)	0.0889(55)	0.4864(29)	0.4112(50)
Cl4	0.5722(7)	0.3522(11)	0.3336(4)	0.5520(25)	0.3620(29)	0.2987(36)
N1	0.384(3)	0.6492(9)	0.0546(4)	0.4209(32)	0.6507(15)	0.0900(35)
C2	0.426(3)	0.5927(10)	-0.1017(4)	0.3990(31)	0.6055(16)	-0.0836(35)
N3	0.615(3)	0.5580(9)	-0.0759(4)	0.5629(34)	0.5551(15)	-0.1278(34)
C4	0.690(3)	0.5930(11)	0.1014(4)	0.6911(31)	0.5672(16)	0.0243(36)
C5	0.551(3)	0.6507(11)	0.1759(4)	0.6025(33)	0.6259(16)	0.1617(34)
C1'	0.193(3)	0.7033(10)	0.0759(4)	0.2770(38)	0.7108(16)	0.1800(42)
C1"	0.717(4)	0.4870(8)	-0.2048(4)	0.5768(44)	0.4978(16)	-0.3023(35)
H2	0.33480	0.58170	-0.20830	0.2699(35)	0.6096(19)	-0.1794(43)
H4	0.81550	0.57570	0.15690	0.8345(33)	0.5344(16)	0.0413(46)
H5	0.57210	0.68530	0.29550	0.6734(42)	0.6487(18)	0.2964(34)
H1A'	0.21730	0.77070	0.06960	0.1307(37)	0.6884(42)	0.1302(98)
H1B'	0.10710	0.68480	-0.03660	0.3039(91)	0.7824(16)	0.1314(99)
H1C'	0.12520	0.68820	0.20250	0.2825(93)	0.7016(46)	0.3422(42)
H1A"	0.72050	0.50980	-0.34330	0.4324(71)	0.4987(35)	-0.3794(50)
H1B"	0.85290	0.47280	-0.15990	0.6895(57)	0.5215(36)	-0.4058(67)
H1C"	0.63470	0.43020	-0.19820	0.5936(98)	0.4241(16)	-0.2621(52)

Full occupancies for all atoms.
(a) a = 6.5434(2) Å, b = 14.0286(2) Å, c = 6.5314(2) Å, $\alpha = \gamma = 90º$, β = 89.921(1)º, s.g. $P2_1$. B_{Fe} = 7.4(1) Å^2; B_{Cl} = 8.1(1) Å^2; $B_{C,H}$ = 10.2(1) Å^2.
(b) a = 6.5419(27) Å, b = 14.0374(26) Å, c = 6.5357(30) Å, $\alpha = \gamma = 90º$, β = 90.006(23) º, s.g. $P2_1$. $B_{overall}$ = 5.4(9) Å^2 ..

ELECTRONIC SUPLEMENTARY MATERIAL

Table S4. Final refined positional coordinates from SXPD at 100 K and high resolution NPD pattern at 10 K of Dimim[$FeCl_4$] (phase **I-a**). Label of the atoms as in Figure 10.

	Dimim[$FeCl_4$] at 100K[a]			Dimim[$FeCl_4$] at 10K[b]		
Atom	*x/a*	*y/b*	*z/c*	*x/a*	*y/b*	*z/c*
Fe	0.2564(2)	0.2478(4)	0.2610(4)	0.2582(6)	0.2462(7)	0.2683(8)
Cl1	0.3986(5)	0.3757(3)	0.2302(4)	0.4019(8)	0.3728(5)	0.2267(9)
Cl2	0.1079(4)	0.2362(5)	0.0727(4)	0.1031(8)	0.2359(5)	0.0764(6)
Cl3	0.3818(5)	0.1106(3)	0.2810(4)	0.3799(9)	0.1055(5)	0.2870(8)
Cl4	0.1305(4)	0.2729(4)	0.4643(4)	0.1329(9)	0.2734(6)	0.4730(7)
N1	-0.0757(13)	0.4519(11)	0.2411(4)	-0.0700(6)	0.4539(4)	0.2437(4)
C2	0.0113(17)	0.4947(15)	0.3407(4)	0.0187(8)	0.4947(6)	0.3421(3)
N3	0.1042(13)	0.5513(10)	0.2651(4)	0.1119(6)	0.5526(4)	0.2645(4)
C4	0.0742(13)	0.5441(10)	0.1155(4)	0.0829(9)	0.5475(7)	0.1210(4)
C5	-0.0402(15)	0.4838(11)	0.1009(4)	-0.0292(9)	0.4825(6)	0.1070(3)
C1'	-0.1913(12)	0.3825(10)	0.2860(4)	-0.18449(14)	0.38529(9)	0.28813(10)
C1"	0.2228(13)	0.6094(11)	0.3319(4)	0.22694(15)	0.61194(8)	0.33338(12)
H2	0.00240	0.48860	0.45760	0.032(4)	0.482(3)	0.4550(7)
H4	0.13570	0.58080	0.03590	0.139(3)	0.587(2)	0.042(2)
H5	-0.08870	0.45740	0.00410	-0.074(3)	0.454(2)	0.0101(17)
H1A'	-0.29030	0.39100	0.22580	-0.137(3)	0.3217(11)	0.326(3)
H1B'	-0.14360	0.31530	0.26430	-0.262(2)	0.413(2)	0.360(2)
H1C'	-0.20970	0.39120	0.40130	0.3270(15)	0.5839(20)	0.300(3)
H1A"	0.30660	0.56260	0.36590	0.224(3)	0.6821(9)	0.293(3)
H1B"	0.26220	0.65730	0.24910	0.209(3)	0.614(2)	0.4469(6)
H1C"	0.17970	0.64840	0.42270	0.2582(6)	0.2462(7)	0.2683(8)

Full occupancies for all atoms.
(a) $a = a = 9.1242(1)$ Å, $b = 13.8132(2)$ Å, $c = 9.0359(1)$ Å, $\alpha = \beta = \gamma = 90º$, s.g. $P2_12_12_1$. $B_{Fe} = 2.3(1)$ Å^2; $B_{Cl} = 2.9(1)$ Å^2; $B_{C,H} = 2.5(1)$ Å^2.
(b) $a = 9.0897(2)$ Å, $b = 13.7423(3)$ Å, $c = 9.9767(19)$ Å, $\alpha = \beta = \gamma = 90º$, s.g. $P2_12_12_1$. $B_{overall} = B_{Fe} = 0.3(1)$ Å^2; $B_{Cl} = 0.4(1)$ Å^2; $B_N = 0.6(1)$ Å^2, $B_C = 0.3(1)$ Å^2, $B_H = 4.0(2)$ Å^2.

ELECTRONIC SUPLEMENTARY MATERIAL

Table S5. Final refined positional coordinates from SXPD at 220 K and high resolution NPD at 10 K of Dimim[$FeCl_4$] (phase **I-b**). Label of the atoms as in Figure 10.

	Dimim[$FeCl_4$] at 220K[a]			Dimim[$FeCl_4$] at 10K[b]		
Atom	*x/a*	*y/b*	*z/c*	*x/a*	*y/b*	*z/c*
Fe1	0.4018(4)	0.2525(6)	0.0628(4)	0.4059(13)	0.2547(13)	0.0660(13)
Cl1	0.4494(8)	0.1094(8)	0.0216(4)	0.4432(14)	0.1065(11)	0.0160(13)
Cl2	0.4331(7)	0.2594(9)	0.2376(4)	0.4302(13)	0.2617(13)	0.2397(15)
Cl3	0.4890(7)	0.3649(8)	0.0248(4)	0.4867(14)	0.3682(12)	0.0212(16)
Cl4	0.2389(8)	0.2708(8)	-0.0331(4)	0.2313(13)	0.2789(13)	-0.0373(14)
N1	0.2514(19)	0.5235(11)	0.0499(4)	0.2590(7)	0.5295(13)	0.0429(3)
C2	0.1870(17)	0.4728(11)	0.0797(4)	0.1982(9)	0.4822(17)	0.0793(4)
N3	0.2344(18)	0.4534(10)	0.1861(4)	0.2455(7)	0.4666(12)	0.1910(5)
C4	0.3305(18)	0.4904(12)	0.2244(4)	0.3386(10)	0.5097(16)	0.2294(2)
C5	0.3401(17)	0.5341(11)	0.1394(4)	0.3435(7)	0.5508(15)	0.1376(4)
C1'	0.228(2)	0.5591(12)	-0.0615(4)	0.22921(14)	0.55319(13)	-0.0752(2)
C1"	0.1915(19)	0.3991(11)	0.2527(4)	0.20866(16)	0.40398(16)	0.25791(17)
H2	0.119	0.4537	0.0328	0.124(2)	0.458(4)	0.023(4)
H4	0.3823	0.4872	0.2973	0.389(4)	0.514(5)	0.3145(12)
H5	0.3988	0.5671	0.1426	0.408(3)	0.585(4)	0.133(5)
H1A'	0.2947	0.5664	-0.0635	0.299(2)	0.537(4)	-0.081(5)
H1B'	0.1881	0.5094	-0.1133	0.168(3)	0.509(4)	-0.129(4)
H1C'	0.1905	0.6198	-0.0815	0.212(5)	0.6270(12)	-0.093(5)
H1B"	0.1315	0.3572	0.2182	0.222(5)	0.442(4)	0.331(3)
H1A"	0.1787	0.4457	0.2993	0.1281(9)	0.398(4)	0.207(4)
H1C"	0.2518	0.3605	0.2972	0.248(4)	0.338(2)	0.284(5)
Fe2	0.0841(5)	0.7404(5)	0.1486(4)	0.0933(13)	0.7399(14)	0.1480(13)
Cl1b	0.0274(9)	0.6192(8)	0.2207(4)	0.0251(14)	0.6172(13)	0.2141(14)
Cl2b	0.2558(7)	0.7472(10)	0.2413(4)	0.2609(11)	0.7454(14)	0.2433(13)
Cl3b	0.0210(8)	0.8856(7)	0.1611(4)	0.0184(13)	0.8833(13)	0.1566(14)
Cl4b	0.0395(7)	0.7106(6)	-0.0290(4)	0.0540(13)	0.7048(12)	-0.0253(14)
N1b	0.2925(13)	0.9244(11)	0.0779(4)	0.2870(7)	0.9306(9)	0.0785(7)
C2b	0.2142(13)	0.9835(12)	0.0574(4)	0.2057(8)	0.9936(11)	0.0570(8)
N3b	0.2299(16)	1.0375(11)	0.1457(4)	0.2293(6)	1.0525(9)	0.1434(7)
C4b	0.3246(17)	1.0106(14)	0.2266(4)	0.3255(5)	1.0260(7)	0.2204(9)
C5b	0.3637(14)	0.9403(13)	0.1866(4)	0.3610(9)	0.9479(12)	0.1808(9)
C1'b	0.3100(17)	0.8495(12)	0.0084(4)	0.29487(13)	0.85235(17)	0.00514(19)
C1"b	0.1616(18)	1.1173(12)	0.1594(4)	0.16357(16)	1.12610(18)	0.16487(15)
H2b	0.1573	0.9864	-0.017	0.134(2)	1.001(4)	-0.014(3)
H4b	0.3574	1.0315	0.2985	0.431(2)	0.908(4)	0.220(5)
H5b	0.425	0.9078	0.2155	0.375(4)	1.072(3)	0.285(3)
H1A"b	0.2038	1.1604	0.2189	0.166(5)	1.125(5)	0.244(2)
H1B"b	0.1288	1.1538	0.0913	0.182(5)	1.191(2)	0.136(4)
H1C"b	0.1087	1.0879	0.1766	0.0837(11)	1.120(5)	0.111(4)
H1A'b	0.3783	0.8597	0.0116	0.359(3)	0.866(5)	-0.012(4)
H1B'b	0.3097	0.7904	0.047	0.308(5)	0.7850(20)	0.045(4)
H1C'b	0.2594	0.8445	-0.068	0.223(3)	0.847(5)	-0.066(3)

Full occupancies for all atoms.(a) $a = a = 14.1391(3)$ Å, $b = 13.7039(3)$ Å, $c = 13.2935(3)$ Å, $\alpha = \beta = \gamma = 90^o$, $\beta = 115.539(2)$ s.g. $P2_1/c$. . $B_{Fe} = 5.4(1)$ Å^2; $B_{Cl} = 4.2(1)$ Å^2; $B_N = 6.7(1)$ Å^2, $B_{C,H} = 7.9(1)$ Å^2.(b) $a =$

ELECTRONIC SUPLEMENTARY MATERIAL

13.9037(6) Å, b = 13.5621(6) Å, c = 13.1303(6) Å, $\alpha = \beta = \gamma = 90º$, β =115.453(3) º s.g. $P2_1/c$. B_{Fe} = 0.8(2) Å^2; B_{Cl} = 0.8(1) Å^2; B_N = 1.5(2) Å^2, , B_C = 1.0(1) Å^2, B_H = 3.4(2) Å^2

Table S6. Estimated parameters from the Mössbauer spectra of Dimim[$FeCl_4$] for phase **I-a** and **I-b** taken at different temperatures.

T (K)	IS (mm/s)	QS (mm/s)	(2ε) (mm/s)	B_{hf} (T)	Γ (mm/s)	I
			Phase I-a			
70	0.34	0.22	-	-	0.37	100
10	0.33	0.22	-	-	0.38	100
4.0	0.33	0.22	-	-	0.37	100
2.1	0.31	0.20	-	-	0.37	100
1.9	0.32	0.22	-	-	0.54	100
			Phase I-b			
70	0.33	0.21	-	-	0.37	100
6	0.34	0.19	-	-	0.36	100
4.0	0.33	-	0.17	27.1	0.31	48
	0.33	-	0.04	28.7	0.31	46
	0.33	0.15	-	-	0.34	6
3.0	0.33	-	0.09	38.1	0.33	48
	0.33	-	0.12	39.0	0.32	46
	0.32	0.15	-	-	0.29	6
2.1	0.33	-	0.07	41.5	0.35	49
	0.32	-	0.15	42.9	0.35	45
	0.33	0.18	-	-	0.33	6
1.9	0.33	-	0.04	42.7	0.37	48
	0.33	-	0.18	44.1	0.36	46
	0.33	0.19	-	-	0.34	6

IS, isomer shift relative to metallic Fe at 295K; QS, quadrupole splitting of doublets; (2ε) quadrupole shift for magnetic sextets; B_{hf} magnetic hyperfine field. Estimated standard deviations are < 0.02 mm/s for IS, QS and (2ε), <0.5T for B_{hf} .

Table S7. Basis vectors of the four possible irreducible representation of the space group $P2_1/c$ for **k** = (0, 0, 0) for the $Fe(1)^{3+}$ and $Fe(2)^{3+}$ ions located on the (0.0930, 0.7410, 0.1500) and (0.4080, 0.2550, 0.0660) positions, respectively.

	x, y, z	$-x, y+1/2, -z+1/2$	$-x, -y, -z$	$x, -y-1/2, z-1/2$
Γ_1	(100)(010)(001)	(-100)(010)(00-1)	(-100)(0-10)(00-1)	(100)(0-10)(001)
Γ_2	(100)(010)(001)	(-100)(010)(00-1)	(100)(010)(001)	(-100)(010)(00-1)
Γ_3	(100)(010)(001)	(100)(0-10)(001)	(-100)(0-10)(00-1)	(-100)(010)(00-1)
Γ_4	(100)(010)(001)	(100)(0-10)(001)	(100)(010)(001)	(100)(0-10)(001)

ELECTRONIC SUPLEMENTARY MATERIAL

Table S8. Final refined positional coordinates from DFT calculations at 0 K for Phase I-b For the phase I-a these are included in Ref 28 of the manuscript.

Dimim[$FeCl_4$] phaseI-b at 0 K			
Atom	*x/a*	*y/b*	*z/c*
Fe1	0.59348191	0.75665654	0.43810872
Cl1a	0.55016966	0.61475831	0.48225811
Cl2a	0.76309147	0.77793962	0.53832890
Cl3a	0.51008025	0.87654072	0.47537285
Cl4a	0.56306780	0.75906879	0.25952253
N1	0.77000268	0.95249600	0.85514358
C2	0.79392185	0.01112444	0.94157203
N3	0.71301673	0.06824115	0.92232195
C4	0.63551620	0.04538282	0.82105631
C5	0.67111947	0.97293592	0.77904674
C1'	0.83668056	0.87755668	0.84483895
C1"	0.70774281	0.14205202	0.99701624
H2	0.86608427	0.01228633	0.01382393
H4	0.56362619	0.08358960	0.78753623
H5	0.63507541	0.93422950	0.70282098
H1A'	0.82050779	0.86958606	0.75843473
H1B'	0.82172304	0.81095932	0.87710966
H1C'	0.91660722	0.89806816	0.89131502
H1A"	0.67314031	0.20565605	0.94912639
H1B"	0.78535432	0.15762574	0.05775610
H1C"	0.66045179	0.11713041	0.03730834
Fe2	0.08551877	0.73680022	0.14684002
Cl1b	0.03047235	0.61580881	0.21836829
Cl3b	0.01713426	0.87874255	0.15637262
Cl2b	0.25663029	0.74686311	0.23967546
Cl4b	0.04392564	0.70300669	0.96913173
N1b	0.24467341	0.46445719	0.18841636
C2b	0.19526848	0.47965906	0.07972900
N3b	0.25780201	0.52892687	0.04740026
C4b	0.34950986	0.54573146	0.13812216
C5b	0.34134859	0.50519726	0.22628776
C1'b	0.20507078	0.40915879	0.25479915
C1"b	0.23373065	0.55789705	0.93436010
H2b	0.11891994	0.45518494	0.02698389
H4b	0.41111244	0.58571422	0.13215515
H5b	0.39472002	0.50265771	0.31177660
H1A'b	0.12320175	0.39700965	0.20730263
H1B'b	0.21753840	0.44912483	0.32885141
H1C'b	0.24606845	0.34163290	0.27748439
H1A"b	0.15663966	0.53361456	0.88093816
H1B"b	0.29002225	0.52622516	0.90973000
H1C"b	0.23716547	0.63515567	0.93001858

ELECTRONIC SUPLEMENTARY MATERIAL

Table S9. Most Relevant Interatomic Distances in the crystal structures of phase I-a at 100 K, phase II at 300 K and phase I-b at 220 K obtained from Rietveld refinements of synchrotron powder diffraction data.

(a)

	Phase I-a 100K		Phase II 300K	
	length (Å)	angle (º)	length (Å)	angle (º)
$[FeCl]^{-}$···$[Dimim]^{+}$ (potential π-d interactions)				
Fe1-Cl1··centroid1	3.936(8)	81.1(2)	-	-
Fe1-Cl3··centroid1	3.901(8)	80.9(2)	3.990(11)	82.1(3)
$[Cl]^{-}$··· $[Cl]^{-}$				
Cl3···Cl4	3.610(6)			
Cl1···Cl2	3.678(6)		3.92(1)	
Cl1···Cl3	3.815(6)		3.92(2)	
Cl1···Cl4			3.97(1)	
Cl2··Cl3			3.94(1)	

(b)

	Phase I-b 220 K	
	length (Å)	angle (º)
$[FeCl]^{-}$···$[Dimim]^{+}$ (potential π-d interactions)		
Fe1-Cl1··centroid1	3.76(1)	90.5(4)
Fe2-Cl2b··centroid1	3.55(2)	96.1(4)
Fe2-Cl2b··centroid2	3.77(1)	88.4(4)
Fe1-Cl4··centroid2	3.72(1)	85.6(4)
$[Cl]^{-}$··· $[Cl]^{-}$		
Cl1···Cl1	3.48(2)	
Cl4···Cl1b	3.82(1)	
Cl3···Cl3	3.80(2)	
Cl1b···Cl3b	3.76(1)	
Cl4···Cl3b	3.95(1)	
Cl2···Cl3	3.94(1)	
Cl2b···Cl3	3.95(1)	

ELECTRONIC SUPLEMENTARY MATERIAL

References:

(1). Stewart, J.; Deen, P.; Andersen, K.; Schober, H.; Barthélémy, J.-F.; Hillier, J.; Murani, A.; Hayes, T.; Lindenau, B. *Journal of Applied Crystallography* **2009**, *42*, 69.
(2). Schärpf, O.; Capellmann, H. *physica status solidi (a)* **1993**, *135*, 359.
(3). J. M. Soler, E. Artacho, J. D. Gale, A. García, J. Junquera, P. Ordejón and D. Sánchez-Portal, *J. Phys.: Cond. Matter.,* 2002, **14**, 2745-2779.
(4). G. Román-Pérez and J. M. Soler, *Phys.Rev. Lett.*, 2009, **103**, 096102.
(5). M. Dion, H. Rydberg, E. Schröder, D. C. Langreth and B. I. Lundqvist, *Phys. Rev. Lett.*, 2004, **92**, 246401.
(6). J. Kohanoff, C. Pinilla, T. G. Youngs, E. Artacho and J. M. Soler, *J Chem Phys*, 2011, **135**, 154505.
(7). N. Troullier and J. L. Martins, *Phys. Rev. B*, 1991, **43**, 1993-2006.
(8). L. Kleinman and D. M. Bylander, *Phys. Rev. Lett.*, 1982, **48**, 1425-1428.
(9). S. G. Louie, S. Froyen and M. L. Cohen, *Phys. Rev. B*, 1982, **26**, 1738-1742.
(10). E. Artacho, D. Sánchez-Portal, P. Ordejón, A. García and J. M. Soler, *Phys. Status Solidi B*, 1999, **215**, 809-817.
(11). H. J. Monkhorst and J. D. Pack, *Phys. Rev. B*, 1976, **13**, 5188-5192.
(12). J. Moreno and J. M. Soler, *Phys. Rev. B*, 1992, **45**, 13891-13898.
(13). M. Leslie and N. Gillan, *J. Phys. C: Solid State Phys.*, 1985, **18**, 973.
(14) Boultif, A.; Louer, D. *Journal of Applied Crystallography* **2004**, *37*, 724.
(15) Vallcorba, O.; Rius, J.; Frontera, C.; Peral, I.; Miravitlles, C. *Journal of Applied Crystallography* **2012**, *45*, 844.
(16) Vallcorba, O.; Rius, J.; Frontera, C.; Miravitlles, C. *Journal of Applied Crystallography* **2012**, *45*, 1270.
(17) Rius, J. *RIBOLS18: A computer program for least-squares refinement from powder diffraction data; Institut de Ciencia de Materialsde Barcelona (CSIC)*, Barcelona, Spain, **2009**.
(18) Bruno, I. J.; Cole, J. C.; Kessler, M.; Luo, J.; Motherwell, W. D. S.; Purkis, L. H.; Smith, B. R.; Taylor, R.; Cooper, R. I.; Harris, S. E.; Orpen, A. G. *Journal of Chemical Information and Computer Sciences* **2004**, *44*, 2133.
(19) de Pedro, I.; Maria Rojo, J.; Luis Pizarro, J.; Rodriguez Fernandez, J.; Sanchez Marcos, J.; Teresa Fernandez-Diaz, M.; Arriortua, M.; Rojo, T. *Journal of Materials Chemistry* **2007**, *17*, 3915.
(20) de Pedro, I.; Rojo, J. M.; Jubera, V.; Fernandez, J. R.; Marcos, J. S.; Lezama, L.; Rojo, T. *Journal of Materials Chemistry* **2004**, *14*, 1157.
(21) Bertaut, E. *Acta Crystallographica Section A* **1968**, *24*, 217.
(22) Arunan, E.; Desiraju, G. R.; Klein, R. A.; Sadlej, J.; Scheiner, S.; Alkorta, I.; Clary, D. C.; Crabtree, R. H.; Dannenberg, J. J.; Hobza, P.; Kjaergaard, H. G.; Legon, A. C.; Mennucci, B.; Nesbitt, D. J. *Pure and Applied Chemistry* **2011**, *83*, 1637.
(23) Rosokha, Y. S.; Lindeman, S. V.; Rosokha, S. V.; Kochi, J. K. *Angewandte Chemie International Edition* **2004**, *43*, 4650.

Capítulo 4

Dimim[$FeBr_4$]

4.1. Introducción

Una vez conocido que la interacción se da por medio de caminos de supercanje del tipo Fe-X–X-Fe (X = halógeno), y que en parte, la fuerza de interacción va a depender del grado de deslocalización, el siguiente paso fue estudiar el efecto del halógeno en estos sistemas. Para ello se usó un halógeno menos electronegativo, en este caso bromo, basándose en que la interacción magnética entre aniones $[FeX_4]^-$ debería ser más fuerte en el orden X = I $>$ Br $>$ Cl $>$ F.

El Dimim[$FeBr_4$] se encuentra en estado sólido a temperatura ambiente. Su caracterización térmica enfriando desde su punto de fusión de 369 K sufre una transición sólido-sólido en torno a 334 K. Por otra parte, calentando se descompone a una temperatura próxima a 684 K.

A partir de medidas de difracción en polvo de rayos X de sincrotrón y datos de difracción de neutrones de alta resolución se obtuvo que este compuesto, a temperatura ambiente, es isoestructural al Dimim[$FeCl_4$], cristalizando en un grupo espacial $P2_1$ donde sus aniones y cationes se apilan en forma de capas a lo largo del eje *b*, con distancias hierro-hierro superiores a los del compuesto clorado (6.7 Å).

Las medidas de espectroscopia Raman realizadas, aparte de permitir caracterizar los complejos aniónicos y catiónicos, mostraron por primera vez la presencia de magnones magnéticos en este tipo de compuestos a bajas temperaturas. Su caracterización magnética, por medio de medidas de susceptibilidad, magnetización y calor específico, revelan un ordenamiento tridimensional antiferromagnético con una temperatura de

Néel próxima a 9.2 K. De estos datos se deduce que los acoplamientos magnéticos se incrementan al intercambiar el halógeno cloro por el bromo dentro de la misma estructura cristalina. Los análisis de los datos de la susceptibilidad magnética utilizando modelos teóricos, revelan como la interacción más fuerte se da entre los planos.

A partir de las medidas de difracción de neutrones de alto flujo se observó que la celda magnética y nuclear son la misma, obteniendo la estructura magnética de este MIL. Ésta se corresponde con una estructura donde las capas están ordenadas internamente de manera ferromagnética pero que están acopladas antiferromagnéticamente entre ellas a lo largo de la dirección *b*. Por otro lado, analizando la disposición de las moléculas en la estructura cristalina, se observó que existía una gran posibilidad de que los anillos aromáticos y los complejos metálicos se unieran formando interacciones no-covalentes anión-π. Este tipo de enlaces son poco frecuentes en compuestos basados en imidazolio, donde ambas partes se suelen unir por puentes de hidrógeno. Para comprobar esta característica se utilizaron cálculos teóricos de DFT por medio de dos caminos; el primero calculando la "energía de ionización" en estado gaseoso, y el segundo por medio de la densidad proyectada de estados (PDOS) del imidazolio con los bromos de los complejos metálicos $[FeBr_4]^-$. Estos últimos exhibieron un gran rango de energías en las que los estados de ambas moléculas coinciden, probando la existencia de este enlace químico. Además, se representó la isosuperficie asociada a uno de estos estados y se pudo observar visualmente la conexión entre ambas moléculas.

Finalmente se realizó el análisis de las correlaciones magneto-estructurales. Los complejos metálicos se disponen dentro de la estructura cristalina con tres tipos de interacciones no covalentes: (a) puentes de hidrógeno, (b) bromo-bromo y (c) anión-π; siendo estas dos últimas las responsables del ordenamiento magnético. La fuerza de estas interacciones de supercanje dependen, por un lado, de la distancia de enlace y de los ángulos que involucran los iones. En general, distancias más cortas y ángulos más grandes (en torno a 180^o) se relacionan con constantes más fuertes de acoplamiento magnético. De acuerdo con los datos obtenidos la interacción de supercanje más fuerte se da entre planos, adquiriendo el carácter antiferromagnético del ordenamiento, en buen acuerdo con los datos de caracterización magnética. Por otro lado, los efectos electrostáticos y la deformación de la carga eléctrica[34] también influyen en la fuerza del ordenamiento. Con los resultados obtenidos por DFT puede verse que existe una deslocalización de espín en torno a los bromos y el solapamiento es mayor para la interacción interplanar. Estos resultados y su comparación con los del compuesto isoestructural de cloro indican que el aumento de la interacción magnética no puede deberse a factores geométricos

de las interacciones no enlazantes, ya que las distancias hierro-hierro son mayores. De esta forma, la deslocalización magnética, la cual aumenta al sustituir cloro por bromo, favorece el acoplamiento magnético, aumentando la temperatura de Néel.

4.2. Artículo V

Artículo publicado en la revista *Inorganic Chemistry*: "Anion-π and Halide-Halide Non-bonding Interactions in a New Ionic Liquid Based on Imidazolium Cation with Three-Dimensional Magnetic Ordering in the Solid State"

Anion−π and Halide–Halide Nonbonding Interactions in a New Ionic Liquid Based on Imidazolium Cation with Three-Dimensional Magnetic Ordering in the Solid State

Abel García-Saiz, Imanol de Pedro, Pedro Migowski, Oriol Vallcorba, Javier Junquera, Jesús Angel Blanco, Oscar Fabelo, Denis Sheptyakov, Joao Carlos Waerenborgh, María Teresa Fernández-Díaz, Jordi Rius, Jairton Dupont, Jesús Antonio Gonzalez, Jesús Rodríguez Fernández.

Inorg. Chem.2014, 53, 16, 8384-8396

https://doi.org/10.1021/ic500882z

Supplementary Material

EXPERIMENTAL SECTION

2.1. Synthesis and Elemental Analysis and Thermal Investigations.
Synthesis: 1,3-dimethylimidazolium iodide (12 g, 53.56 mMol) was dissolved in 500 ml of distilled water and passed through a chloride free (Volhard method tested) Amberlite IRA-400 column (OH- form). Then, the iodine-free compound,
1,3-dimethylimidazolium hydroxide solution, also tested by the Volhard method, was reacted with concentrated hydrobromic acid till pH 7 and the water removed in rotary evaporator. The remaining water was vacuum removed at 100ºC. The subsequent solids were then dissolved in dichloromethane and dried over anhydrous Na_2CO_3, filtered and the solvent was vacuum removed, yielding 9.8 g of (82%) of 1,3-dimethylimidazolium bromide. In a glove-box, the 1,3-dimethylimidazolium bromide (1.5 g, 8.46 mmol) was mixed with anhydrous $FeBr_3$ (98.5 %, Brand) (2.50 g, 8.46 mmol) in a 8 mL vial. The exothermic reaction melted the mixture and the desired 1,3-dimethylimidazolium tetrabromoferrate product was obtained as a brown solid, 4.00 g (100% yield).
Chemical analysis: Microanalytical data (C, H and N) were obtained with an Elemental model Vario 51 MACRO elemental analyzer. The iron and bromine contents were determined with a Spectra Spectrometer DCP-AEC after dissolving a weight amount of sample in water (aq) confirming the $C_5N_2H_9Br_4Fe$ chemical formula. Elemental analysis for $C_5N_2H_9Br_4Fe$. Calcd: C, 12.71; N, 5.93; H, 1.92; Br, 67.63; Fe, 11.81 %; found: C, 12.65; N, 5.94; H, 1.90; Br, 67.60; Fe, 11.91%.
Thermal analysis: A Mettler-Toledo (TGA/SDTA851 and DSC822) was used for the thermal analyses in an oxygen dynamic atmosphere (50 ml/min) at a heating rate of 10 °C/min. For this experiment, ca. 16 mg of powder sample was thermally treated, and blank runs were performed. Thermal investigations show a solid–solid (s–s) phase transition around 334 K upon cooling from above the melting point (369 K), which starts to decompose at about 684 K (see Figure S1 of Supporting Information).
2.2. Structural characterization: Synchrotron powder X-ray diffraction, High and low resolution neutron diffraction experiments.
Synchrotron powder X-ray diffraction: We have investigated the crystal structure near room temperature (280 K) in detail by high-resolution synchrotron powder X-ray diffraction (SXPD). The experiment was performed at the MS beamline of the Paul Scherrer Institut PSI (Switzerland) at a wavelength $\lambda = 0.6204$ Å. The powder sample, which was thoroughly ground and placed in a thin-walled borosilicate glass capillary with a diameter of ~0.3 mm and 30-mm-long to reduce the effect of the absorption, was spun during the experiment. The diffracted signal was detected using the high-resolution fast MYTHEN II solid-state detector.
Neutron diffraction experiments: Neutron powder diffraction measurements were performed on the HRPT and D1B powder diffractometers at the Laboratory for Neutron Scattering of the Paul Scherrer Institute (LNS PSI, Villigen, Switzerland) and at the Institute Laue-Langevin (ILL, Grenoble, France), respectively. About 3 g of Dimim[$FeBr_4$] were used in the experiments, this being placed in a cylindrical vanadium container and held in a liquid helium cryostat. A high-resolution powder diffractometer, HRPT ($\lambda = 1.8857$ Å) was used to obtain extensive and accurate structural data at room temperature over a large angular angle $4 \leq 2\theta \leq 160º$. High flux and medium resolution of D1B operated at $\lambda = 2.525$ Å were used to study the temperature evolution of the sample in the temperature range 2– 10 K to solve the magnetic contributions of the neutron patterns. Data were collected every 0.5 K with an acquisition time of 40 min in

the angular range $5 \leq 2\theta \leq 90^{\circ}$. The crystal structures of Dimim[$FeBr_4$] were solved by the direct-space methodology implemented in TALP[1] software using intensities extracted with DAJUST[2] program and introducing the structure determined by high-resolution neutron diffraction data of Dimim[$FeCl_4$][3] as a starting model. At 10 K, the final restrained Rietveld refinement was performed with the computer RIBOLS18[4] program by applying the restraints taken from the corresponding Density Functional Theory (DFT) calculations obtained at 0 K.

2.3. Physical characterization techniques.

Variable-temperature magnetic susceptibility measurements were performed using a standard Quantum Design PPMS magnetometer whilst heating from 2 to 300 K in the $1 \leq H/\text{kOe} \leq 85$ range after cooling in either the presence (field cooling, FC) or the absence (zero field cooling, ZFC) of the applied field. Magnetization as a function of field (H) was measured using the same magnetometer in the $-85 \leq H/\text{kOe} \leq 85$ range at 2 and 15 K after cooling the sample in zero field. AC magnetic susceptibility measurements were carried out using the QD PPMS magnetometer with an alternate excitation field (hac) of 3 Oe and frequencies from 100 to 10,000 Hz. Heat capacity was measured with the same magnetometer between 2 and 300 K at several magnetic fields from 0 to 85 kOe using a standard relaxation method with a two-tau model. In order to guarantee a good thermal contact, apiezon N grease was used to glue the sample to the sample-holder. The addenda (sample-holder plus grease) was measured under different magnetic fields before the sample measurements were taken and then subtracted from the total heat capacity in order to get the sample heat capacity. The sample used was a 6.8 mg plate obtained compressing the original thin powder. Mössbauer spectra from RT to 10 K were collected in transmission mode using a conventional constant-acceleration spectrometer and a 25 mCi 57Co source in a Rh matrix. The velocity scale was calibrated using α-Fe foil. Low-temperature spectra were collected using a bath cryostat with the sample immersed in flowing He gas (temperature stability of 0.2 K). The spectra were fitted to Lorentzian lines using a non-linear least-squares method[5]. The non-polarized Raman spectra were taken in the backscattering geometry with a Horiba T64000 triple spectrometer with a confocal microscope in the subtractive mode that had a resolution of 0.6 cm-1, a 1800 grooves/mm grating and a 100-μm slit was equipped with a liquid N2-cooled CCD detector (Jobin-Yvon Symphony). A 647 nm line of a Coherent Innova Spectrum 70C Ar+-Kr+ laser was focused down with a 20x objective and kept the power on the sample below 5 mW to avoid laser-heating effects on the material being tested and the concomitant softening of the observed Raman peaks. For low temperature measurements (4-14 K) we used a liquid helium cooled, vacuum loading continuous flow (CF) cryostat with a special narrow tail for optical microscopy and Raman spectroscopy measurements (MicrostatHe2 from Oxford Instruments) with a temperature precision of 0.1 K at low temperatures.

2.4. DFT calculations. Computational details.

We have carried out density functional first-principles simulations based on a numerical atomic orbital method as implemented in the SIESTA[6] code. All the calculations have been performed within the efficient implementation[7] of the vdw density functional of Dion et al.[8] This fully non-local vdw correlation has been recently tested on imidazolium-based ionic liquids[9], showing spectacular improvements in the interatomic geometries, equilibrium volume and internal geometry with respect to the local density (LDA) and generalized gradient approximation (GGA) at a very modest computational cost.

Core electrons were replaced by ab-initio norm conserving pseudopotentials, generated using the Troullier-Martins scheme[10], in the Kleinman-Bylander fully non-local separable representation[11]. In order to avoid the spiky oscillations close to the nucleus we have

included small partial core corrections[12] for all the atoms. The reference configuration and cutoff radii for each angular momentum shell and the matching radius between the full core charge density and the partial core charge density for the nonlinear core corrections (NLCCs) for the pseudopotentials used in this work can be found in Table S.1 of Supporting Information for H, C, N, Br and Fe.

The one-electron Kohn-Sham eigenstates were expanded on a basis of strictly localized numerical atomic orbitals[13]. We used a double-ζ plus polarization for the valence states of all the atoms. The atomic shells explicitly included in the simulations are the 1s, 2p for H; 2s, 2p, 3d for C and N; 4s, 4p, 4d for Br; and 4s, 4p, 3d for Fe. All the parameters that define the shape and range of the basis functions were obtained by a variational optimization of the enthalpy[14] (with a pressure P=0.1 GPa), using the coordinates of Dimim[$FeBr_4$] obtained by Rietveld refinement from high resolution neutron powder diffraction data as the reference configuration.

The electronic density, Hartree, and exchange correlation potentials, as well as the corresponding matrix elements between the basis orbitals, were calculated in a uniform real space grid. An equivalent plane wave cut-off of 350 Ry was used to represent the charge density. For the Brillouin zone integrations we use a Monkhorst-Pack sampling[15] of 4 × 2 × 4, equivalent to a real-space cut-off of 10 Å.[16]

Starting from the experimental coordinates obtained by high resolution neutron powder diffraction data at 300 K, a full optimization of the crystal lattice parameters and atomic positions was carried out, until a maximum component of the force on any atom was smaller than 0.01 eV/Å and the maximum component of the stress tensor was smaller than 0.0001 eV/$Å^3$.

The intramolecular geometries and distances of the $[Dimim]^+$ cation and $[FeBr4]^-$ anion obtained by DFT calculations lie in the expected range comparable to those found in experimental data (overestimation within the range from 2 to 3 %). The intermolecular distances and orientations are in good agreement with the experimental results, thus confirming that the vdw functional does not introduce any unwanted features in the description of the low temperature structure.[7]

References

1. Vallcorba, O.; Rius, J.; Frontera, C.; Miravitlles, C., *J. Appl. Crystallogr*. **2012**, 45, 1270-1277.
2. Vallcorba, O.; Rius, J.; Frontera, C.; Peral, I.; Miravitlles, C., *J. Appl. Crystallogr.* **2012**, 45, 844-848.
3. García-Saiz, A.; Migowski, P.; Vallcorba, O.; Junquera, J.; Blanco, J. A.; González, J. A.; Fernández-Díaz, M. T.; Rius, J.; Dupont, J.; Rodríguez Fernández, J.; de Pedro, I., Chem. Eur. J 2014, 20, 72-76.
4. Rius, J., *RIBOLS18- A computer program for least-squares refinement from poder diffraction data; Institut de Ciència de Materials de Barcelona (CSIC): Barcelona, Spain.* **2012**.
5. Waerenborgh, J. C.; Salamakha, P.; Sologub, O.; Gonçalves, A. P.; Cardoso, C.; Sério, S.; Godinho, M.; Almeida, M., *Chem. Mater*. **2000**, 12, 1743-1749.
6. Soler, J. M.; Artacho, E.; Gale, J. D.; García, A.; Junquera, J.; Ordejón, P.; Sánchez-Portal, D., *J. Phys.: Condens. Matter* **2002**, 14, 2745-2779.
7. Román-Pérez, G.; Soler, J. M., *Phys. Rev. Lett*. **2009**, 103, 096102.
8. Dion, M.; Rydberg, H.; Schröder, E.; Langreth, D. C.; Lundqvist, B. I., *Phys. Rev. Lett.* **2004**, 92, 246401.

9. Kohanoff, J.; Pinilla, C.; Youngs, T. G.; Artacho, E.; Soler, J. M., *J. Chem. Phys*. **2011**, 135, 154505.
10. Troullier, N.; Martins, J. L., *Phys. Rev. B* **1991**, 43, 1993-2006.
11. Kleinman, L.; Bylander, D. M., *Phys. Rev. Lett*. **1982**, 48, 1425-1428.
12. Louie, S. G.; Froyen, S.; Cohen, M. L., *Phys. Rev. B* **1982**, 26, 1738-1742.
13. (a) Sankey, O. F.; Niklewski, D. J., *Phys. Rev. B* **1989**, 40, 3979-3995; (b) Artacho, E.; Sánchez-Portal, D.; Ordejón, P.; García, A.; Soler, J. M., Phys. *Status Solidi B* **1999**, 215, 809-817.
14. Anglada, E.; M. Soler, J.; Junquera, J.; Artacho, E., *Phys. Rev. B* **2002**, 66, 205101.
15. Monkhorst, H. J.; Pack, J. D., *Phys. Rev. B* **1976**, 13, 5188-5192.
16. Moreno, J.; Soler, J. M., *Phys. Rev. B* **1992**, 45, 13891-13898.

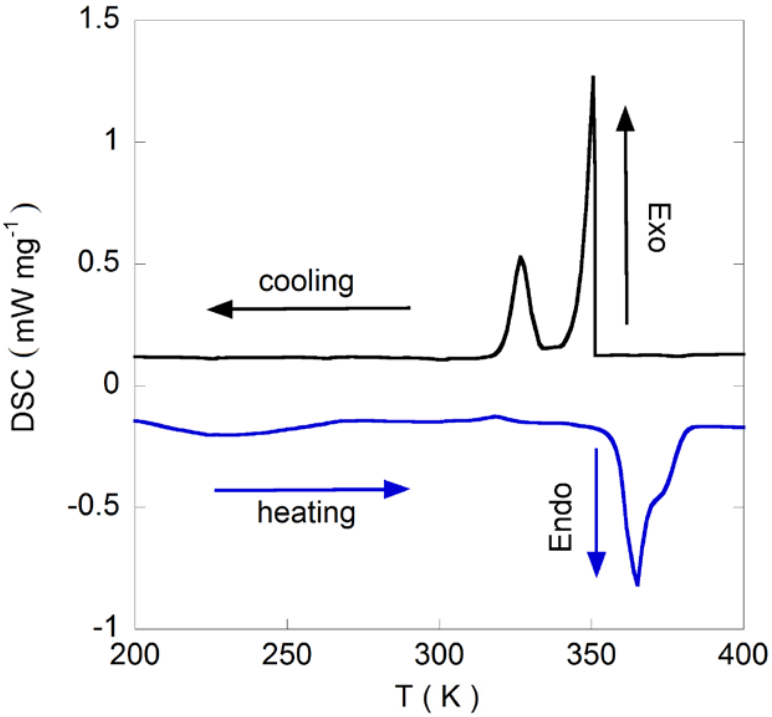

Figure S.1 (a)

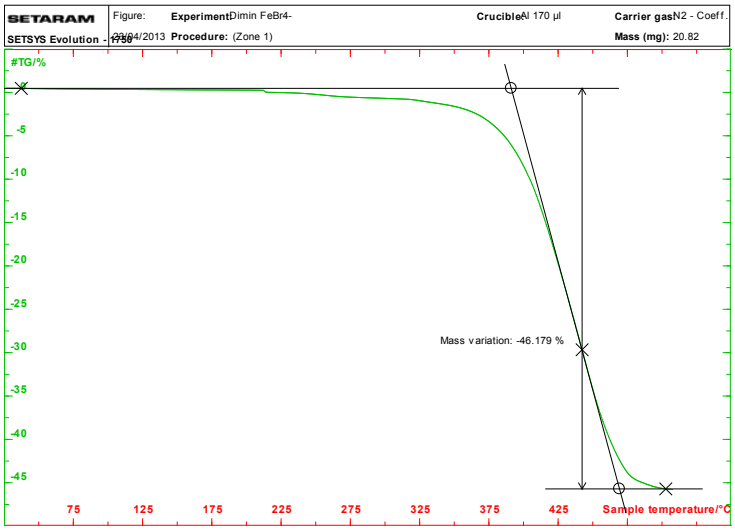

(b)

Figure S.1 (b)

Figure S1. (a) DSC-thermogram of Dimim[$FeBr_4$]. Black line: 1st cooling cycle; blue line: 2nd heating cycle. Heating rate 10 K/min. (b) TGA curve recorded in the inert atmosphere.

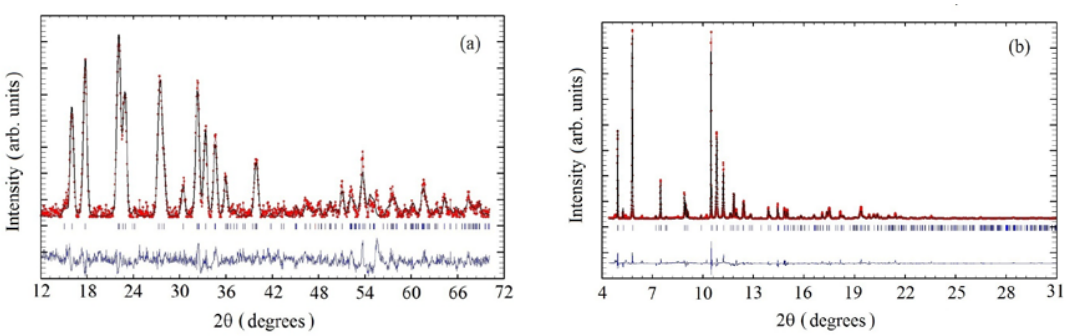

Figure S.2. Observed (red points) and calculated (blue solid line) powder diffraction patterns for Dimim[$FeBr_4$]: (a) neutron diffraction data at 300 K and (b) synchrotron powder X-ray data at 280 K. Positions of the Bragg reflections are represented by vertical bars. The observed-calculated difference patterns are depicted at the bottom of each figure.

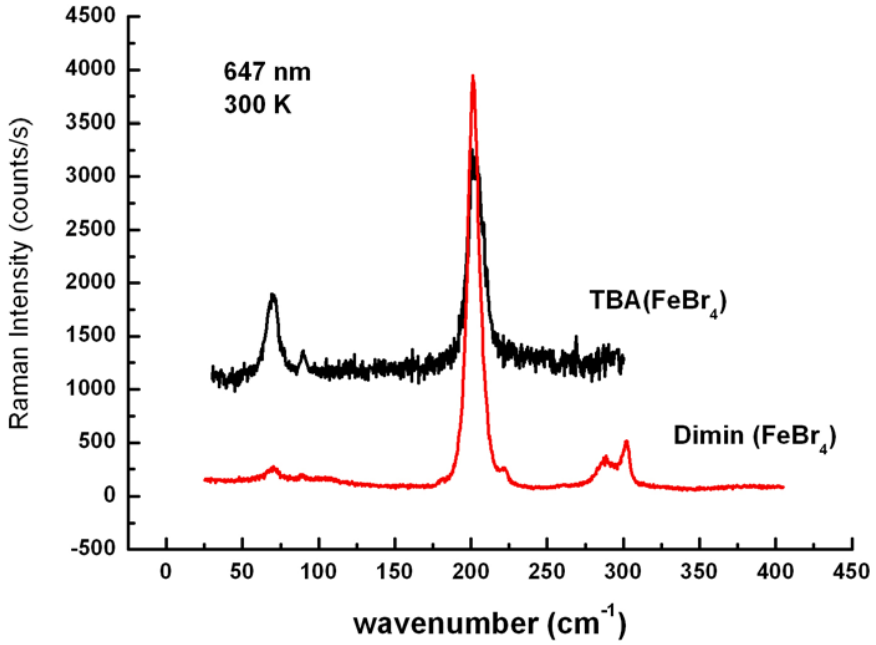

Figure S.3. Comparison of the frequencies of the Raman modes of Dimim[$FeBr_4$] and TBA[$FeBr_4$] with a 647 nm laser at 300 K. We can see how the bending and stretching of the ion [$FeBr_4$] frequencies in both compounds are very similar.

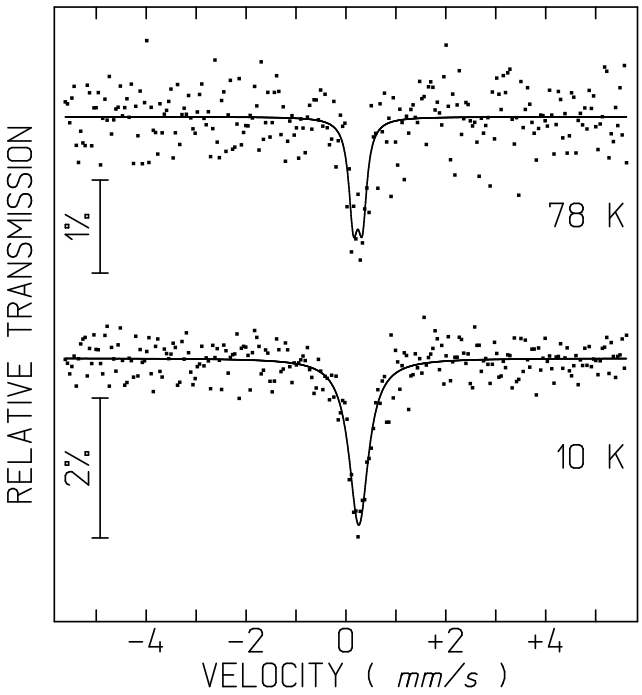

Figure S.4. Mössbauer spectra of Dimim[$FeBr_4$] at 78 and 10 K.

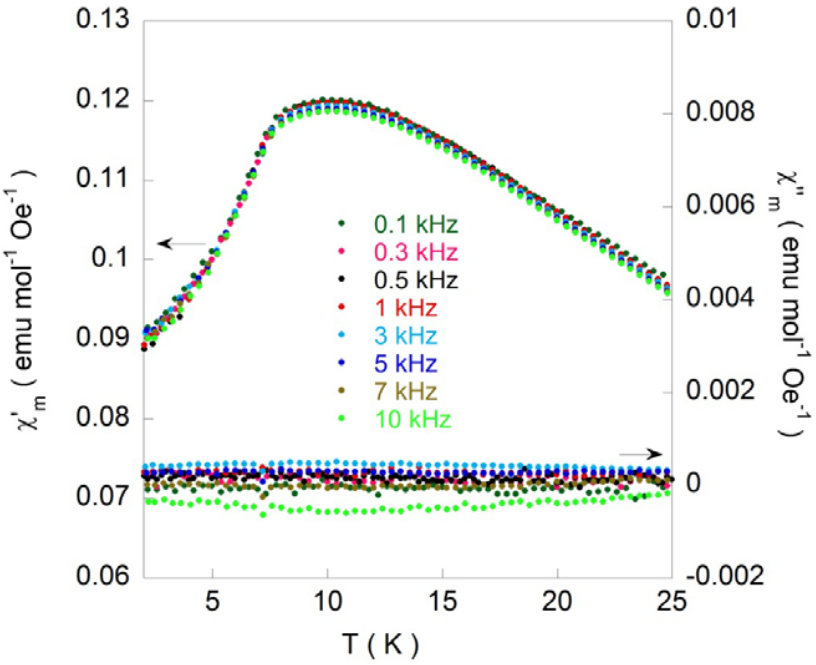

Figure S.5.Temperature dependence of the real (χ') and imaginary (χ'') components of the ac magnetic susceptibility for Dimim[$FeBr_4$] measured under an ac field hac = 10 Oe and frequencies from 100 to 10000 Hz.

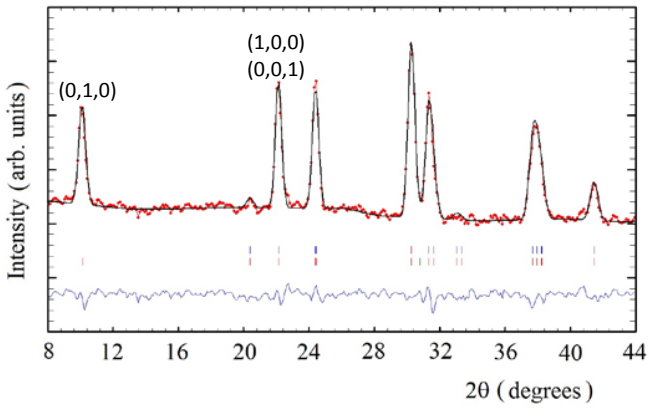

Figure S.6. Neutron diffraction profile of Dimim[$FeBr_4$] at 2 K obtained in D1B. Crosses are experimental, solid line calculated and blue line differential data. The first line of vertical marks corresponds to the position of the allowed reflexions for the crystallographic structure and the second line marks the magnetic reflections.

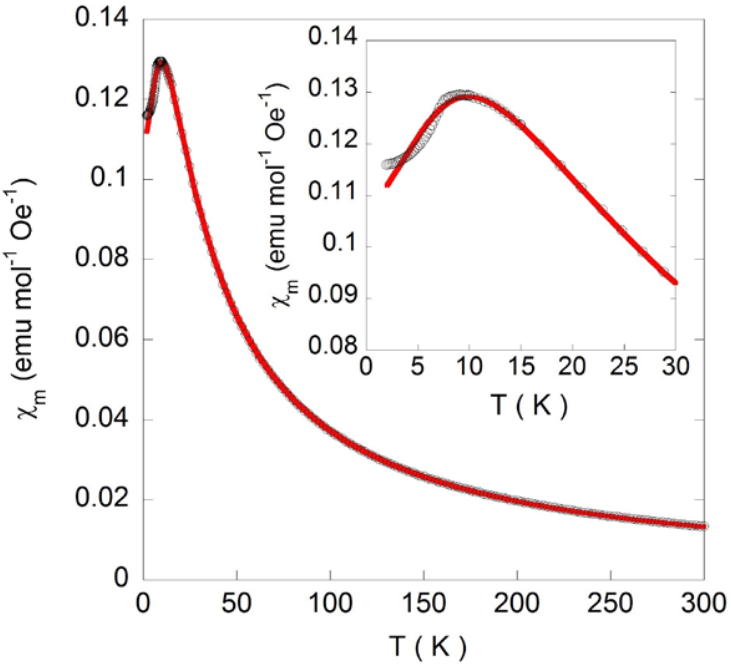

Figure S.7. Temperature dependence of χ_m (black circles) for Dimim[$FeBr_4$] measured under 1 kOe. The solid red line is the fit according to Equation (3) of the text.

Table S.1. Reference configuration and cut-off radii of the pseudopotentials used in our study. NLCC for non-linear corrections. Units in Bohr.

		H	C	N	Br	Fe
Reference		$1s^1, 2p^0, 3d^0, 4f^0$	$2s^2, 2p^2, 3d^0, 4f^0$	$2s^2, 2p^3, 3d^0, 4f^0$	$4s^2, 4p^5, 4d^0, 4f^0$	$4s^2, 4p^0, 3d^6, 4f^0$
Core radius	*s*	1.00	1.30	1.35	1.50	2.10
	p	1.25	1.30	1.35	1.80	2.40
	d	1.25	1.30	1.35	2.50	2.00
	f	1.25	1.30	1.35	1.50	2.00
Scalar relativistic		no	no	no	yes	yes
Core corrections		no	yes	yes	yes	yes
Cut-off radii for core corrections		no	1.40	1.30	1.00	0.70

Table S.2. Crystallographic data and structure refinement details for Dimim[$FeBr_4$] from high resolution neutron powder diffraction (300 K), synchrotron powder X Ray diffraction pattern (280 K) and DFT calculations (0 K).

	Dimim[$FeBr_4$] at 300K	**Dimim[$FeBr_4$] at 280K**	**Dimim[$FeBr_4$] at 0K***
Molecular formula	$C_5H_9N_2$, Br_4Fe	$C_5H_9N_2$, Br_4Fe	$C_5H_9N_2$, Br_4Fe
Formula weight	472.59	474.29	474.29
Crystal System	Monoclinic	Monoclinic	Monoclinic
Space group	$P2_1$	$P2_1$	$P2_1$
a (Å)	6.745(3)	6.7520(1)	6.8459(1)
b (Å)	14.364(3)	14.3717(3)	15.1113(3)
c (Å)	6.759(3)	6.7500(2)	6.8505(2)
α (º)	90.0	90.0	90.0
β (º)	90.80(2)	90.676(1)	89.71(2)
γ (º)	90.0	90.0	90.0
Volume ($Å^3$)	655.2(5)	654.97(3)	708.68(1)
Z	2	2	2
Calculated density (g/cm^3)	2.395	2.396	
Measurement Temperature (K)	300	298	-
Radiation (wavelengths in Å)	1.8857	0.62039	-
Measured 2θ range, stepsize (º)	3.75–164.70, 0.05	2.00–36.00, 0.00376	-
Rietveld refinement details:			
Profile function	Pseudo-Voigt	Pseudo-Voigt	-
2θ range used	12.00–80.00	4.40–32.00	-
Num. of reflections	240	505	-
Data points	1360	7346	-
Parameters	71	53	-
Restraints	63	33	-
R_{wp}	0.011	0.035	-
R_{exp}	0.008	0.017	-
$\chi_{Rietveld}/\chi_{Pattern\text{-}Matching}$	1.228	1.476	-

* Data calculated by DFT

Table S.3. Final refined positional coordinates from high resolution neutron powder diffraction (300 K) and synchrotron powder X Ray diffraction pattern (280 K). Label of the atoms as in Figures 2 and 3.

	Dimim[$FeBr_4$] at 300K[a]			Dimim[$FeBr_4$] at 280K[b]		
Atom	*x/a*	*y/b*	*z/c*	*x/a*	*y/b*	*z/c*
Fe	0.266(4)	0.00008	0.783(3)	0.2414(11)	0.00008	0.7593(4)
Br1	0.095(9)	-0.138(3)	0.911(3)	0.0984(20)	-0.1337(7)	0.8979(4)
Br2	0.190(7)	0.010(5)	0.437(3)	0.1873(11)	-0.0082(14)	0.4243(4)
Br3	0.105(9)	0.134(4)	0.941(3)	0.1196(17)	0.1344(7)	0.9177(4)
Br4	0.614(6)	0.026(4)	0.842(3)	0.5830(11)	0.0069(14)	0.8254(4)
N1	0.612(4)	0.202(2)	0.444(3)	0.5610(40)	0.2161(14)	0.4415(4)
C2	0.569(5)	0.260(3)	0.595(3)	0.5682(33)	0.2632(15)	0.6143(4)
H2	0.676(8)	0.281(4)	0.708(3)	0.6874	0.2749	0.7216
N3	0.385(4)	0.295(2)	0.568(3)	0.3940(37)	0.3092(13)	0.6309(4)
C4	0.305(5)	0.256(3)	0.397(3)	0.2726(34)	0.2884(16)	0.4679(4)
H4	0.165(5)	0.282(3)	0.338(3)	0.1258	0.3159	0.433
C5	0.451(5)	0.202(3)	0.314(3)	0.3781(46)	0.2299(16)	0.3486(4)
H5	0.454(10)	0.153(3)	0.191(3)	0.3461	0.1857	0.2213
C1'	0.795(5)	0.152(3)	0.391(3)	0.7060(56)	0.1507(14)	0.3556(4)
H1A'	0.754(11)	0.080(3)	0.423(3)	0.6532	0.0784	0.3623
H1B'	0.802(11)	0.166(5)	0.231(3)	0.7564	0.1663	0.2049
H1C'	0.928(6)	0.179(6)	0.467(3)	0.8274	0.1606	0.4633
C1"	0.292(6)	0.359(3)	0.712(3)	0.3334(54)	0.3771(13)	0.7852(4)
H1A"	0.392(10)	0.419(3)	0.692(3)	0.3211	0.4427	0.7018
H1B"	0.137(7)	0.379(6)	0.688(3)	0.1897	0.3593	0.85
H1C"	0.307(14)	0.327(5)	0.858(3)	0.4456	0.3846	0.9034

Full occupancies for all atoms.
(a) a = 6.745(3) Å, b = 14.364(3) Å, c = 6.759(3) Å, $\alpha = \gamma = 90^o$, β = 90.80(2)º, s.g. $P2_1$. $B_{overall}$ = 4.0(2) Å^2.
(b) a = 6.7520(1) Å, b = 14.3717(3) Å, c = 6.7500(2) Å, $\alpha = \gamma = 90^o$, β = 90.676(1)º, s.g. $P2_1$. $B_{overall}$ = 8.4(1) Å^2.

Table S.4. Estimated parameters from the Mössbauer spectra of Dimim[$FeBr_4$] and Choline[$FeCl_4$] taken in the paramagnetic state.

	T	IS (mm/s)	QS/ε (mm/s)
Dimim[$FeBr_4$]	78 K	0.35	0.18
	10 K	0.37	0.14
Choline[$FeCl_4$][45]	160 K	0.27	0.19
	4.1 K	0.32	0.23

IS, isomer shift relative to metallic Fe at 295 K. QS, quadrupole splitting. Estimated standard deviations are < 0.02 mm/s for IS and, QS.

Table S.5. Mulliken spin populations of Dimim[$FeBr_4$] obtained by DFT. The atoms in the imidazolium cation have been fixed at 0.

atom	Spin population
Fe	3.863
Br1	0.293
Br2	0.283
Br3	0.268
Br4	0.271

Capítulo 5

Edimim[$FeCl_4$] y Edimim[$FeBr_4$]

5.1. Introducción

Una vez conocido que la fuerza de interacción va a depender del grado de deslocalización magnética y del halógeno en el complejo metálico, el siguiente paso fue estudiar el efecto de un catión mayor de imidazolio en estos sistemas. Para ello se usó el 1-etil-2,3-dimetilimidazolio, Edimim, combinado con complejos de hierro FeX_4^- (X = Cl and Br). Esta molécula de imidazolio, como se ha comentado, tiene un tamaño mayor que en los anteriores sistemas estudiados, Dimim y Emim. Por lo tanto, a priori, al estar incrementando la distancia entre aniones FeX_4^- dentro de la estructura cristalina, la interacción magnética debería ser más débil.

La caracterización térmica realizada en los MILs Edimim[$FeCl_4$] y Edimim[$FeBr_4$] muestran una transición sólido-sólido a 302 y 301 K y un punto de fusión a 317 y 352 K respectivamente, consistente con mayores interaciones interiónicas en el compuesto de bromo. La estructura cristalina del Edimim[$FeCl_4$] y Edimim[$FeBr_4$], obtenida a partir de medidas en polvo de radiación sincrotrón en ALBA y difracción de rayos X en monocristal a una temperatura de 100 K, presenta un grupo espacial $P2_1/n$ y $P2_1$, respectivamente. Ambas estructuras se pueden describir como capas de cationes y aniones intercaladas cambiando de orientación entre capa y capa. De los datos cristalográficos obtenidos, al igual que ocurría en el compuesto anterior, se observa que aparecen tres tipos de internaciones no covalentes (a) puentes de hidrógeno, (b) halógeno-halógeno, y (c) anión-π. Las interacciones halógeno-halógeno, principales responsables del ordenamiento tridimensional magnético, son un poco mayores que la suma de los radios de van der Walls, al igual que lo observado en los anteriores compuestos de la familia.

Las medidas de susceptibilidad magnética en función de la temperatura muestran un comportamiento paramagnético en casi todo el rango de temperaturas estudiado. En el régimen de bajas temperaturas, aparece un máximo en la susceptibilidad a 2.9 K y 9 K para el Edimim[$FeCl_4$] y Edimim[$FeBr_4$] respectivamente, indicando la existencia de ordenamiento magnético de largo alcance. En estos compuestos, al igual que con el Emim[FeX_4] y Dimim[FeX_4] (X = Cl o Br), al sustituir cloro por bromo las interacciones magnéticas son más fuertes. Sin embargo, en contra de la primera hipótesis planteada de que un tamaño más pequeño del catión favorece interacciones más fuertes, en el caso del Edimim[$FeBr_4$], la temperatura de orden es mayor que en el Dimim[$FeBr_4$]. Asimismo, de los ajustes magnéticos, se deduce que las interacciones magnéticas interplanares son las más fuertes. Finalmente las correlaciones magneto-estructurales y los cálculos de DFT demuestran que la temperatura de orden más alta en el compuesto de bromo no puede atribuirse a cuestiones del tamaño del catión, sino que debe atribuirse a una mayor deslocalización de espín del hierro hacia los bromos, lo que favorece el acoplamiento magnético.

5.2. Artículo VI

Artículo publicado en la revista *RSC Advances*: “Anion-π and Halide-Halide Nonbonding Interactions in a New Ionic Liquid Based on Imidazolium Cation with Three-Dimensional Magnetic Ordering in the Solid State”

1-Ethyl-2,3-dimethylimidazolium paramagnetic ionic liquids with 3D magnetic ordering in its solid state: synthesis, structure and magneto-structural correlations

Abel García-Saiz, Imanol de Pedro, Oriol Vallcorba, Pedro Migowski, Ignacio Hernández, Luis Fernández Barquin, Isaac Abrahams, Majid Motevalli, Jairton Dupont, Jesús Antonio Gonzalez and Jesus Rodriguez Fernandez

RSC Adv., 2015, 5, 60835

DOI: 10.1039/c5ra05723j

Table S1. Final refined positional coordinates from synchrotron powder X Ray diffraction pattern of Edimim[$FeCl_4$] at 100 K.

Edimim[$FeCl_4$] at 100K			
Atom	*x/a*	*y/b*	*z/c*
Fe	0.5300(2)	1.7467(2)	1.2536(4)
Cl1	0.4423(3)	1.7756(3)	1.4559(4)
Cl2	0.3625(3)	1.7637(3)	1.0826(4)
Cl3	0.7005(4)	1.8427(3)	1.2174(4)
Cl4	0.6017(4)	1.6007(2)	1.2449(4)
C1''	0.0713(11)	0.8728(7)	1.3526(4)
H1A''	0.0102	0.8231	1.2918
H1B''	0.0047	0.9155	1.4102
H1C''	0.1432	0.837	1.4238
C1'	0.3789(10)	1.1206(7)	1.1917(4)
H1A'	0.3666	1.1675	1.2769
H1B'	0.3614	1.1545	1.0923
C2'	0.5220(11)	1.0850(7)	1.1970(4)
H2A'	0.5431	1.0507	1.2955
H2B'	0.592	1.1423	1.1893
H2C'	0.5352	1.0369	1.1138
C1'''	0.2771(11)	1.0208(8)	1.4519(4)
H1A'''	0.3459	1.0794	1.4568
H1B'''	0.3303	0.9612	1.4962
H1C'''	0.1893	1.0359	1.5097
C2	0.2343(11)	1.0012(8)	1.3040(4)
N3	0.1463(9)	0.9324(7)	1.2623(4)
N1	0.2778(9)	1.0443(7)	1.1936(4)
C5	0.2095(11)	1.0065(8)	1.0721(4)
H5	0.2187	1.0261	0.9695
C4	0.1287(11)	0.9365(7)	1.1165(4)
H4	0.0632	0.8956	1.0525

Full occupancies for all atoms.
a = 9.6703(1) Å, b = 14.3513(2) Å, c = 9.5744(1) Å, $\alpha = \gamma = 90^{o}$, β = 94.261(1)º, s.g. $P2_1/n$, B_{Fe} = 2.5(2) Å^2, B_{Cl} = 2.9(1) Å^2, B_{Edimim} = 3.2(2) Å^2

Table S2. Final refined positional coordinates obtained from X Ray single crystal diffraction of Edimim[$FeBr_4$] at 100 K.

Edimim[$FeBr_4$] at 100K			
Atom	*x/a*	*y/b*	*z/c*
Fe	0.2999(3)	0.73410(14)	0.7427(3)
Br1	0.4534(2)	0.62359(11)	0.5637(3)
Br2	0.4247(2)	0.73187(12)	1.0494(2)
Br3	0.3449(2)	0.87866(10)	0.6117(2)
Br4	-0.0321(2)	0.70335(11)	0.7492(2)
C1''	1.088(3) -	1.1013(15)	0.263(3)
H1A''	0.9990	1.1233	-0.3584
H1B''	1.2036	1.0768	-0.3211
H1C''	1.1248	1.1512	-0.1806
C1'	0.948(2)	0.8567(10)	0.200(2)
H1A'	1.0849	0.8491	0.2369
H1B'	0.8960	0.7971	0.1629
C2'	0.836(3)	0.8954(19)	0.354(3)
H2A'	0.8430	0.8546	0.4606
H2B'	0.7019	0.9028	0.3146
H2C'	0.8899	0.9543	0.3885
C1'''	1.260(4)	1.003(2)	0.086(5)
H1A'''	1.2890	0.9614	0.1889
H1B'''	1.2572	1.0649	0.1320
H1C'''	1.3599	0.9970	-0.0078
C2	1.063(3)	0.9783(19)	0.000(4)
N3	0.991(4)	1.0267(17)	-0.150(4)
N1	0.930(3)	0.9221(14)	0.045(3)
C5	0.789(4)	0.9298(19)	-0.078(5)
H5	0.6857	0.8882	-0.0849
C4	0.804(4)	-1.000(2)	0.190(5)
H4	0.7119	1.0249	-0.2740

Full occupancies for all atoms.
a = 6.957(6) Å, *b* = 14.804(12) Å, *c* = 7.232(6) Å, α = γ = 90º, β = 90.728(14) º, s.g. $P2_1$,

Table S3. Anisotropic displacement parameters ($Å^2x10^3$) for Edimim[$FeBr_4$]. The anisotropic displacement factor exponent takes the form: $-2\pi^2[\, h^2a^{*2}U_{11} + ... + 2\, h\, k\, a^*\, b^*\, U_{12}\,]$. U(eq) is defined as one third of the trace of the orthogonalized U_{ij} tensor.

	U_{11}	U_{22}	U_{33}	U_{23}	U_{13}	U_{12}
Br(1)	26(1)	43(1)	47(1)	0(1)	7(1)	-8(1)
Br(2)	36(1)	42(1)	33(1)	4(1)	0(1)	3(1)
Br(3)	33(1)	30(1)	39(1)	6(1)	5(1)	-6(1)
Br(4)	38(1)	38(1)	48(1)	-11(1)	6(1)	11(1)
Fe(1)	26(1)	24(1)	32(1)	2(1)	4(1)	1(1)
C(1A)	49(10)	82(16)	30(12)	12(10)	5(9)	-7(10)
C(5A)	27(7)	33(9)	25(9)	5(7)	10(6)	-2(6)
C(6A)	43(10)	130(20)	62(17)	52(15)	26(9)	44(12)
C(3A)	32(13)	49(18)	42(19)	-20(16)	-8(13)	26(12)
C(2A)	31(8)	29(9)	28(11)	1(7)	2(8)	15(8)
N(1A)	45(9)	37(8)	28(10)	-1(7)	-12(8)	16(9)
N(2A)	25(8)	20(7)	37(10)	4(7)	-4(8)	5(7)
C(4A)	33(9)	32(10)	23(11)	-1(9)	-11(8)	3(8)
C(7A)	40(9)	35(10)	23(10)	-6(8)	-7(8)	8(8)
C(1B)	49(10)	82(16)	30(12)	12(10)	5(9)	-7(10)
C(5B)	27(7)	33(9)	25(9)	5(7)	10(6)	-2(6)
C(6B)	43(10)	130(20)	62(17)	52(15)	26(9)	44(12)
C(3B)	32(13)	49(18)	42(19)	-20(16)	-8(13)	26(12)
C(2B)	31(8)	29(9)	28(11)	1(7)	2(8)	15(8)
N(1B)	45(9)	37(8)	28(10)	-1(7)	-12(8)	16(9)
N(2B)	25(8)	20(7)	37(10)	4(7)	-4(8)	5(7)
C(4B)	33(9)	32(10)	23(11)	-1(9)	-11(8)	3(8)
C(7B)	40(9)	35(10)	23(10)	-6(8)	-7(8)	8(8)

Capítulo 6

Discusión final

El método de síntesis descrito en la presente memoria ha llevado a la obtención de 4 nuevos líquidos iónicos magnéticos: el Dimim[$FeCl_4$], Dimim[$FeBr_4$], Edimim[$FeCl_4$] y Edimim[$FeBr_4$]. Para ello hemos utilizando aniones de tetracloroferrato y tetrabromoferrato unidos con cationes orgánicos basados en el anillo aromático imidazolio. Mediante una caracterización físico-química se ha comprobado que la formación de estos compuestos era la deseada.

El Emim[$FeCl_4$] presenta un orden magnético tridimensional en torno a 4 K. Las medidas de la susceptibilidad magnética AC (no hay dependencia con la frecuencia) junto con las medidas de la imanación en función del campo magnético aplicado (no presenta histéresis magnética) claramente sugieren que el ordenamiento es de tipo antiferromagnético, descartando un estado spin-glass. Por otro lado, los análisis estructurales de este MIL fueron infructuosos debido a la formación de orientaciones preferenciales en las medidas de difracción de rayos X. Además, las medidas de difracción de neutrones presentan una gran contribución de scattering incoherente debido al gran número de hidrógenos, perjudicando la calidad de los datos. Para intentar resolver este problema y poder determinar las estructuras cristalinas, se realizó una deuteración de la muestra. Respecto a las propiedades magnéticas, las temperaturas de orden y comportamiento magnético eran similares. Sin embargo, los diagramas de difracción de neutrones eran muy diferentes a los del compuesto sin deuterar. Un estudio del Emim[$FeCl_4$] sometido a presión hidrostática sugiere que el ordenamiento magnético se ve influenciado por la presión, induciendo una transición a un ordenamiento ferrimagnético por encima de una presión de 3.4 kbar y aumentando la temperatura de orden un 40 %.

El compuesto 1,3-dimetilimidazolio tetracloroferrato, estudiado para observar la influencia del tamaño del catión en las propiedades magnéticas, dio lugar a un compuesto con ordenamiento antiferromagnético por debajo 5.6 K, indicando a priori que un menor tamaño del catión da lugar a una estructura cristalina más compacta en la que los complejos metálicos se encuentran más cerca, interaccionando más fuertemente. A partir de un estudio de difracción de neutrones se llegó a que el Dimim[$FeCl_4$] cristaliza formando capas de aniones y cationes apiladas en la dirección *b* en una estructura monoclínica $P2_1$ a temperatura ambiente mientras que a 9 K es ortorrómbica con grupo espacial $P2_12_12_1$. Por medio de cálculos DFT con el código SIESTA se encontró que la estructura magnética más estable era la que presenta un ordenamiento antiferromagnético tanto dentro de los planos como entre los planos. Además, analizando la densidad de espín, se observó que se producía una transferencia parcial de momento magnético del hierro a los cloros, fortaleciendo la interacción magnética, que viene mediada por una interacción de supercanje a través de los caminos de intercambio Fe-Cl–Cl-Fe.

Para estudiar el efecto del anión en la interacción magnética se realizó un estudio sobre el 1,3-dimetilimidazolio tetrabromoferrato, cuyo anión presenta un halógeno menos electronegativo. El Dimim[$FeBr_4$] presenta un ordenamiento antiferromagnético por debajo de 9.2 K. Del análisis de difracción de rayos X en sincrotrón y neutrones se obtiene que el compuesto es isostructural al Dimim[$FeCl_4$] con grupo espacial $P2_1$. Sin embargo, la disposición de las moléculas permite la formación de interacciones anión-π, y junto con los cálculos DFT pudo observarse que además, está interacción está involucrada en los caminos de canje magnéticos por medio de interacciones de intercambio Fe-Br–Im–Br-Fe (Im = Imidazolio).

El estudio de las correlaciones magneto-estructurales en los compuestos 1-etil-2,3-dimetilimidazolio tetracloroferrato y tetrabromoferrato revela que en el caso del compuesto con cloro, la temperatura de orden es de 2.9 K mientras que con bromo es de 9 K, siendo ambos ordenamientos del tipo antiferromagnéticos. El catión es mayor que el Dimim, sin embargo, la temperatura de orden en la muestra bromada es superior. Este hecho pone de manifiesto que el parámetro principal que controla la fuerza de la interacción magnética no es la distancia entre los iones magnéticos sino el grado de deslocalización de la densidad de espín del hierro hacia los halógenos.

Capítulo 7

Conclusiones

- Se han sintetizado cuatro nuevos MILs basados en cationes de imidazolio y aniones de tetracloroferrato y tetrabromoferrato que presentan un ordenamiento antiferromagnético de largo alcance a bajas temperaturas.
- Todos los compuestos estudiados presentan transiciones sólido-sólido por debajo de temperatura ambiente. Sus estructuras cristalinas han sido determinadas, estando formados por capas de aniones y cationes apiladas a lo largo de la dirección *b*.
- Se ha podido determinar, por primera vez, la estructura magnética de un MIL a partir de los datos experimentales de difracción de neutrones.
- Se ha observado que las propiedades magnéticas del Emim[$FeCl_4$] están influenciadas por la presión hidrostática, la cual favorece una transición de un comportamiento antiferromagnético a otro ferrimagnético.
- La deuteración del Emim[$FeCl_4$] modifica tanto el ordenamiento cristalino como el magnético, probablemente debido al efecto de los puentes de hidrógeno.
- El mecanismo de transmisión magnética en los MILs estudiados en la presente memoria se da principalmente por medio de caminos de supercanje del tipo Fe-X–X-Fe (X = halógeno).
- La transferencia electrónica desde el metal al halógeno, junto con el solapamiento de los orbitales, son los responsables principales del incremento de la temperatura de orden magnético. Como consecuencia, la sustitución de Cl por Br produce un aumento de la temperatura de Néel.

- La velocidad de enfriamiento de los MILs influye en la dinámica de los estados sólidos teniendo repercusión en sus propiedades magnéticas a bajas temperaturas.

Apéndice A

Artículos

- Abel García-Saiz, Imanol de Pedro, Jesús Ángel Blanco, Jesús Antonio González, Jesús Rodríguez Fernández.
  Pressure effects on emim[$FeCl_4$], a magnetic ionic liquid with three-dimensional magnetic ordering.
  J. Phys. Chem. B. 2013, 117, 3198 – 3206. doi: dx.doi.org/10.1021/jp3114623. I_F: 3.377

- Imanol de Pedro, Abel García-Saiz, Jesús González, Idoia Ruiz de Larramendi, Teófilo Rojo, Carlos A. M. Afonso, Svilen P. Simeonov, Joao Carlos Waerenborgh, Jesús Ángel Blanco, Beatriz Ramajo and Jesús Rodríguez Fernández.
  Magnetic ionic plastic crystal: choline [$FeCl_4$].
  Phys. Chem. Chem. Phys. 2013, 15, 12724 – 12733. doi: dx.doi.org/10.1039/C3CP50749A. I_F: 4.198

- Abel García-Saiz, Pedro Migowski, Oriol Vallcorba, Javier Junquera, Jesús Ángel Blanco, Jesús Antonio González, María Teresa Fernández-Díaz, Jordi Rius, Jairton Dupont, Jesús Rodríguez Fernández, Imanol de Pedro.
  A Magnetic Ionic Liquid Based on Tetrachloroferrate Exhibits Three-Dimensional Magnetic Ordering: A Combined Experimental and Theoretical Study of the Magnetic Interaction Mechanism.
  Chem. Eur. J. 2014, 20, 72 – 76. doi: dx.doi.org/10.1002/chem.201303602. I_F: 5.731

- Abel García-Saiz, Imanol De Pedro, Pedro Migowski, Oriol Vallcorba, Javier Junquera, Jesús Ángel Blanco, Oscar Fabelo, Denis Sheptyakov, Joao Carlos Waerenborgh, María Teresa Fernández-Díaz, Jordi Rius, Jairton Dupont, Jesús Antonio González, Jesús Rodríguez Fernández.
  Anion-π and Halide-Halide Nonbonding Interactions in a New Ionic Liquid Based on Imidazolium Cation with Three-Dimensional Magnetic Ordering in the Solid State.
  Inorg. Chem. 2014, 53, 8384 – 8396. doi: dx.doi.org/10.1021/ic500882z. I_F: 4.762

- Abel García-Saiz, Imanol de Pedro, Oriol Vallcorba, Pedro Migowski, Ignacio Hernández, Luis Fernández Barquin, Isaac Abrahams, Majid Motevalli, Jairton Dupont, Jesús Antonio González, Jesús Rodríguez Fernández.
  1-Ethyl-2,3-dimethylimidazolium paramagnetic ionic liquids with 3D magnetic ordering in its solid state: synthesis, structure and magneto-structural correlations.
  RSC Adv. 2015, 5, 60835 – 60848. doi: dx.doi.org/10.1039/c5ra05723j. I_F: 3.840

- Imanol de Pedro, Abel García-Saiz, Jairton Dupont, Pedro Migowski, Oriol Vallcorba, Javier Junquera, Jordi Rius, and Jesús Rodríguez Fernández.
  On the Colossal and Highly Anisotropic Thermal Expansion Exhibited by Imidazolium Salts.
  Cryst. Growth Des. 2015, 15 (11), pp 5207 – 5212. doi: dx.doi.org/10.1021/acs.cgd.5b00633. I_F: 4.891

- Abel García-Saiz, Imanol de Pedro, Luis Fernández Barquín, Maria Teresa Fernández-Díaz, Jesús Ángel Blanco, Jesús Rodríguez Fernández.
  Neutron Powder Diffraction study of the Magnetic Ionic Liquid Emim[FeCl4] and its deuterated phase.
  Journal of Physics: Conference Series 663 (2015) 012008. doi: dx.doi.org/10.1088/1742-6596/663/1/012008. I_F: -

- Imanol de Pedro, Abel García-Saiz, Daniel Andreica, Luis Fernández Barquín, María Teresa Fernández-Díaz, Jesús Ángel Blanco, Alex Amato and Jesús Rodríguez Fernández.

Low Temperature Magnetic Ordering of the Magnetic Ionic Plastic Crystal, Choline[FeCl4].
Journal of Physics: Conference Series 663 (2015) 012012. doi: dx.doi.org/10.1088/1742-6596/663/1/012012. I_F: -

- Abel García-Saiz, Imanol de Pedro, Oriol Vallcorba, Oscar Fabelo, Javier Junquera, Jesús Ángel Blanco, Joao Carlos Waerenborgh, D. Andreica, Andrew Wildes, María Teresa Fernández-Díaz, and Jesús Rodríguez Fernández.
  Slow Dynamically Solid-to-Solid Phase Transition Induced by Thermal Treatment on DimimFeCl4 Magnetic Ionic Liquid.
  En preparación

Apéndice B

Comunicaciones a congresos

- **Congreso:** 4th Congress on Ionic Liquids, Washington DC, EEUU. Junio de 2011.
  Título: Neutron diffraction studies on Emim[$FeCl_4$]. A magnetic ionic liquid with long-range magnetic ordering.
  Tipo de participación: Póster

- **Congreso:** ISMANAM 2011, Gijón. Junio de 2011.
  Título: Magnetic Ionic Liquid 1-Ethyl-3-Methylimidazolium Tetrachloroferrate(III). Crystallization Monitored by Powder X-Ray Thermodiffraction.
  Tipo de participación: Oral

- **Congreso:** XXII Congress and General Assembly of the International Union of Crystallography. Madrid. Agosto de 2011.
  Título: Magnetic ionic liquids 1-ethyl- and 1-butyl-3-methylimidazolium tetrachloroferrate(III). Crystallization monitored by powder x-ray thermodiffraction.
  Tipo de participación: Póster

- **Congreso:** XXXIII Bienal de la Real Sociedad Española de Física, Santander. Septiembre de 2011.
  Título: Magnetic Properties of Magnetic Ionic Liquid 1-Ethyl-3-Methylimidazolium Thetrachloroferrate(III).
  Tipo de participación: Oral

- **Congreso:** Sociedad Española de Técnicas Neutrónicas, Segovia, España, Junio 2012.
  Título: Magnetic and Neutron Diffraction Studies on Emin[FeCl4]. A Magnetic Ionic Liquid with Long-Range Magnetic Ordering.
  Tipo de participación: Oral

- **Congreso:** 19th International Conference on Magnetism, Busan, Korea, Julio de 2012.
  Título: Pressure effects on the magnetic properties of Emim[$FeCl_4$], a magnetic ionic liquid with antiferromagnetic ordering.
  Tipo de participación: Oral

- **Congreso:** 13th International Conference on Magnitude Fluids (ICMF-13), New Delhi, India, Enero de 2013.
  Título: Magnetic and Neutron Powder Diffraction Study in a MIL with a Long-range Magnetic Ordering, [Emim][$FeCl_4$].
  Tipo de participación: Oral

- **Congreso:** 5th Congress on Ionic Liquids, Algarve, Portugal, Abril de 2013
  Título: Magnetic Computational and Neutron powder diffraction study in a MIL with a long-range magnetic ordering, [Dimim][$FeCl_4$].
  Tipo de participación: Póster

- **Congreso:** International Conference on Neutron Scattering, ICNS 2013, Edimburgo, 8-12 Julio de 2013.
  Título: In search of the origin of the long-range magnetic ordering of Magnetic Ionic Liquids based on imidazolium cation and tetrachloroferrate anion.
  Tipo de participación: Póster (Premio por el mejor póster de un estudiante)

- **Congreso:** VIII Reunión Grupo Especializado de Física del Estado Sólido, GEFES 2014, Ciudad Real, 22-24 Enero de 2014.
  Título: Magnetic properties of ionic liquids exhibiting three-dimensional magnetic order in their condensed phases.
  Tipo de participación: Oral

- **Congreso:** Molten Salts and Ionic Liquids XXV, EUCHEM 2014, Tallin, 6-11 Julio 2014.
  Título: Anion-π interactions and halogen-halogen nonbonding contacts in magnetic ionic liquids based on imidazolium cation: a combined experimental and computational study.
  Tipo de participación: Oral

- **Congreso:** VII Reunión de la sociedad Española de técnicas neutrónicas, SETN 2014, Pamplona, 22-25 Junio 2014.
  Título: Influence of the Cooling Speed in the Magnetic Properties of Ionic Liquids based on Imidazolium Cation: Dimim[FeCl4].
  Tipo de participación: Oral

- **Congreso:** VII Reunión de la sociedad Española de técnicas neutrónicas, SETN 2014, Pamplona, 22-25 Junio 2014.
  Título: Low Temperature Magnetic Ordering of the Magnetic Ionic Plastic Crystals, Choline[$FeCl_4$].
  Tipo de participación: Póster

- **Congreso:** International conference of magnetism, ICM 2015, Barcelona, 22 de Julio de 2015.
  Título: Magneto-Structural Correlations of Paramagnetic Ionic Liquids with 3D Ordering in the Solid State.
  Tipo de participación: Póster

- **Congreso:** European Conference of neutron scattering, ECNS 2015, Zaragoza, 1 de Septiembre de 2015.
  Título: Unusual Effect of the Cooling Speed on the Structural and Magnetic Behavior of the Magnetic Ionic Liquid Dimim[$FeCl_4$].
  Tipo de participación: Oral

Apéndice C

Experimentos en grandes instalaciones

- **Título:** Phase transition and magnetic structure study in a magnetic ionic liquid with a long-range magnetic ordering, [C2mim][$FeCl_4$].
  Instrumento: G4-2 (LLB).
  Fecha: 23, 24 de Mayo 2012

- **Título:** Neutron powder diffraction study in the first example of MIL with a long-range magnetic ordering [Emim][$FeCl_4$].
  Instrumento: D2B (ILL).
  Fecha: 12, 13 de Junio 2012.

- **Título:** Neutron diffraction study of a magnetic Ionic Liquid Crystal: [Choline][$FeCl_4$].
  Instrumento: D1B (2 días) + D2B (1 día) (ILL).
  Fecha: 10, 11 de Junio 2012 y 14 de Junio 2012.

- **Título:** Investigation of the long range magnetic ordering in a magnetic Ionic Liquid Crystal: [Choline][$FeCl_4$].
  Instrumento: GPS (PSI).
  Fecha: 28, 29 de Junio 2012.

- **Título:** Magnetic structure study in a magnetic ionic liquid with a long-range magnetic ordering, [C2nim][$FeCl_4$],and deutered samples.
  Instrumento: D1B (ILL).

Fecha: 17 de Septiembre 2012.

- **Título:** In search of the origin of the long-range magnetic ordering of Magnetic Ionic Liquids based on imidazolium cation and tetrachloroferrate anion.
  Instrumento: HRPT (2 días) + MS (1 día) (PSI).
  Fecha: 5, 6 de Julio 2013 y 6 de Junio 2013.

- **Título:** Investigation of the Long Range Magnetic Ordering in the magnetic Ionic Liquid EMIM[$FeCl_4$].
  Instrumento: GPS (PSI).
  Fecha: 20, 21 de Noviembre 2013.

- **Título:** Crystal structure determination of the multifunctional [(CnH2n+1)4N][$FeCl_4$] (n=1-2) compounds: Following the phase transition sequence.
  Instrumento: MSPD (ALBA).
  Fecha: 16,17 de Julio de 2014.

- **Título:** In the Search of the Magnetic Interaction Mechanism in MILs Based on Tetrachloroferrate Exhibiting Three-Dimensional Magnetic Ordering.
  Instrumento: MSPD (ALBA).
  Fecha: 18, 19 de Julio de 2014.

- **Título:** Study of the influence of the organic group in the magnetic interaction mechanisms of MILs based on imidazolium tetrahalureferrates family.
  Instrumento: D1B (2 días) + D2B (2 días).
  Fecha: 22-25 de noviembre 2014.

Bibliografía

[1] Jason P. Hallett and Tom Welton. Room-temperature ionic liquids: Solvents for synthesis and catalysis. 2. *Chemical Reviews*, 111(5):3508–3576, 2011.

[2] Markus Dobbelin, Vasko Jovanovski, Irantzu Llarena, Luis J. Claros Marfil, German Cabanero, Javier Rodriguez, and David Mecerreyes. Synthesis of paramagnetic polymers using ionic liquid chemistry. *Polym. Chem.*, 2:1275–1278, 2011.

[3] Paul Brown, Alexey Bushmelev, Craig P. Butts, Jing Cheng, Julian Eastoe, Isabelle Grillo, Richard K. Heenan, and Annette M. Schmidt. Magnetic control over liquid surface properties with responsive surfactants. *Angewandte Chemie International Edition*, 51(10):2414–2416, 2012.

[4] Cheng-Xia Miao, Jin-Quan Wang, Bing Yu, Wei-Guo Cheng, Jian Sun, Sebastien Chanfreau, Liang-Nian He, and Suo-Jiang Zhang. Synthesis of bimagnetic ionic liquid and application for selective aerobic oxidation of aromatic alcohols under mild conditions. *Chem. Commun.*, 47:2697–2699, 2011.

[5] Esther Santos, Jonathan Albo, Andreia Rosatella, Carlos A.M. Afonso, and Angel Irabien. Synthesis and characterization of magnetic ionic liquids (mils) for co2 separation. *Journal of Chemical Technology & Biotechnology*, 89(6):866–871, 2014.

[6] Ahmad Hafiidz Mohammad Fauzi, Nor Aishah Saidina Amin, and Ramli Mat. Esterification of oleic acid to biodiesel using magnetic ionic liquid: Multi-objective optimization and kinetic study. *Applied Energy*, 114:809 – 818, 2014.

[7] Satoshi Hayashi and Hiro o Hamaguchi. Discovery of a magnetic ionic liquid [bmim]fecl4. *Chemistry Letters*, 33(12):1590–1591, 2004.

[8] Jason P. Hallett and Tom Welton. Room-temperature ionic liquids: Solvents for synthesis and catalysis. 2. *Chemical Reviews*, 111(5):3508–3576, 2011.

[9] A. K. Abdul-Sada, K. R. Seddon, and N. J. Stewart. Ionic liquids, 1995.

[10] Peter Larkin. *Infrared and Raman spectroscopy; principles and spectral interpretation*. Elsevier, 2011.

[11] Juan R. Carvajal. FULLPROF: A Program for Rietveld Refinement and Pattern Matching Analysis. *Abstracts of the Satellite Meeting on Powder Diffraction of the XV Congress of the IUCr*, 1990.

[12] Oriol Vallcorba, Jordi Rius, Carlos Frontera, Inma Peral, and Carles Miravitlles. DAJUST: a suite of computer programs for pattern matching, space-group determination and intensity extraction from powder diffraction data. *Journal of Applied Crystallography*, 45(4):844–848, 2012.

[13] Jordi Rius. RIBOLS18- A computer program for least-squares refinement from poder diffraction data. 2012.

[14] Oriol Vallcorba, Jordi Rius, Carlos Frontera, and Carles Miravitlles. TALP: a multisolution direct-space strategy for solving molecular crystals from powder diffraction data based on restrained least squares. *Journal of Applied Crystallography*, 45(6):1270–1277, 2012.

[15] Jordi Rius. Patterson-function direct methods for structure determination of organic compounds from powder diffraction data. XVI. *Acta Crystallographica Section A*, 67(1):63–67, 2011.

[16] Jordi Rius. Derivation of a new tangent formula from Patterson-function arguments. *Acta Crystallographica Section A*, 49(3):406–409, 1993.

[17] Hermann Weingärtner. Zum verständnis ionischer flüssigkeiten auf molekularer ebene: Fakten, probleme und kontroversen. *Angewandte Chemie*, 120(4):664–682, 2008.

[18] Jairton Dupont. On the solid, liquid and solution structural organization of imidazolium ionic liquids. *Journal of the Brazilian Chemical Society*, 15:341 – 350, 2004.

[19] Roberta Bertani, Paolo Sgarbossa, Alfonso Venzo, Francesco Lelj, Mario Amati, Giuseppe Resnati, Tullio Pilati, Pierangelo Metrangolo, and Giancarlo Terraneo. Halogen bonding in metal–organic–supramolecular networks. *Coordination Chemistry Reviews*, 254(5-6):677 – 695, 2010.

[20] Antonio Frontera, Patrick Gamez, Mark Mascal, Tiddo J. Mooibroek, and Jan Reedijk. Putting anion-π interactions into perspective. *Angewandte Chemie International Edition*, 50(41):9564–9583, 2011.

[21] Carolina Estarellas, David Quiñonero, Pere M. Deyà, and Antonio Frontera. *ChemPhysChem*, 14(1):145–154, 2013.

[22] Kristina Noack, Peter S. Schulz, Natalia Paape, Johannes Kiefer, Peter Wasserscheid, and Alfred Leipertz. The role of the c2 position in interionic interactions of imidazolium based ionic liquids: a vibrational and nmr spectroscopic study. *Phys. Chem. Chem. Phys.*, 12:14153–14161, 2010.

[23] José M Soler, Emilio Artacho, Julian D Gale, Alberto García, Javier Junquera, Pablo Ordejón, and Daniel Sánchez-Portal. The siesta method for ab initio order-n materials simulation. *Journal of Physics: Condensed Matter*, 14(11):2745, 2002.

[24] Jorge Kohanoff, Carlos Pinilla, Tristan G. A. Youngs, Emilio Artacho, and José M. Soler. Dispersion interactions in room-temperature ionic liquids: Results from a non-empirical density functional. *The Journal of Chemical Physics*, 135(15): 154505, 2011.

[25] M. Dion, H. Rydberg, E. Schröder, D. C. Langreth, and B. I. Lundqvist. Van der waals density functional for general geometries. *Phys. Rev. Lett.*, 92:246401, 2004.

[26] Javier Campo, Javier Luzón, Fernando Palacio, Garry J. McIntyre, Angel Millán, and Andrew R. Wildes. Understanding magnetic interactions in the series $A_2\mathrm{Fe}X_5 \cdot \mathrm{h_2O}$ ($a =$ K, rb; $x =$ Cl, br). inelastic neutron scattering and dft studies. *Phys. Rev. B*, 78:054415, 2008.

[27] Abel García-Saiz, Imanol de Pedro, Pedro Migowski, Oriol Vallcorba, Javier Junquera, Jesús A. Blanco, Oscar Fabelo, Denis Sheptyakov, Joao Carlos Waerenborgh, María Teresa Fernández-Díaz, Jordi Rius, Jairton Dupont, Jesús Antonio Gonzalez, and Jesús Rodríguez Fernández. Anion-π and halide–halide nonbonding interactions in a new ionic liquid based on imidazolium cation with three-dimensional magnetic ordering in the solid state. *Inorganic Chemistry*, 53(16): 8384–8396, 2014.

[28] Olivier Khan. *Inorganic chemistry*, 23(23):3808–3818, 1984.

[29] Yukihiro Yoshida and Gunzi Saito. Influence of structural variations in 1-alkyl-3-methylimidazolium cation and tetrahalogenoferrate(iii) anion on the physical properties of the paramagnetic ionic liquids. *J. Mater. Chem.*, 16:1254–1262, 2006.

[30] Imanol de Pedro, Daniel P. Rojas, Jonathan Albo, Patricia Luis, Ángel Irabien, Jesús A. Blanco, and Jesús Rodríguez Fernández. Long-range magnetic ordering in magnetic ionic liquid: Emim [fecl4]. *Journal of Physics: Condensed Matter*, 22(29):296006, 2010.

[31] Imanol de Pedro, Daniel P. Rojas, Jesús A. Blanco, and Jesús Rodríguez Fernández. Antiferromagnetic ordering in magnetic ionic liquid emim [fecl 4]. *Journal of Magnetism and Magnetic Materials*, 323(10):1254–1257, 2011.

[32] Tobias Bäcker, Oliver Breunig, Martin Valldor, Klaus Merz, Vera Vasylyeva, and Anja-Verena Mudring. In-situ crystal growth and properties of the magnetic ionic liquid [c2mim][fecl4]. *Crystal Growth & Design*, 11(6):2564–2571, 2011.

[33] Robert Hayes, Gregory G. Warr, and Rob Atkin. Structure and nanostructure in ionic liquids. *Chemical Reviews*, 115(13):6357–6426, 2015.

[34] Firas F. Awwadi, Roger D. Willett, Kirk A. Peterson, and Brendan Twamley. The nature of halogen $\cdots$ halogen synthons: Crystallographic and theoretical studies. *Chemistry – A European Journal*, 12(35):8952–8960, 2006.